Design and Fabrication of Hydrogel Ionotronics

Ran Huo

Department of Mechanical Engineering
McGill University
Montreal, Canada

April 2024

A dissertation submitted to McGill University in partial fulfillment of the requirements for the degree of Doctor of Philosophy

Abstract

Electronics devices have integrated into various aspects of contemporary life, spanning entertainment, office productivity, industrial applications, and healthcare. The rise of commercially accessible wearable technology has catalyzed the advancements of soft electronics that better match the human body compared to conventional rigid electronics. Over the past decade, various strategies to render electronics soft and stretchable have been developed, among which, ionotronics have gained increasing attention. Ionotronics are devices that conduct current via ions and electrons. Their physical, mechanical, and electrical resemblances to tissues enable better electrical communication at the interface of human and machine and holds great potential for use as wearable and implantable devices.

Despite the promises, it remains a major challenge to fabricate structurally precise, mechanically robust, and electrically high-performance hydrogel ionotronics that are comparable to current state-of-the-art electronic products. The inability to fabricate and integrate multiple ionic components further hinders the invention of new ionic functions and limits the variety of ionotronics. Although 3D printing stands as a promising solution, current developments in 3D-printable hydrogel ionotronic materials encounter difficulties in achieving a balance between ink printability, structural mechanical robustness, and ionotronic performance. To this end, this thesis focuses on the design of 3D-printable and tough hydrogel ionotronic materials and the fabrication of various multi-component hydrogel ionotronic devices.

The thesis first presents a conductive printable tough adhesive polyacrylic acid/chitosan hydrogel. The material system features a triggered mechanical enhancement mechanism to transform a 3D-printable hydrogel ink into a stretchable and tough structure. By leveraging oppositely charged long-chain polymers as the hydrogel backbones, the material is intrinsically printable. Upon exposure to water or body fluid, strong electrostatic interactions drive polymer network contraction and strengthening, resulting in marked mechanical enhancement in toughness, stiffness, tensile strength, and stretchability. The highly charged polyelectrolytes render the ionic conductivity and further support application as strain sensors.

Despite simultaneously achieving high printability and toughness, the proposed PAAc/Chit ionotronic material still faces limitations, including compromised electrical conductivity, monotonous electrical functionality, and significant size changes after phase transition. These drawbacks impede the broader application of this material in ionotronic devices. To address these challenges, a more versatile 3D printing method compatible with fabrication of multi-component ionotronics for expanded ionic device functionalities is proposed. The 3D ionic microgel printing strategy features double-network microgels containing different ionic species embedded in a secondary polymer network. The use of ionic microgels enables a combination of intrinsic printability, tough mechanics, and high electrical performance. This method allows one to fabricate ionic devices of various configurations with high geometrical definition and strong adhesion between dissimilar units. With the printing method and material system, an array of high-performance ionotronics, including ionic diodes, ionic bipolar transistors, ionic rectifiers, and ionic touchpads were demonstrated.

Résumé

Les appareils électroniques ont été intégrés dans divers aspects de la vie contemporaine. L'essor de la technologie portable commercialement accessible a catalysé les progrès de l'électronique souple qui s'adapte mieux au corps humain que l'électronique rigide conventionnelle. Diverses stratégies ont été mises au point pour rendre l'électronique souple et extensible, parmi lesquelles l'ionotronique a fait l'objet d'une attention croissante. Les ionotroniques sont des dispositifs qui conduisent le courant par l'intermédiaire d'ions et d'électrons. Leur ressemblance physique, mécanique et électrique avec les tissus permet d'améliorer la communication électrique à l'interface entre l'homme et la machine et offre un grand potentiel d'utilisation en tant que dispositifs portables et implantables.

Malgré ces promesses, la fabrication d'ionotroniques à base d'hydrogel structurellement précises, mécaniquement robustes et électriquement performantes, comparables aux produits électroniques, reste un défi majeur. L'impossibilité de fabriquer et d'intégrer de multiples composants ioniques entrave en outre l'invention de nouvelles fonctions ioniques et limite la variété des ionotroniques. Bien que l'impression 3D soit une solution prometteuse, les développements actuels des matériaux ionotroniques hydrogel imprimables en 3D rencontrent des difficultés pour atteindre un équilibre entre l'imprimabilité de l'encre, la robustesse mécanique de la structure et la performance ionotronique. À cette fin, cette thèse se concentre sur la conception de matériaux ionotroniques hydrogel imprimables en 3D et résistants et sur la fabrication de divers dispositifs ionotroniques hydrogel multicomposants.

Cette thèse présente tout d'abord un hydrogel conducteur imprimable et résistant à base d'acide polyacrylique et de chitosane. Le système de matériau comporte un mécanisme d'amélioration mécanique déclenché pour transformer une encre hydrogel imprimable en 3D en une structure extensible et résistante. En s'appuyant sur des polymères à longue chaîne chargés de manière opposée comme squelette de l'hydrogel, le matériau est intrinsèquement imprimable. Lors de l'exposition à l'eau ou à un fluide corporel, de fortes interactions électrostatiques entraînent la contraction et le renforcement du réseau de polymères, ce qui se traduit par une amélioration mécanique marquée de la ténacité, de la rigidité, de la résistance à la traction et de l'extensibilité. Les polyélectrolytes hautement chargés assurent la conductivité ionique et renforcent l'application en tant que capteurs de déformation.

Bien que le matériau ionotronique PAAc/Chit proposé présente simultanément une imprimabilité et une ténacité élevées, il reste confronté à des limitations, notamment une conductivité électrique compromise, une fonctionnalité électrique monotone et des changements de taille après la transition de phase. Ces inconvénients empêchent une application plus large de ce matériau dans les dispositifs ionotroniques. Pour relever ces défis, une méthode d'impression 3D plus polyvalente, compatible avec la fabrication de dispositifs ionotroniques à composants multiples, est proposée pour élargir les fonctionnalités des dispositifs ioniques. La stratégie d'impression 3D de microgels ioniques comprend des microgels à double réseau contenant différentes espèces ioniques intégrées dans un réseau polymère secondaire. L'utilisation de microgels ioniques permet de combiner l'imprimabilité intrinsèque, une mécanique robuste et des performances électriques élevées. Cette méthode permet de fabriquer des dispositifs ioniques de différentes configurations avec une haute définition géométrique et une forte adhésion entre des unités dissemblables. Grâce à la méthode d'impression et au système de matériaux, une série de dispositifs ioniques de haute performance, y compris des diodes ioniques, des transistors bipolaires ioniques, des redresseurs ioniques et des pavés tactiles ioniques, ont été démontrés.

Acknowledgements

Foremost, I would like to express my deep and sincere gratitude to my Ph.D. advisor, Prof. Jianyu Li, for introducing me to the world of research and generously supported me during my doctoral study. Prof. Jianyu Li provided me with the opportunities, freedom, and maximum supports to explore the biomaterials realm, and his enthusiasm in the field never stopped to inspire me. The creative ideas that he could never wait to share with me, the insights that he had on my research problems, and the stories of him when he was a student always guided me. Prof. Jianyu Li also offered me with opportunities to collaborate with people from diverse backgrounds, broadening my horizon and exposing me to the bigger scientific world. I truly enjoy working with him, and I deeply treasure such an invaluable experience.

I also wish to thank the friendly lab environment and all the lovely people in our lab. To my friends in office MD352, Zhenwei, Xuan, Chris, Alex, Portia, Zhen, Shiyu, Yin, Michelle, David-Michael, and Xiang, thank you all for creating this pleasant and relaxing lab retreat, where we had so much fun and laughter. To my good friend, mentor, and desk mate, Zhenwei, thank you for the wise advice that guided me through my research. You have always been a role model for me that I look up to. To my good friend and mentor, Guangyu, thank you for always being so patient and willing to help. Your efficiency and achievements in both research life always motivate me. To my coffee bestie, Xuan, thanks for the coffee chats that always cleared my mind and the tasty coffee you shared with me to energize my day. To my dear friends, Chris, Alex, and Portia, thanks for always being so caring and delightful. You showed me the real Canadians, and your presence always cheers me up even during my worst days. It was a wonderful trip we had to PEI that I will never forget. To the OG gang of the lab, Zhen and Shuaibing, thank you for all the mechanics and chemistry lessons you taught me and the late nights that we spent in the lab. To Aram, thanks for the wise tips and tricks in life and always being so cheerful and sophisticated. To Tianqin and Yixun, thanks for your help in the putty projects. You amazed me with the excellence you demonstrated as a younger generation. To Justin, thank you for the authentic Italian coffee. To Farshid, thank you for the career advice and being so knowledgeable. To David-Micheal, thanks for mentoring me on the bioreactor project and bringing so much happiness to the lab. I miss the Friday afternoon hangouts a lot. To my other friends in the Li lab, Evan, Mary, Louis, Malvika, and Binbin, I extend my sincere gratitude for the assistance and support you have provided over the years. Engaging in discussions with you about research ideas and future career goals has been truly enjoyable.

I also wish to express my sincere gratitude to my collaborators from diverse backgrounds. The work of this thesis would not have been possible without the knowledge, effort, and resources from all of you. I truly enjoyed the interdisciplinary research we had, and the interflow of ideas was amazing. Huge thanks to Zixin for helping me establish the test setups for the ionic devices and being knowledgeable and hands-on just as a proper mechanical engineer. To my collaborators in the SCSD McGill, Hideaki, Lisa, Andrew, and especially, Dr. Nicole Li-Jessen, thank you for providing me with the opportunity to apply my devices to solve a real-life clinically relevant challenge and introducing me to the world of voice and laryngeal health. Many thanks to Hideaki for the animal surgeries you performed with fantastic techniques and being so knowledgeable in the clinic. To Lisa, thanks for the valuable insights in voice pathology and always being so supportive in arranging everything and making sure all the human tests go smoothly. To my collaborators at INRS, Shengyun, Zhonglin, Ruiqi, and Dr. Dongling Ma, thank you for letting me explore the realm of nanomaterials. To Shengyun, thank you for teaching me the synthesis of nanowires and being so kind to give me a lift every time I go to INRS. To Zhonglin and Ruiqi, thanks for helping me with all the quantum dots and the laser experiments. To folks in the nano factory next-door, Lingzhi and Dr. Changhong Cao, thanks for the stunning SEM images you took and generously lend me your potentiostats. To Dr. Mazy, thank you for the meniscus 101 course and letting me be part of “save the meniscus”.

I would also like to appreciate the generous support from various funding agencies, including Natural Sciences and Engineering Research Council (NSERC), Fonds de recherche du Québec - Nature et technologies (FRQNT), and McGill Faculty of Engineering.

To friends outside research, your support is an integral part of my wonderful life throughout the past years. To Ari, thank you for being there for me, sharing laughter and tears. Your unique perspectives to the world and to life, your delightfulness, and your positivity shaped who I am today. To my gym buddy, Jiawei, thank you for coaching me and always pushing me through my physical limits. Your company in the gym is what helped me maintain my physique and keep me mentally healthy. To my gaming buddy, Lingzhi, thanks for all those game nights that I had so much fun and relief. Let’s go save the world! To my friends back on the other side of the earth, Tian, Yanxiang, Xun, Yuanpeng, and Zikun, although you are not physically with me these years, thank you for chatting with me from time to time. Knowing that there is someone always supporting you is the happiest thing.

Finally, I would like to express my deepest gratitude to my family for their unconditional support and love. To mom and dad, my gratitude is beyond words. Thank you so much for supporting me all these years and always believing in me. Love you!

Contribution to Original Knowledge

The body of work presented in this thesis contributed to the advancement of original knowledge to the field of ionotronics in four aspects, pertaining to a novel printable and tough material system, a new multi-material 3D printing strategy leveraging ionic microgels, a new equivalent circuit model for theoretical analysis of the faradaic rectification process, and four original 3D-printed multi-component ionic devices.

A **novel material system** composed of negatively charged polyacrylic acid (PAAc) and positively charged chitosan (Chit) is developed. The injectable and printable PAAc/Chit hydrogel features a phase transition process for substantial mechanical enhancement that can be triggered by benign physiological conditions such as water and body fluid. The macromolecular crosslinkers bypass the use of cytotoxic monomers and crosslinkers and are able to form stretchable hydrogel network through pure physical interactions.

An **innovative multi-material 3D printing method**, named 3D ionic microgel printing, is developed for the fabrication of ionotronics. The versatile strategy leverages microgels as the vessel to hold diverse ionic species as printable ionic ink modules and enables multi-material 3D printing into various device units in multi-component ionotronic devices. With the double-network design, the 3D-printed ionotronics are stretchable and tough and feature robust inter-component integration post-crosslinking.

A **novel equivalent circuit model** is established for ionic junctions composed of two oppositely charged hydrogels. The model is the first to quantitatively describe the faradaic current rectification process of hydrogel ionic junctions using fittings parameters with physical meanings.

A greatly **expanded device arsenal** based on printed ionic junctions is demonstrated. Four ionotronic devices, including ionic diodes, ionic transistors, ionic rectifiers, and ionic touchpads are successfully 3D-printed and characterized.

The aforementioned contributions have been consolidated in the preparation or publication of the following peer-reviewed journal articles:

1. **Huo, R.**, Bao, G., He, Z., Li, X., Ma, Z., Yang, Z., Moakhar, R., Jiang, S., Chung-Tze-Cheong, C., Nottegar, A., Cao, C., Mahshid, S. and Li, J.*, Tough Transient Ionic Junctions Printed with Ionic Microgels. *Adv. Funct. Mater*. 33, 2213677 (2023).
2. Ma, Z.†, **Huo, R.** †, Nottegar, A., Chung-Tze-Cheong, C. and Li, J.*, Bioinspired Printable Tough Adhesive. *Adv. Funct. Mater*. (in review) (2023).

In addition, the author has contributed to the following works during his Ph.D. studies listed in chronological order, including journal articles, patents and disclosures, and conference proceedings. Unpublished works are not included here.

- Peer-reviewed journal articles
    1. Ma, Z., Yang, Z., Gao, Q., Bao, G., Valiei, A., Yang, F., **Huo, R.**, Wang, C., Song, G., Ma, D., Gao, Z.H. and Li, J.*, Bioinspired tough gel sheath for robust and versatile surface functionalization. *Sci. Adv.* 7, (2021).

       Contributions: Designed and implemented the ex-vivo tissue friction and drag measurement.
    2. Bao, G., **Huo, R.**, Ma, Z., Strong, M., Valiei, A., Jiang, S., Liu, S., Mongeau, L.* and Li, J.*, Ionotronic Tough Adhesives with Intrinsic Multifunctionality. *ACS Appl. Mater. Interfaces* 13, 37849–37861 (2021).

       Contributions: Designed and conducted the experiments involving the study of electromechanical coupling effect and demonstration of the wearable strain sensor. Designed and implemented the burst pressure measurement and created illustration figures for the experimental setup.
    3. Ma, Z., Bourquard, C., Gao, Q., Jiang, S., De Iure-Grimmel, T., **Huo, R.**, Li, X., He, Z., Yang, Z., Yang, G., Wang, Y., Lam, E., Gao, Z.H., Supponen, O.* and Li, J.*, Controlled tough bioadhesion mediated by ultrasound. *Science* 377, 751–755 (2022).

       Contributions: Conducted experiments and analyzed data involving the investigation of ultrasound-induced thermal effect.
    4. Li, X., Liu, Y., Li, L., **Huo, R.**, Ghezelbash, F., Ma, Z., Bao, G., Liu, S., Yang, Z., Weber, M.H., Li-Jessen, N.Y., Haglund, L.* and Li, J.*, Tissue-mimetic hybrid bioadhesives for intervertebral disc repair. *Mater. Horizons* 10, 1705–1718 (2023).

Contributions: Designed and fabricated the ex-vivo biomechanical setup for physiological cyclic loading and failure tests.

5. Yang, Z., Bao, G. †, **Huo, R.** †, Jiang, S., Yang, X., Ni, X., Mongeau, L., Long, R. and Li, J.*, Programming hydrogel adhesion with engineered polymer network topology. *Proc. Natl. Acad. Sci.* 120, e2307816120 (2023).

   Contributions: Performed material synthesis and carried out the experiments related to adhesion of tough hydrogel with dangling chains on tissue surfaces. Designed and fabricated apparatus for the demonstration of soft robotics.
6. Mazy, D., Chung, C., Ma, Z., **Huo, R.**, Lamer, S., Li, J.* and Nault, M. L.*, Tough Gel Adhesive is an Effective Method for Meniscal Repair in a Bovine Cadaveric Study. *J. Exp. Orthop.* (In press) (2023).

   Contributions: Designed and fabricated the ex-vivo biomechanical setup for cyclic loading tests.

- Patents and disclosures
  1. **Huo, R.**, Phillips, D.M., Li, J. and Selmani, S., "Bioreactor for biomechanical characterization" (2020).
  2. **Huo, R.**, Huang, S. and Li, J., Viscoplastic nanocomposite conductors, (2023).
- Peer-reviewed conference proceedings
  1. **Huo, R.**, Phillips, D.M. and Li, J., "New Bioreactor Design for Intervertebral Disc", poster presentation at 2019 Int. Mechanical Engineering Cong. & Expo. (IMECE), Salt Lake City, UT, USA, Nov. 10-14, 2019.
  2. **Huo, R.**, Li, X., Liu, Y., Phillips, D.M. and Li, J., "Intervertebral Disc Bioreactor with Complex Loadings", poster presentation at 2022 Tissue Engineering and Regenerative Medicine International Society (TERMIS-AM), Toronto, ON, CA, July 10-13, 2022.
  3. **Huo, R.** and Li, J., 3D Ionic Microgel Printing of Degradable Ionic Junctions", oral presentation at 2022 Materials Research Society (MRS) Fall Meeting & Exhibit, Boston, AS, US, Nov. 27 – Dec. 2, 2022.

Contribution of Authors

The successful completion of this thesis could not have been realized without the collaborative research efforts from my Ph.D. advisor, colleagues, and collaborators. This section listed the specific contributions.

The author of this dissertation is responsible for conceptualization of the material systems and fabrication techniques, synthesis of materials, design and execution of experimentation, data analysis and visualization, as well as writing, editing, and reviewing of all the chapters in this dissertation. Note that my Ph.D. advisor, Prof. Jianyu Li, offered invaluable insights that contributed to the conception of the materials and the design of the experiments throughout this thesis. Other coauthors' contributions are described below.

In Chapter 3, Dr. Zhenwei Ma contributed significantly to the conceptualization of the material system, material synthesis, as well as design and implementation of the experiments and analyzation of the experimental data pertaining to the mechanical enhancement effect, pH-induced phase transition mechanism studies, effect of the covalent coupling reagents, adhesion performances. He also contributed to conceiving the ideas and designing of the experiments related to the study of polymer ratio, polymer content, kinetics, and the demonstrations of printed tissue mimetics, patterned adhesion, and 3D-printed morphing structures. Alex Nottegar and Christopher Chung-Tze-Cheong contributed to the material synthesis, as well as design and conduct of experiments related to the phase transition mechanism study including polymer ratio, polymer content, kinetics, and pH effect. Alex Nottegar also analyzed the data. Christopher Chung-Tze-Cheong synthesized the materials and conducted experiments for the rheological investigations including printing time window, shear yielding, shear thinning, and self-recovery. He also assisted with data collection for the experiments pertaining to the electrical and electromechanical coupling effect, as well as the demonstrations of the strain sensor. Prof. Jianyu Li supervised the project.

In Chapter 4, Dr. Guangyu Bao conceived the idea and conducted experiments related to the ionic microgel synthesis, analyzed the data associated with the distribution of the ionic microgels, designed and performed experiments regarding the printing resolution investigation, and analyzed the corresponding data. Zixin He designed and built the data acquisition system for the demonstrations of ionic full-wave rectifier and the ionic touchpad. Xuan Li contributed to the fabrication and implementation of the demonstrations involving the ionic touchpad. Dr. Zhenwei Ma contributed to designing and conducting the in vitro degradation experiments. Dr. Roozbeh Moakhar and Prof. Sara Mahshid contributed to analyzation of the electrochemical impedance spectroscopy data and assisted in conceiving the design of equivalent circuits. Zhen Yang assisted in the analyzation of the experimental data involving the mechanical testing including pure shear and t-peeling. Shuaibing Jiang assisted in the illustration of the chemical structures. Christopher Chung-Tze-Cheong and Alexander Nottegar assisted in the ionic microgel synthesis and ionic transistor fabrication. Prof. Changhong Cao assisted in providing the potentiostats for the electrochemical measurements. Prof. Jianyu Li supervised the project.

Abbreviations

3D	three-dimensional
4D	four-dimensional
ac	alternating-current
AF	annulus fibrosus
Agar	agarose
AgNW	silver nanowire
Alg	alginate
CAD	computer-aided design
Chit	chitosan
CNC	cellulose nanocrystal
CNT	carbon nanotube
CS	chondroitin sulfate sodium
DAQ	data acquisition
dc	direct-current
DI	deionized
DIW	direct ink write
DLP	digital light projection
DN	double-network
DPBS	Dulbecco's phosphate-buffered saline
EDC	N-(3-Dimethylaminopropyl)-N'-ethylcarbodiimide hydrochloride
EDL	electrical double layer
G'	storage modulus
G"	loss modulus

GF	gauge factor
I2959	2-hydroxy-4′-(2-hydroxyethoxy)-2-methylpropiophenone
IMP	ionic microgel printing
IVD	intervertebral disc
LCD	liquid crystal display
LiCl	lithium chloride
MBAA	N,N′-methylenebis(acrylamide)
$\mathbf{N_2}$	nitrogen
NaCl	sodium chloride
NHS	N-Hydroxysuccinimide
NP	nucleus pulposus
PAAc	polyacrylic acid
PAAm	polyacrylamide
PAMPS	poly(2-acrylamido-2-methylpropanesulfonic acid)
PAT	poly (1-[2-acryloyloxyethyl]-3-butylimidazolium bis[trifluoromethane] sulfonimide)
PDAC	poly (diallyldimethylammonium chloride)
PDMAPAA-Q	poly(3-acryl- amidopropyl trimethylammonium chloride)
PDMS	polydimethylsiloxane
PEG	poly(ethylene glycol)
PEGDA	poly(ethylene glycol) diacrylate
PET	polyethylene terephthalate
PES	poly (1-ethyl-3- methyl imidazolium [3-sulfopropyl] acrylate)
PLA	polylactic acid
PMMA	polymethyl methacrylate

PMPTC	poly(3-(methacryloylamino)propyl-trimethylammonium chloride)
PPy	polypyrrole
PSPA	poly(3-sulfopropyl acrylate)
PSS	poly(sodium 4-styrenesulfonate)
PT	phase-transitioned
PVBPPh$_3$	poly(vinylbenzyl chloride) quaternized by triphenylphospine
QC	quaternary chitosan ammonium
RMS	root mean square
SEM	scanning electron microscopy
SLA	stereolithography
SLS	selective laser sintering
SN	single-network
TENG	triboelectric nanogenerator
TPP	two-photon polymerization
UV	ultraviolet
VHB	very high bond

Table of Contents

List of Figures

List of Tables

CHAPTER 1

Introduction

This chapter serves as a general introduction to the thesis. The chapter begins with a thesis organization section to explain the overall format and provide an overview of the chapter arrangement, including a brief summary for each chapter. It is followed by a thesis motivation section to provide backgrounds and a challenge section to state the main obstacles to be tackled in hydrogel ionotronics. The chapter continues with a comprehensive literature review section to summarize previous relevant studies and provide fundamental theories. Next, the rationale for conducting this research is stated and detailed objectives for subsequent studies toward addressing the research problems are presented.

1.1 Thesis Organization

This thesis is written in traditional monograph style, including 6 chapters – Introduction, Materials and Methods, 3D printing of polyelectrolyte complex hydrogels, 3D ionic microgel printing of ionic devices, Discussions, and Concluding remarks – overviewed as follows.

Chapter 1 serves as a broad introduction to the thesis. It starts with explaining the background of developing hydrogel ionotronics and is followed by articulating the contextual challenges in the design and fabrication of high-performance hydrogel ionotronics. With the research obstacles and related problems established, a thorough background survey of existing theories and techniques developed in the literature is provided. The literature review is divided into four major subsections. The first subsection provides background information on the advances in ionotronics, mainly focusing on hydrogels. The second subsection specifically discusses multiple desired material properties for hydrogel ionotronics, including conductivity, self-healing, and environment stability. Next, fabrication methods for hydrogel ionotronics are introduced with a highlight in 3D printing technologies. The last part of the literature review surveys the existing hydrogel ionotronic devices, including strain and temperature sensors, triboelectric nanogenerators, and bioelectronic interfaces. Finally, the rationale for conducting the research is clarified and the detailed aims and approaches toward addressing the research challenges are explained.

Chapter 2 focuses on the numerical and experimental methods used throughout the entire thesis. This chapter is divided into six sections, describing the synthesis of materials, characterizations, and fabrication of devices. In the first section, materials synthesis procedures, including the polyacrylic acid/chitosan (PAAc/Chit) polyelectrolyte complex hydrogels, the Agar/PAAm double-network (DN) hydrogels and microgel inks, and 3D printing of the materials are detailed. The next section focuses on the physical and structural characterizations conducted on the materials, comprising swelling tests, degradation, and microscopic imaging. It is followed by a mechanical characterization section to explain the approaches used in investigating the rheological properties, tensile properties, fracture toughness, and adhesion performances. The fourth section details the experimental techniques pertaining to electrical functions, specifying measurements in electrical conductivity, electromechanical coupling, and electrochemical performances. In the next section, relevant details in the fabrication and characterization of the ionotronic devices constructed in this thesis are presented, namely, ionic bipolar junction transistor, ionic full-wave rectifier, and ionic touchpad. Finally, methodologies pertinent to statistical analysis throughout this thesis are described.

Chapter 3 and Chapter 4 comprise the main body of the thesis presenting key results and findings of two subsequent studies towards solving the research challenges. In Chapter 3, a 3D-printable, tough, and adhesive PAAc/Chit hydrogel is presented featuring a unique phase transitioning mechanism for printable inks to experience mechanical enhancement in ubiquitous and mild environments. The developed material system targets the research problem to simultaneously achieve printability and mechanical robustness. The results and analysis related to the 3D printing quality, mechanical performances, phase transition mechanisms, electrical behavior, and demonstrations of applications are presented. Despite the advances, the proposed PAAc/Chit material system still has limitations, for instance, compromised electrical conductivity, limited electrical functionality, and drastic size changes. These drawbacks hamper the further application of this material in fabricating ionotronic devices. Therefore, Chapter 4 introduces the development of 3D Ionic Microgel Printing (3D IMP), a versatile multi-material 3D printing method for hydrogel ionotronics. This 3D printing strategy incorporates a combination of ionic species–contained microgels and DN crosslinking technology. By leveraging the intrinsic printability of the ionic microgels, the microgel-reinforced toughening mechanism, and the modularity of the microgels to host ionic species and support diverse ionic functions, the 3D IMP technique emerges as a promising approach to address the challenges in the fabrication of multi-component ionotronics. Results and analysis pertaining to the material design, 3D printing, electrical investigations, mechanical performances, and the fabrication of various ionotronic devices are presented.

Chapter 5 provides a comprehensive discussion on the findings of the reported technologies. The chapter is divided into four sections. The first three sections discuss the three key ingredients of the presented research, namely, 3D printing, mechanical integrity and degradation, and electrical characteristics. Each topic is elaborated with the highlights, implications, comparisons to the literature, limitations, and potential improvements. With the identified merits and drawbacks, a section devoted to future directions follows. Perspectives and proposals on the development of next generation high-performance ionotronics are put forward.

The last chapter is dedicated to final conclusions and remarks. The outcomes of this thesis are summarized corresponding to the proposed objectives, and its contributions to the advancement of knowledge in the field of ionotronics are emphasized.

1.2 Thesis Motivation

Electronics devices have become an integral part of every facet of modern life, ranging from entertainment to office productivity, industrial applications, and healthcare. Over the past decade, the trend in commercially available wearable technology and a shift toward digital precision medicine have driven the development of a new class of electronics. Wearable and implantable technology can promote convenient and long-term continuous communications between the physiological environment and electronics. Take healthcare as an example, a better machine-to-human interface would assist in faster, safer, more accurate, and more comprehensive health monitoring. It would further contribute to benefits in diagnosis, therapeutics, rehabilitation, and foster a deeper understanding in the physiology of the human body.

Conventional electronics achieve various functions via the integration of diverse electronic elements. Electrical conductors are indispensable elements responsible for transmitting electrical signals and delivering power. Typically composed of metals, these conductors play a vital role in various electronic devices. On the other hand, electrical p-n junctions, commonly made of semiconducting materials, are another types of crucial elementary building block for a myriad of electronic components, including diodes, transistors, light-emitting diodes, solar cells, and integrated circuits[1]. Whereas conventional electrical materials are intrinsically inorganic, rigid, and electronic, most human tissues are organic, soft, and ionic. The distinct nature of the physical, mechanical, and electrical properties in those two systems presents a significant hurdle in achieving physical integration. Consequently, bridging this gap stands out as a fundamental challenge in the pursuit of effective communication between electronic devices and biological systems. The necessity for machines to be soft, stretchable, and ionic to seamlessly integrate with the human body has become increasingly evident.

Tremendous research efforts have been made to render electronics flexible and stretchable, matching the mechanics of soft biological tissues. Early approaches achieved this by engineering the structure (e.g., serpentine and horseshoe shaped metal conductors) and exploiting the mechanics of traditional materials (e.g., flexible thin silicon wafer)[2–4]. Other methods utilized strategies to bind stretchable substrates with rigid electronic components and connect with stretchable conductors[5–7]. Despite the preserved high performances offered by conventional materials, these methods often yielded unsatisfactory stretchability in dynamic environments along with concerns related to stress concentrations and mechanical durability. To circumvent such issues, other emerging methods are being explored, focusing on material chemistry to develop fully stretchable devices. To achieve this, numerous intrinsically stretchable polymeric electronic materials have been created[8–11]. However, sophisticated design and complex processing were inevitable in all the aforementioned strategies[3,12,13]. Such approaches were often time-consuming and tethered to stringent processes and expensive fabrication environments.

Whereas conventional electronics struggle to address the abovementioned challenges, their ionic counterparts – ionotronics – stand as a promising alternative. Ionotronics can fulfill a variety of electrical functions that are the same as electronics but via different charge carriers. While electronic conductors convey electrical signals via electrons, ionic conductors do so via positive and negative ions[14–19]. Analogous to a depletion region formed between electron-rich and hole-rich units of electrical p-n junctions, ionic junctions rectify ionic current with an ion-depletion region at their interface of oppositely charged ionic units. With ions as the main charge carriers, ionotronics resemble the human body. The same electricity conduction mechanism promotes electrical communication and facilitates their integration, which remains challenging for electronics due to the charge carrier mismatches. Among the various materials that comprise ionotronics, hydrogels are one of the most popular classes. Hydrogels comprise hydrophilic polymer chains that swell in water. Polymer matrices serve as vessels to hold water, while water acts as medium for ions to transport. The intrinsic organic, soft, wet, and ion-rich features render hydrogels affinity to biological tissues in terms of physical composition, mechanical characteristics, and charge carriers. Thanks to the extensive development of this engineering material, multiple salient features and properties have been endowed to hydrogels that can also benefit iontronics, such as giant stretchability[20], toughness[21], fatigue resistance[22], self-healing[23,24], ambient stability[25], and freeze tolerance[26]. With the advances in hydrogels, diverse functions has been demonstrated in hydrogel ionotronics, such as current rectification[27,28], computing[29,30], energy generation and harvesting[31–35], sensing[25,36], neural modulation[37], and adhesion[38].

The mainstream fabrication method for hydrogel ionotronics is batch synthesis and manual assembly. These methods cannot produce hydrogels with intricate, small-scale, and precise structural features, nor can they assemble dissimilar hydrogels or hydrogel with other materials with high precision. These drawbacks fundamentally constrain the geometrical fidelity and design flexibility, and thus limit the electrical functions of the resulting ionotronic devices. The advancements in these properties are critical for high-performance hydrogel ionotronics with multiple ionic units[39]. 3D printing has emerged as a promising additive manufacturing strategy to control the architectural features of various structural and functional materials, including hydrogels. The current paradigm for 3D printing of hydrogels is depositing the inks of hydrogel precursors into desirable 3D shapes, predominantly through techniques such as direct ink writing (DIW)[40], embedded printing[41], or vat-photopolymerization[42], and then curing the inks post- or during printing[43]. The small feature size, high precision, and intricate architecture offered by 3D printing can readily address the aforementioned challenges in the fabrication of hydrogel ionotronics. Among all the 3D printing techniques, DIW is the most popular one used for hydrogel ionotronics due to its accessibility, facile operation, and multi-material printing capability.

1.3 Challenges

Implementing 3D printing to hydrogel ionotronics could provide a solution for high-performance ionotronics, but two main challenges remain. First, a recognized issue with DIW of hydrogel ionotronics is the tuning of different 3D-printable inks, which often demands time-consuming and delicate refinement of the rheology and printing conditions of the respective inks to ensure printing quality[44,45]. Considerations of the mechanical properties pertaining to the stretchability, strength, and toughness as well as other electrical functionalities of the post-printed devices further complicate the ionotronic material design process. The often-contradictory design criteria for ink printability and toughness of most existing hydrogels bring significant hurdles for the widespread and rapid implementation of DIW in hydrogel ionotronics.

Second, developing hydrogel ionotronics with new conceptual functions expects the involvement of various hydrogel materials with dissimilar physical, chemical, and electrical properties. 3D printing of such heterogeneous ionotronic devices requires the development of compatible multi-material strategies, where multiple ionic units are constructed with a variety of hydrogel inks. The inter-material contamination caused by ink mixing and diffusion during or after fabrication will adversely affect the performance of 3D-printed devices or even prematurely demolish device functions. Achieving reliable adhesion between dissimilar units for a cohesive device also remains a challenge[46]. Debonding of units would impair or affect the device performance during use and undermine the stretchability and toughness of the whole device.

1.4 Literature Survey

1.4.1 Hydrogel ionotronics

Inspired by living matters, ionotronics are devices with hybrid circuits that conduct current via a combination of both ions and electrons[14]. In ionotronics, ions are the major charge carrier that fulfill device functions, while electrons are involved in connection to external circuits for input and output of power and signals. Early ionotronics took the form of electrolyte solutions or ionic liquids encapsulated in vessels with channels and reservoirs. However, the liquid nature of these ionic conductors poses issues such as leakage and strong dependence on the vessels, which hindered their further development[18]. Therefore, hydrogels, as solid ionic conductors, have risen to become the main form of ionotronics.

Hydrogels are a promising candidate for ionotronics due to their combination of desirable mechanical, chemical, and electrical properties. Hydrogels compose of polymer networks and a large amount of water. In hydrogels, water hold ions and support their transportation, while the polymer networks maintain their solid shapes[14]. Hydrogels have been synthesized with tailored mechanical properties to match a range of biological materials and soft tissues[47]. The high biocompatibility of hydrogels can attenuate the foreign body response and make them suitable candidates for biomedical applications such as drug delivery, tissue engineering, and regenerative medicine[48,49]. Recent research has also highlighted various aspects of hydrogels, including high fracture toughness[20], adhesion energy[50], and ionic conductivity[51]. These properties can further facilitate hydrogels applications in wearable electronics[19], bioelectronics[52], and soft robotics[53].

1.4.2 Properties desired for hydrogel ionotronics

Conductivity. Ionic conductivity is enabled by the motion of ions[54]. The foundation of stretchable ionotronics is established by stretchable ionic conductors. Other ionic functions are enabled by the inclusion of additional ionic species. Hydrogels achieve ionic conductivity mainly by diffusion of ions driven by electric fields, concentration gradients, or temperature[18]. In hydrogels, the mesh size of the polymer networks (~10 nm) is much larger than that of ions; ions carrying charges can drift under an applied electric field with water as the supporting medium to achieve ionic conduction. Introducing mobile ions by dissolving salts in neutrally charged polymer networks is one of the pioneering methods to endow ionic conductivity. For example, the resistivity of polyacrylamide (PAAm) hydrogels can be decreased to 0.02 Ωm, 0.03 Ωm, and 0.05 Ωm with the addition of 1.37M, 2.74M, 5.48M of NaCl respectively, compared to 18.2 MΩm of resistivity for deionized water[51]. Another method is the inclusion of charged polymers – polyelectrolytes – into hydrogel networks[19]. Polyelectrolytes are a type of polymer with charge-carrying groups in their repeated units and associated mobile counterions. Typical polyelectrolytes used in ionotronics include PAAc, poly (sodium 4-styrene sulfonate) (PSS), poly (diallyldimethylammonium chloride) (PDAC), poly(3-(methacryloylamino)propyl-trimethylammonium chloride) (PMPTC), and poly(2-acrylamido-2-methylpropanesulfonic acid) (PAMPS). Due to the charged polymer backbone, hydrogels with polyelectrolytes only allow the transport of mobile ions with opposite charge, leading to selective conductivity.

Whereas pure hydrogel ionic conductors have limited conductivities of < 10 S m^{-1}, the inclusion of other conductive fillers can enhance their conductivity. Some electrically conductive fillers that have been added to hydrogels include conductive polymers such as polypyrrole (PPy)[55] and polyaniline (PANI)[56], as well as inorganic inclusions such as metal nanowire[57], micro/nanoparticles[57,58], carbon nanotubes[59–61], carbon black[62], reduced graphene oxide[63–65], and graphite[66]. In addition, there also exist polymers that render mixed ionic-electronic conductive strategies[67] – the well-studied poly(3,4-ethylenedioxythiophene) polystyrene sulfonate (PEDOT:PSS) being one of them[67–69].

Self-healing. Self-healing capability enables hydrogel ionotronics to recover both mechanical and electrical performances repeatedly after mechanical damage[59,70–72]. Damage in hydrogel ionotronics can arise from notching, tearing, stretching, and puncturing. The damages may not lead to complete rupture of the device but risk compromising the electrical function and durability[23]. Therefore, self-healing of material components after mild damage is a desirable feature for hydrogel ionotronics to prolong device lifespan.

Current self-healing strategies in hydrogel ionotronics can be categorized into external stimuli-induced and autonomous[71]. External stimuli-induced self-healing is accomplished either by incorporating self-healing agents into the material and releasing them at damage sites or by initiating the reformation of polymer networks through heat[73]. However, limitations such as consumption of self-healing agents and inconvenience in applying heat bring hurdles to their practical application. To this end, increasing attention has been drawn to the development of autonomous self-healing hydrogels[74]. Autonomous self-healing takes advantages of the spontaneous interactions of moieties in the hydrogel polymer networks, where bonds can be reformed after broken[75,76]. Some interactions rely on dynamic chemical bonds such as disulfide bond[77,78], acylhydrazone bond[79], phenylboronate ester bond[80], diol-borate eater bond[59,65,81], Diels-Alder reaction[82], and Schiff's base reaction[83,84]. Other mechanisms are based on dynamic noncovalent bonds including hydrogen bonding in polyvinyl alcohol (PVA)[85], chitosan-based[86], and hyaluronic acid-based hydrogels[87], ion interactions (metal-coordination) in PAA hydrogels[88], host-guest interactions[89,90], and hydrophobic interactions[91].

Environment stability. Environment stability for hydrogels mainly involves the capabilities of anti-freezing and water-retention. Resilience to temperature and humidity changes is especially important for hydrogel ionotronics when used as wearable devices. Under ambient conditions, hydrogels spontaneously lose water by evaporation. Reduced water content will stiffen the resulting hydrogel and eventually yield a brittle material that is prone to rupture under dynamic deformations. Ion mobility will also be attenuated due to the loss of transportation medium and denser polymer network. Strategies to prevent evaporation and decrease the freezing point of hydrogels can be categorized into two streams: inclusion of hygroscopic matter and encapsulation of elastomer layers.

The most used hygroscopic matters in hydrogels are cellulose[92], sugar[93], and salts[25,94,95] – including lithium chloride and sodium chloride – which have proven to hold water molecules in hydrogels due to their strong bond strength between dissolved cation/anion and the water molecule pairs. Organic solvents are another type of hygroscopic material that could prevent water loss and endow anti-freezing capability to hydrogels, including glycerol[96], ethylene glycol[25], and sorbitol[97]. However, drawbacks – including health hazards, reduced ionic conductivity, and deteriorated toughness are major concerns to these inclusions[74].

Encapsulation of hydrogel ionotronics with elastomer layers is another simple and effective method to achieve water retention while minimally affecting the electrical and mechanical functions of the devices. In this case, strong adhesions at the elastomer-elastomer and hydrogel-elastomer interfaces are necessary. Strategies include oxygen plasma treating of the elastomer surfaces[98] – introducing silane for siloxane bonds[99] – and benzophenone-treated elastomer for covalent bonding with hydrogels[100,101].

1.4.3 Fabrication of hydrogel ionotronics

Hydrogel ionotronics typically consist of multiple components. The device fabrication processes involve the synthesis of each material component, integration of the components, and encapsulation of the whole device. In this section, we will be mainly discussing two of the existing methods for fabricating hydrogel ionotronics: molding and assembly and 3D printing.

Molding and assembly. Molding and assembly is the most used method in fabrication of hydrogel ionotronics due to its simplicity and intuitive process, adopted from traditional hydrogel synthesis. Components of a device, usually including conductive hydrogels, dielectric elastomers, and encapsulation layers, are first molded from their precursors. Upon solidification, each material is harvested from the molds and cut to designed shapes and sizes. Finally, layers of materials are laminated manually in designed sequence and special arrangement with or without adhesion treatments to construct the hydrogel ionotronics.

Despite the intuitive fabrication process, drawbacks related to this method stand to be one of the most significant impediments to the further development of hydrogel ionotronics. The major issue is that, since molding and assembly method relies on manual assembly of each component, shapes and spatial position varies across each individual device, therefore, it suffers from low repeatability in terms of device performance. In fact, the functionalities of such devices could only remain in the proof-of-concept stage. In addition, features in nanometer and micrometer scale cannot be achieved, which is a significant obstacle in reducing component size, increasing the number of units packed in one device, and further improving device performances and multifunctionality[39]. Additionally, the unstandardized process is not able to support large-scale production of hydrogel ionotronics for commercialization.

3D printing. 3D printing is an additive manufacturing approach to embody precise 3D architectures according to digital designs[102]. 3D printing of hydrogels arose from the application of 3D bioprinting for tissue engineering and has gradually spread to other fields of hydrogels. To accommodate for broader applications, one of the focuses is to develop 3D-printed strong and tough hydrogels, as summarized in Table 1.1. 3D printing has drawn increasing attention as a fabrication method for hydrogel ionotronics due to its advantages in producing intricate 3D patterning, fast prototyping for design iterations, and upscale potential[39].

Two general methods are typically used for 3D printing of hydrogel ionotronics: light- and extrusion-based[103], as shown in Figure 1.1. Light-based 3D printing, including stereolithography (SLA), digital light projection (DLP), liquid-crystal display (LCD), and two-photon polymerization (TPP), involves shining a focused laser beam or a projected light pattern onto a photopolymerizable resin, which trigger the photo-initiator inside the resin for polymerization and crosslinking of the hydrogel polymer networks. The laser beam is computer-controlled and can create a thin layer of hydrogel with accurate patterns. As the platform elevates, a layer-by-layer structured 3D hydrogel is formed. Printing quality depends on the laser wavelength, intensity, voxel size, scanning speed, as well as composition and concentrations of the chemical components.

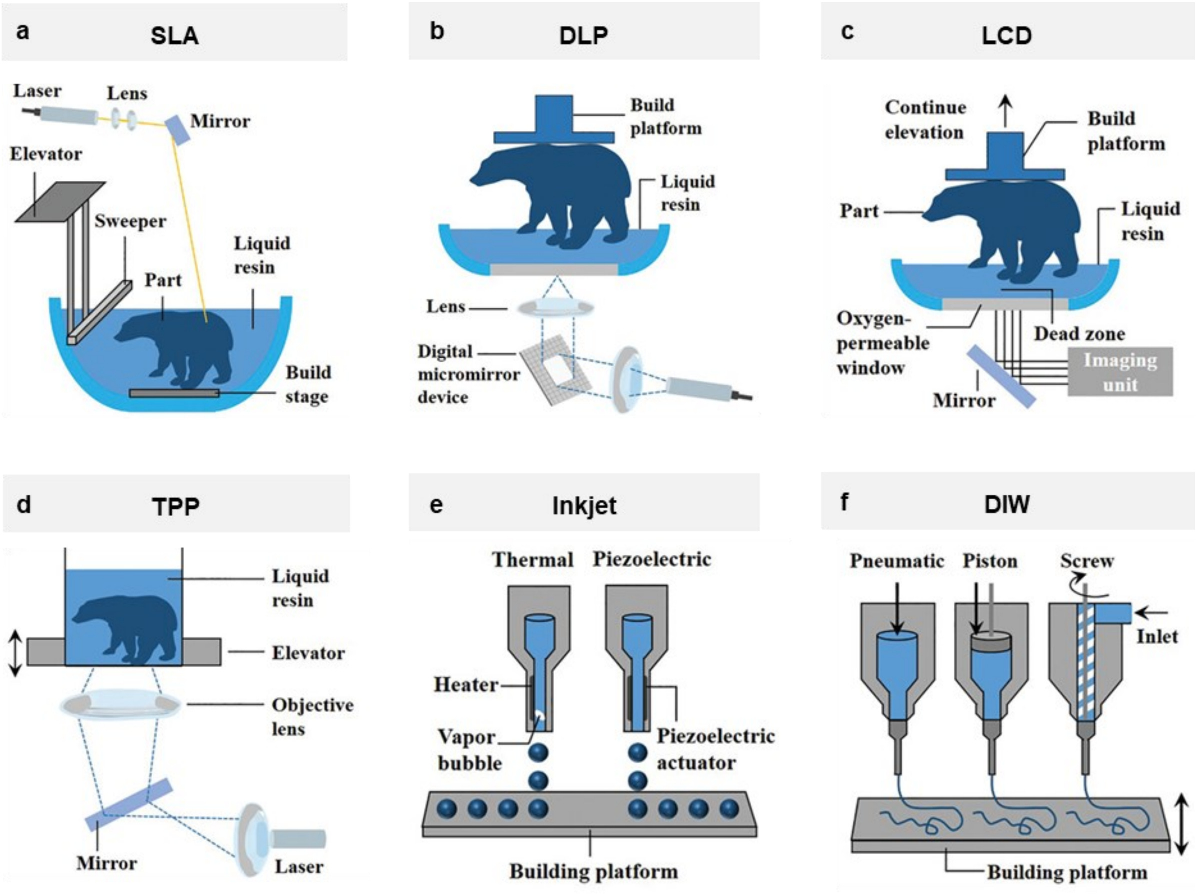

Figure 1.1. 3D printing techniques for hydrogels. (a) Light-based printing methods include SLA printing, (b) DLP printing, (c) LCD printing, and (d) TPP printing. (e) Extrusion-based printing methods include inkjet printing and (f) DIW printing. Reproduced with permission[103]. Copyright 2021, Wiley-VCH.

Extrusion-based 3D printing, including inkjet printing and direct ink writing (DIW), utilizes a robotic system to control the movement of an extrusion nozzle as drops or filaments of ink are extruded. DIW is the most popular extrusion-based 3D printing method to fabricate hydrogel ionotronics because of the wide selection of materials and tunability of most hydrogel precursors to meet the requirement of DIW. Continuous flow of inks can be facilitated with shear thinning behavior, where viscosity decreases with shear rate. A properly designed ink material also necessitates suitable yield stress to allow yielding when extruded out from the nozzle under external pressure while preventing yielding before or after extrusion to hold the printed structures.

In addition, to stabilize the post-printed structures and render properties such as high stretchability, strength, and toughness, a post-processing step such as UV crosslinking, heating, or ionic crosslinking is often required. This demands such triggerable mechanical enhancements to be encoded in the hydrogel inks during material design. As a burgeoning field, current research in 3D-printed hydrogel ionotronics has been focusing on balancing the printability and device functionality such as stretchability, adhesion, and ionic conductivity. This stems from the fact that DIW requires inks with proper rheological properties to generate successful prints with high resolution and shape fidelity, while the addition of electrical or mechanical functional components normally alters the rheological properties of the ink. Thus, optimization of the ink to produce printable, stretchable, and conductive materials is necessary.

Table 1.1. Summary of materials, printing methods, printing resolution, and mechanical properties of 3D-printed hydrogels.

Material	Method	Resolution (µm)	Elastic modulus (kPa)	Max strain (%)	Tensile strength (kPa)	Toughness (kJ m^{-3})	Fracture toughness (J m^{-2})	Ref.
PAAm/Alg	DIW	300	66	300	170	260	-	[104]
PAAm/Agar/Alg	DIW	-	810	691	781	3860	-	[105]
PAAm-Zr4+	DIW	330	10000	150	2000	2000	-	[106]
PAAc-Zr4+	DLP	100	570	955	1350	-	-	[107]
P(AAc-co-AAM)	DIW	500	520	353	1520	-	-	[108]
PAMPS/PAAm	DIW	500	440	923	1400	3024	-	[109]
PAMPS/PAAm microgel	DIW	500	480	5000	1000	660	-	[110]
PAMPS/PAAm microgel	DIW	210	300	1600	1200	-	15000	[111]
PAMPS/PAAm microgel	DIW	-	-	280	470	-	3000	[112]

PEG/Alg/ nanoclay	DIW	500	-	500	250	-	1500	[113]
PVA/Chit	DIW	200	14000	302	1271	22100	9920	[114]
PMPTC/PSS	DIW	180	2600	530	1200	-	-	[115]
PMPTC/PSS	DIW	500	10200	700	3400	-	9500	[116]
PMPTC/PSS/CNT	DIW	280	4470	475	1690	-	-	[117]

1.4.4 Applications of hydrogel ionotronics

The applications of hydrogel ionotronics have demonstrated various functions. Stretchable ionic conductors have been incorporated in diverse emerging ionotronic devices, encompassing artificial skins[118], axons[119], muscles[51], eel[120], luminescent fiber[121], thermometer[122], neural interfaces[123,124], ionic eye[125,126], and triboelectric nanogenerators (TENG)[127,128]. In this thesis, we highlight the development and functionalities of several emerging applications for hydrogel ionotronics including biophysical sensors, TENG, and bioelectronic interfaces.

Biophysical sensors. Hydrogel biophysical sensors, typically in the form of wearable devices, detect physical changes of the body such as strains, pressures, and temperatures that have certain biomedical implications[19]. These physical stimuli are then transformed into electrical signals in forms of changes in current, voltage, resistance, and capacitance that can be measured and recorded by instruments. Hydrogel biophysical sensors have gained increasing interest to mimic the function of human skin. The development of artificial skins can find uses in biomedical applications including health monitoring, rehabilitation, and prosthesis. In this section, we will focus on resistive and capacitive strain and pressure sensors and hydrogel temperature sensors.

Strain and pressure sensors generate electrical signals upon mechanical deformation. Hydrogel resistive strain sensors function by coupling mechanical deformation-induced geometrical changes with the electrical resistance change. For resistive strain sensors, the gauge factor (GF) is defined as $GF = (\Delta R/R_0)/\varepsilon$, where ΔR is the change in resistance, R_0 is the resistance without deformation, and ε is the applied strain[129]. Ideally, the ionic conductivity of hydrogels remains unchanged during mechanical deformation, therefore, when hydrogels are stretched to λ times its original length, their resistance increase to λ^2 times their original resistance[14].

Compared to resistive strain sensors, capacitive sensors have the advantages of high linearity (even at large strain – up to 500%), low hysteresis, good mechanical durability, and robustness in material selection[85,88]. Capacitive strain sensors have been primarily used in pressure, tactile, elongation, and shear sensing. Hydrogel capacitive strain sensors consist of a dielectric layer sandwiched between two conductive hydrogel layers, with two electrodes contacting the hydrogel layers, connecting the device with external circuits[118]. At the electrode/hydrogel interface, an electrical double layer (EDL) forms, which behaves as a capacitor (C_{EDL}) with a capacitance far larger than that of the capacitor formed between a dielectric layer and a conductive hydrogel (C_D)[118]. The total capacitance of the capacitive strain sensor can then be modeled as two EDL capacitors and one dielectric capacitor in series, represented as: $1/C = 2/C_{EDL}+1/C_D$. Deformations can cause changes in both the dielectric layer thickness (d) and facing area (A) of the two conductive hydrogel layers; as the capacitance of dielectric capacitor can be equated as: $C_D = \epsilon A/d$, capacitance can then be coupled with deformation[118]. Under the assumption of constant dielectric constant (ϵ) of the dielectric material during deformation, capacitance scales as $C = C_0\lambda$ under uniaxial stretch λ and as $C = C_0\lambda^4$ under biaxial stretch.

Local temperatures of tissue microenvironments are important parameters to reflect physiological activities[130,131]. Accurate measurement of temperature on the surface of biological tissues as functions of both time and location and decoupled with deformations can be used to monitor health conditions, as well as to diagnose diseases and disorders including infections, traumatic injury, chronic inflammation, immunological irregularities, and transplant rejection processes[132,133]. Hydrogel temperature sensors of wide sensing range, high discernible resolution, and fast response are desirable[19]. Using PANI nanofibers, temperature sensing by resistance change was demonstrated. The hydrogel temperature sensor could response to sudden temperature variation with a sensing resolution of 2.7°C. The mechanism is based on varying carrier hopping rates among inter-fiber junctions at different temperatures[134,135]. Alternatively, a temperature sensor based on NaCl-PAAm conductive hydrogel has been demonstrated with high sensitivity (1.19 mV/°C). It utilized the self-generated voltage signal of EDL at the hydrogel-electrode interface in response to temperature change[136]. However, the aqueous nature of hydrogels makes such devices prone to accelerate evaporation at elevated temperature or freeze at subzero temperatures. Consequently, the temperature sensing range is significantly restricted.

Triboelectric nanogenerator. A TENG converts mechanical energy into electricity based on a conjugation of contact electrification and electrostatic induction[137]. With the advantages of simple structures, vast material choice, and multiple operating modes, TENG has been demonstrated to not only harvest energy for versatile applications, but also function as self-powered sensors to detect mechanical motions[138]. Hydrogel ionotronics TENG are flexible, stretchable, and transparent, suitable for both wearable and implantable biomedical applications. They have shown capacities in serving as energy source for therapeutics such as cardiac pacemakers[139,140], wound healing[141], osteoblast differentiation[142,143], and neural stimulation[144–147], as well as self-powered sensors for health monitoring and rehabilitation such as pulse[148–151], respiration[148,152], voice[153,154], and joint movement monitoring[155,156].

Hydrogel ionotronic TENG typically employs a sandwich-like architecture, with a piece of ionically conductive hydrogel sealed between two elastomer films, and two electrical conducting components attached to the hydrogel for electrical connection. Polydimethylsiloxane (PDMS) and VHB are the most used elastomer material, while PAAm with LiCl ions is the most popular conductive hydrogels[157]. Four types of working modes can be implemented: contact-separation mode, sliding mode, freestanding mode, and single-electrode mode – among which single-electrode and contact-separation mode are the most common ones[157]. Regardless of the mode, the working principle can be described briefly as follows[158]: when two dielectric materials with different electronegativity contact, charge will transfer between them according to their electron affinities (e.g., PDMS is triboelectrically negative, while skin is triboelectrically positive, so charge transfer from skin to PDMS, causing the PDMS layer to be negatively charged). Upon separation, the static charges on the surface of the elastomer layer will induce ion movement in the conductive hydrogel layer to locally balance the charge at the elastomer/hydrogel interface, which will further polarize the EDL at the hydrogel/electrode interface. To locally balance the EDL, electrons will flow in the electrode through external circuits until charges in elastomer layer are screened. Similar processes will occur with opposite charge directions when the dielectric material (skin) reapproaches the elastomer, thus, repetitive mechanical movement will lead to alternating current generation for device powering or self-powered sensing.

Bioelectronic interface. Bioelectronics directly interface with human body for electrical communication between biological environment and electronics, including electrical stimulation and bioelectricity sensing[52,159,160]. A successful bioelectronic interface requires seamless integration between target biological tissues and electrodes. Conformal mechanical contacts are the foundation for reliable electrical communications. The low moduli of hydrogel ionotronics ensure their mechanical integration with tissues, while the capability to form strong adhesions makes them more advantageous in long-term applications[124,161,162].

Surface hydrogel coatings and interfacing hydrogel adhesives manifest the two forms of hydrogel ionotronics as bioelectronic interfaces[163]. Surface hydrogel coatings are mainly implemented under the scenario of coupling bioelectronics with surrounding biological fluids, while interface hydrogel adhesives bond bioelectronics with biological tissues. Regardless of the form, to achieve spatially precise electrical communication between each electrode and specific regions of the tissue, electrical signals need to be conducted directly from the electrode through the hydrogel layer and to the target tissue. In this case, conductivity of hydrogel interfaces stands to be a crucial factor to be considered for the structural design of the hydrogel layer. When hydrogel interfaces have conductivity similar to local tissues (~0.5 S m^{-1} at 1 kHz), a simple uniform layer of conductive hydrogel can serve as the interface, due to the spatially resolved ionic conduction, where electrical signals can be transmitted along the thickness direction of the hydrogel with low interference from neighboring electrodes[163]. Recent studies have taken advantages of this salient feature in ionic conductivity to implement hydrogel bioelectronic interfaces in multiple biomedical setups, including electrical stimulation devices such as cardiac pacemakers[124] and neural cuff electrodes[164], and biopotential sensors such as multielectrode array[124], epicardial potential mapping electrodes[165], and electrocorticography electrodes[166]. On the other hand, low conductivity is not always desired, while island-structured hydrogel layers are required for hydrogel interfaces with high conductivity to be implemented with electrical stimulation devices.

1.5 Thesis Objectives

Wearable and implantable devices call for better integration with the human body. 3D printing of hydrogel ionotronics, presenting a promising strategy for constructing soft and stretchable devices, could effectively address this demand. Existing approaches for developing 3D-printable ionotronic materials face challenges in balancing ink printability, printed structural mechanical robustness, and ionotronic performances. The lack of compatibility in fabricating ionotronic devices with multiple functional ionic elements further impedes their advancement. This thesis aims to address the aforementioned challenges by focusing on approaches in materials design and fabrication techniques. To this end, the goal of this thesis is to develop novel hydrogel material systems and innovative 3D printing methods for ionotronics by leveraging the physical and mechanical properties of different forms of hydrogels, various mechanical toughening mechanisms, and ionic functionalities of diverse ionic species. The specific aims of this thesis are listed as follows.

Specific aim 1: Developing a polyelectrolyte complex hydrogel that is 3D-printable and can undergo extreme mechanical enhancement by phase transition.

In the first aim, emphasis would be placed on achieving simultaneous hydrogel printability and mechanical robustness. A family of PAAc/Chit hydrogel with different polymer concentrations and polymer ratios was to be synthesized. The phase transitioning behavior in response to different conditions (kinetics, environment pH, coupling reagent) would be studied, and evaluations were to be conducted encompassing the physical (volume ratio) and mechanical performances (stretchability, elastic modulus, tensile strength, fracture toughness, and adhesion). Adhesion performances to biological and non-biological substrates were to be investigated. The assessment of 3D printing performances would be carried out regarding printing time window, ink rheological characteristics, and shape fidelity. To be used as ionotronic materials, the ionic conductivities and electromechanical coupling were to be measured and demonstrations of wearable strain sensor, tissue mimetics, patterned adhesion, and four-dimensional (4D) printing were to be presented. The outcomes of this aim would yield an optimized PAAc/hydrogel formulation and synthesis procedure and to suggest its adequacy for application in ionotronics.

Specific aim 2: Developing the 3D IMP strategy that is capable of fabricating stretchable and tough hydrogels with complex structures and diverse ionic functions.

The second aim of this thesis would center on resolving the research challenge related to limited ionic functionalities while ensuring the ink printability and structural mechanical robustness. Agarose microgels, incorporating three different ionic species (NaCl, polyanion, polycation), along with precursors of a second AAm network, would be synthesized and printed. Evaluation of 3D printing quality for each type of ink was to be conducted, considering rheological behavior, shape fidelity, and printing resolutions. The electrical performance was to be assessed based on an ionic junction comprising two ionic components. Cyclic voltammetry and electrochemical impedance microscopy would be conducted on ionic junctions under various conditions (polyelectrolyte concentration, polyelectrolyte species, heterogeneity, desalination, and size) to appraise the electrical performances and investigate the electrochemical mechanisms. Subsequent characterizations would focus on the mechanical robustness (stretchability, fracture toughness, inter-component adhesion) and degradation behavior of such devices. The outcomes of this aim include a family of optimized DN PAAm/Agar microgel materials, a 3D IMP strategy with validated printing, structural, and electrical performance, as well as a fundamental understanding of the electrochemical process underlying hydrogel ionic junctions.

Specific aim 3: Validating the efficacy and applicability of the 3D IMP method in constructing integrated ionotronic devices with multiple ionic components.

In the last aim, the material system and fabrication technique established in aim 2 would be validated by an array of ionotronic devices. 3D IMP would be implemented to construct ionic-active components in all devices, incorporating all three ionic species. First, an ionic bipolar-junction transistor in p-n-p configuration was planned to be fabricated with p- and n-type microgels. The evaluations would include performances such as threshold voltage, current modulation behaviors under sweeping or step inputs, and on-off ratio. Subsequently, with the same microgel inks, an ionic full-wave rectifier was to be printed. The assessment would encompass current rectification performances under different input waveforms (sinusoidal or square wave) and various signal frequencies (0.01, 0.1, 1 Hz). Finally, to confirm the efficacy of printing of ionic conductors (microgels comprise NaCl), an ionic touchpad was to be constructed. Printed ionic conductors were intended to function as the current collector for each triboelectric nanogenerator sensing pixel. Voltage signals corresponding to single- and multi-point touches were planned to be assessed. Completion of this aim was expected to yield three ionotronic devices, accompanied by insights into the applicability of the 3D IMP strategy to fabricate multi-component ionotronics.

CHAPTER 2

Materials and Methods

This chapter describes the numerical and experimental methods as well as materials used throughout the thesis. The content in this chapter is categorized into six sections. First, detailed procedures in material synthesis including the hydrogels and printable inks, along with 3D printing methods are elaborated. The following sections describe the material characterizations conducted in this thesis, specifying physical and structural, mechanical, as well as electrical characterizations. Finally, pertinent details regarding the fabrication and characterization of the ionotronic devices are presented, followed by explanations of the statistical analysis used.

2.1 Material Synthesis and Fabrication

Two types of hydrogels were synthesized for the study of the material components, fabrication method, and realization of various hydrogel ionotronic devices. First, the PAAc/Chit hydrogels were synthesized to investigate the use of polyelectrolyte complex and phase-transitioning strategy in 3D printing of tough and ionically conductive materials. Then, DN agarose/polyacrylamide (Agar/PAAm) hydrogels with positively or negatively charged polyelectrolytes were prepared by either mold casting or 3D printing method to establish the 3D IMP method in fabricating ionotronic devices. The materials used and the synthesis steps are detailed in this section.

2.1.1 PAAc/Chit polyelectrolyte complex hydrogels

Synthesis of PAAc/Chit hydrogels. PAAc (Mw ~1250000, 306215) was purchased from Sigma-Aldrich. The PAAc solutions were prepared by dissolving PAAc powders in deionized (DI) water at concentrations of 15%, 11.25%, 7.5%, and 3.75% (w/v). To obtain uniform solutions were mixed with a vortex mixer (VWR) for 10 minutes, a rotary mixer (Fisher Scientific) for 24 hours, and heated at 40℃ in an oven for 12 hours. Chit (DDA: 95%, medium and high molecular weight, water soluble) was purchased from Xi'an Lyphar Biotech (Shanxi, China). Similarly, the Chit solutions were prepared by dissolving Chit powders in DI water at concentrations of 20%, 15%, 10%, and 5% (w/v) by vortex for 10 minutes and rotary mixers for 24 hours. The chemical structures of the two constituents, PAAc and Chit, are shown in Figure 2.1.

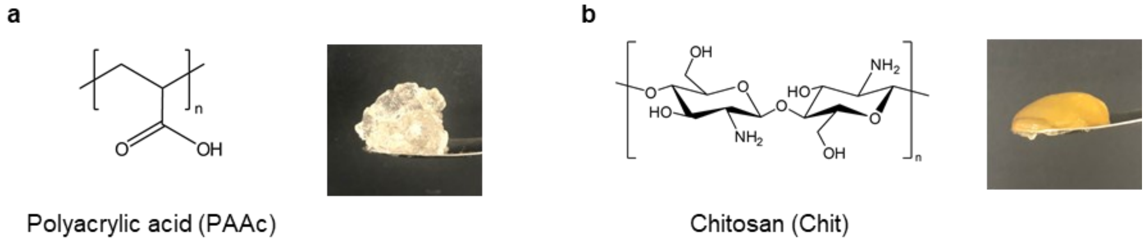

Figure 2.1. Chemical structures and digital images of the key constituents for the PAAc/Chit polyelectrolyte complex hydrogels. (a) PAAc and (b) Chit.

The phase transitioning PAAc/Chit polyelectrolyte complex hydrogels contain PAAc and Chit at weight ratio of 3:1. The PAAc/Chit hydrogels with total polymer contents of 12% (w/v) were obtained by mixing 11.25% (w/v) PAAc solution with 15% (w/v) Chit solution at 4:1 volume ratio. As a result, the final concentration of PAAc was 9% (w/v) and Chit was 3% (w/v). Specifically, the PAAc and Chit solutions were loaded into two separate syringes, centrifuged (Eppendorf, Centrifuge 5810R) at 2000 rpm for 15 minutes, and quickly syringe-mixed for 1 minute to yield a uniform solution. The solution was then poured into a glass mold covered with polytetrafluoroethylene (PTFE) tape (McMaster Carr, 6305A22). Carbodiimide coupling reagents were optionally introduced into the material system during 3D printing, adhesion tests, electrical characterizations, and demonstration of applications. N-(3-Dimethylaminopropyl)-N′-ethylcarbodiimide hydrochloride (EDC, Sigma-Aldrich, 03450) and N-Hydroxysuccinimide (NHS, Sigma-Aldrich, 56480) were both dissolved in chitosan solutions at concentration of 10 mg mL^{-1} before mixing with PAAc. For the total polymer concentration study, PAAc/Chit hydrogels of 16%, 8%, and 4% (w/v) were obtained by mixing 15%, 7.5%, 3.75% (w/v) PAAc solutions with 20%, 10%, 5% (w/v) Chit solutions at volume ratio of 4:1, respectively. For the study of polymer ratio, a similar procedure was implemented, except PAAc and Chit solutions were prepared at different concentrations and mixed at different volume ratios. Specifically, to obtain PAAc/Chit hydrogels with PAAc to Chit weight ratio of 6:1, 9:2, 9:4, and 3:2, 18% (w/v) PAAc solutions and 3%, 4%, 8%, 12% (w/v) Chit solutions were mixed at 1:1 volume ratio, respectively, before pouring into the mold. The detailed ingredients for each formulation are listed in Table 2.1.

To trigger phase transition, as-prepared PAAc/Chit hydrogels were carefully removed from the molds and immersed in baths of 1 L DI water for 48 hours. The baths were subjected to mechanical stirring at 60 rpm. For mechanism study, as-prepared hydrogels were immersed in baths of different pH levels (1, 2, 3, 5, 7, 9, 11, 13). The baths were prepared by adding specific amount of either hydrochloric acid (HCl, Fisher Scientific, FLSA481) or sodium hydroxide (NaOH, ACP Chemicals Inc., S3698) to DI water, and the reservoir pH were validated with a pH meter (Mettler Toledo, FiveEasy). For phase transition kinetics study, hydrogels were removed from DI water baths at predetermined time intervals (1, 3, 6, 12, 24, 48 hours).

Table 2.1. Formula of the PAAc/Chit hydrogels.

Total polymer content	PAAc: Chitosan	PAAc		Chitosan	
		Volume	Concentration	Volume	Concentration
16%	**3:1**	4	15%	1	20%
12%	**3:1**	4	11.25%	1	15%
8%	**3:1**	4	7.5%	1	10%
4%	**3:1**	4	3.75%	1	5%
10.5%	**6:1**	1	18%	1	3%
11%	**9:2**	1	18%	1	4%
13%	**9:4**	1	18%	1	8%
15%	**3:2**	1	18%	1	12%

3D printing of PAAc/Chit polyelectrolyte hydrogels. The PAAc/Chit hydrogel with 9% (w/v) PAAc and 3% (w/v) Chit was chosen to be used in most printing tasks and referred to as PAAc9/Chit3. Freshly mixed PAAc and Chit solution was first loaded into cartridges. To remove trapped air, the cartridges were sealed and centrifuged at 2000 rpm for 1 min. All printing was performed on a commercial 3D bioprinter (BioX2, Cellink) under pneumatic control. 3D models were generated using Solidworks (Dassault Systems) and exported as .stl files. G-codes were generated by Heartware slicer (Cellink) with 603 μm layer height, 3 perimeters, 3 top and bottom layers, 100% infill, and concentric infill patterns. 20G blunt needle nozzles (603 μm inner diameter, 12.7 mm needle length, Cellink) and glass petri dishes (Cellink) were used for all printing tasks. The printing parameters were set at pressure of 80 kPa for PAAc9/Chit3 and 40 kPa for

PAAc6/Chit1, and 7 mm s^{-1} writing speed. Printed structures were stabilized at room temperature and 50% relative humidity for 24 hours and then immersed in 200 mL of DI water for 48 hours to phase transition. For patterned adhesion, printing of morphing structures, and fluidic channel demonstrations, polyacrylamide/alginate (PAAm/Alg) hydrogels or fresh porcine skins were used. They function as substrates during printing and provide pH-changing environment for printed structures to go through phase transition.

2.1.2 Agar/PAAm DN hydrogels

Synthesis of cast DN Agar/PAAm hydrogels and devices. The two-step synthesis protocol was adopted here. First, single-network (SN) agarose hydrogels with polyelectrolytes were synthesized. Biopolymer polyelectrolytes chondroitin sulfate sodium (CS, purity ≥ 98%) and quaternary chitosan ammonium (QC, DDA: 99%) powders were purchased from Xi'an Lyphar Biotech (Shanxi, China). Polyelectrolyte solutions were prepared by dissolving CS and QC powders in DI water at 20 % and 10 % (w/w) concentration, respectively. The solutions were mixed by a vortex mixer (VWR) for 10 minutes and a rotary mixer (Fisher Scientific) for 24 hours before use. For every 1 g p-type precursor, 20 mg agarose powder (low melting point, BioShop, AGA101) and 450 mg 20% (w/w) CS solution were added to 0.53 mL DI water. The mixture was heated at 90℃ under 500 rpm stirring for 30 minutes until uniform. For the n-type precursor, agarose powder was dissolved in DI water at 4% (w/w) at 90℃ under 500 rpm stirring, while the 10% (w/w) QC solution was heated at 70℃ for 30 minutes. Hot agarose and QC solutions were quickly syringe-mixed at 1:1 weight ratio until uniform. The prepared p-type and n-type hot mixtures were poured into glass molds and cooled at room temperature for 12 hours until complete gelation.

In the second step, 20% (w/v) acrylamide (AAm, Sigma-Aldrich, A9099) and 1% (w/v) poly(ethylene glycol) diacrylate (PEGDA Mn 250, Sigma-Aldrich, 475629) were first dissolved and stirred for 24 hours before use. 18.9% (w/v) 2-Hydroxy-4′-(2-hydroxyethoxy)-2-methylpropiophenone (I2959, Sigma-Aldrich, 410896) was dissolved in ethanol and covered with aluminum foil 1 hour before use. To prepare the gelling solution, 600 µL 1% PEGDA solution and 500 µL 18.9% I2959 solution were added to 15 mL 20% degassed AAm solution to obtain a gelling solution containing 18.6% (w/v) AAm, 0.0373% (w/v) PEGDA, and 0.588% (w/v) I2959. The SN agarose hydrogels were then immersed in the gelling solution for at least 24 hours in a dark environment for the components of the second polymer network to diffuse in. To form the second hydrogel network, each p-type and n-type hydrogel was clamped in a glass mold and subject to UV irradiation (OAI Instruments, 33 mWcm^{-2}, 365 nm) in an ice bath for 1 hour until complete gelation. Ionic junction devices were fabricated with the same procedure as bulk DN hydrogels, except two oppositely charged hydrogels were clamped together with 10% compression in a glass mold and subjected to 30 minutes UV irradiation each side.

Table 2.2. Formula of the Agar/PAAm hydrogels.

Agarose	P-type	N-type	PAAm gelling solution				
			AAm	I2959	crosslinker		other
2%	CS 15%	QC 7%	18.6%	0.588%	PEGDA	0.0373%	N/A
2%	CS 9%	QC 5%	18.6%	0.588%	PEGDA	0.0373%	N/A
2%	CS 3%	QC 3%	18.6%	0.588%	PEGDA	0.0373%	N/A
2%	PSS 7%	PDAC 5%	18.6%	0.588%	PEGDA	0.0373%	N/A
2%	CS 9%	QC 5%	18.6%	0.588%	MBAA	0.0192%	N/A
2%	N/A	N/A	18.6%	0.588%	PEGDA	0.0373%	NaCl 3M

For polyelectrolyte concentration study, 15%/7% and 3%/3% (w/w) CS/QC ionic junctions were prepared by similar methods, except different amounts of 20% (w/w) CS solution and 10% (w/w) QC solution were added to the mixture in the first step. For polyelectrolyte species study, 201.5 µL 30% (w/w) PSS solution (Mw~70000, 30 wt.%, Sigma-Aldrich, 527483) and 240.4 µL 20% (w/w) PDAC solution (Mw 400000–500000, 20 wt.%, Sigma-Aldrich, 409030) were added to every 1 g of precursor, respectively, before heating. The resulting SN hydrogels contained 7% (w/w) PSS and 5% (w/w) PDAC, respectively. For in-vitro degradation study, non-degradable DN hydrogels were synthesized by substituting PEGDA with 150 µL 2% (w/v) N,N′-methylenebis(acrylamide) (MBAA, Sigma-Aldrich, M7279) in the second step. Table 2.2 listed the detailed constituents for each formulation. For electrical performance study, desalinated samples were made by immersing each piece of SN hydrogel (1.8 mL) in DI water (1 L) for 7 hours before the second step. Washed samples were made by soaking each piece of DN hydrogel (1.8 mL) in 10 mL 30% (v/v) ethanol twice and 10 mL DI water thrice. The chemical structures of the key components in the material system are demonstrated in Figure 2.2.

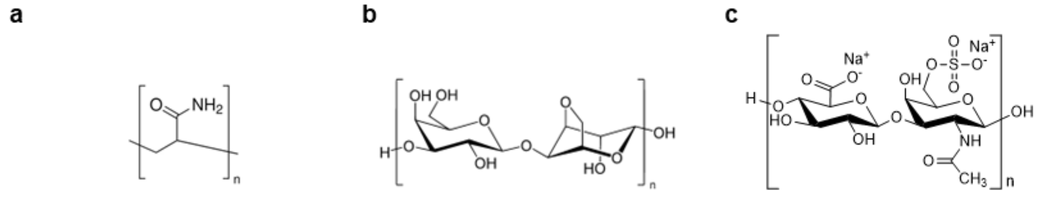

Polyacrylamide (PAAm)

Agarose (Agar)

Chondroitin sulfate sodium (CS)

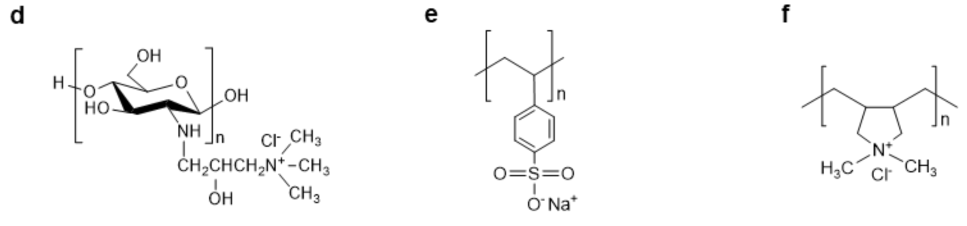

Quaternary chitosan (QC)

Poly(sodium 4-styrenesulfonate) (PSS)

Poly(diallyldimethylammonium chloride) (PDAC)

Figure 2.2. Chemical structures of the key ingredients for forming the ionic microgels. (a) Constituents for the DN hydrogel polymer matrix include polyacrylamide (PAAm) and (b) agarose (agar). (c) Biopolymer polyelectrolytes include negatively charged chondroitin sulfate sodium (CS) and (d) positively charged quaternary chitosan (QC). (e) Synthesized polyelectrolytes include negatively charged poly(sodium 4-styrenesulfonate) (PSS) and (f) positively charged poly(diallyldimethylammonium chloride) (PDAC).

Preparation of ionic microgels. The batch emulsion method was adopted to fabricate ionic microgels. P-type and n-type SN hydrogel precursors were prepared as described above. The synthesis process was illustrated in Figure 2.3, the hot aqueous mixture was drop-by-drop added to mineral oil solutions (light, BioShop, MIN333) containing 2% (w/w) Span80 (Sigma-Aldrich, S6760) that is heated at 90℃ under constant stirring. The water-in-oil emulsion was stirred at 1200 rpm while cooled to room temperature for complete gelation of agarose. The resulting microgels were centrifuged at 4000 rpm for 3 minutes (Eppendorf, Centrifuge 5810R), and the supernatant was discarded. To remove the mineral oil, 30 mL 30% (v/v) ethanol was added to 5 mL microgels, followed by vortex mixing for 1 minute. The mixture was centrifuged, and supernatant discarded. The process was repeated twice with ethanol (30%) and thrice with DI water. Clean p-type, n-type microgels were screened through cell strainer (pluriSelect, 300 μm) by vacuum filtration and resuspended in water for storage. To incorporate the second polymer network in the ink, SN microgels were resuspended in a gelling solution containing 18.6% (w/v) AAm, 0.0373% (w/v) PEGDA, and 0.588% (w/v) I2959 for 24 hours before use. For microgels containing sodium chloride (NaCl, ACP Chemicals Inc., S2830), 2% (w/w) agarose microgels without polyelectrolytes were suspended in the same gelling solution but with 3M NaCl added.

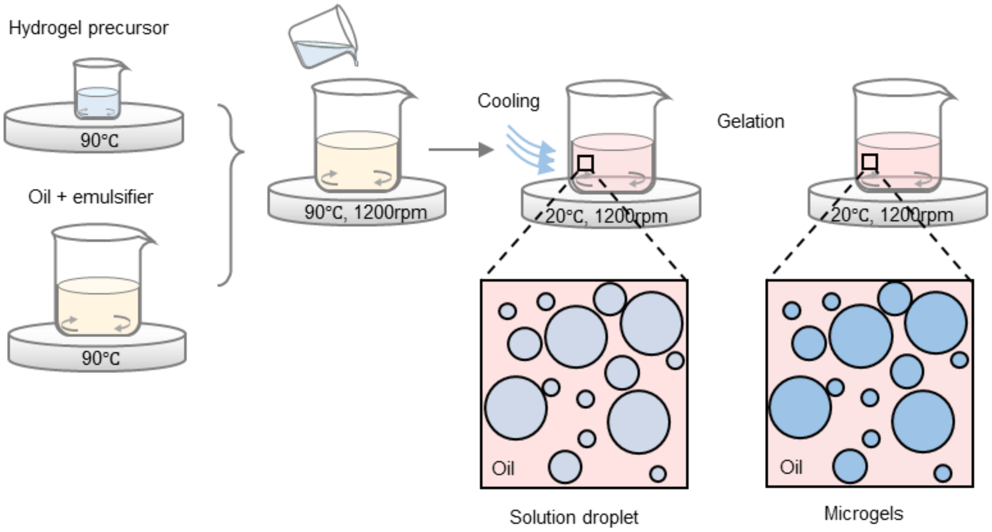

Figure 2.3. Synthesis of the agarose microgels by batch emulsion method.

3D ionic microgel printing. The preparation procedure for the microgel to become printable inks was illustrated in Figure 2.4, the microgel suspension was vacuum filtrated (particle retention: 5-10 µm, Fisherbrand) to yield jammed microgel ink. The jammed microgel ink was then loaded into cartridges. To remove trapped air, the cartridges were sealed and centrifuged at 2000 rpm for 1 min. The printing was performed on a commercial bioprinter (BioX2, Cellink) under pneumatic control. 3D models were generated using Solidworks (Dassault Systems) and exported as .stl files. G-code was generated by either the built-in slicer (HeartWare, Cellink) or PrusaSlicer (Prusa) with 410 µm layer height, 3 perimeters, 3 top and bottom layers, 100% infill, and concentric infill patterns. 22G conical nozzles (410 µm inner diameter, 32 mm nozzle length, Cellink) and glass petri dishes were used for all printing tasks. The printing parameters were set at pressure of 20 kPa for p-type ink, 8 kPa for n-type ink, and 15 kPa for NaCl ink, and all printing tasks were performed at 7 mm s^{-1} writing speed. Printed structures were crosslinked by exposure to UV irradiation (33 $mWcm^{-2}$, 365nm, OAI Instruments) under nitrogen (N_2) flow and 50% relative humidity for 30 minutes. For printing fidelity study, food colorings (Nasco, K00454) were added to p-type (red) and n-type (blue) inks after jamming before printing. For printing resolution study, line widths were measured against varying ink-write speed and printing pressure for different inks. Line widths were determined using ImageJ.

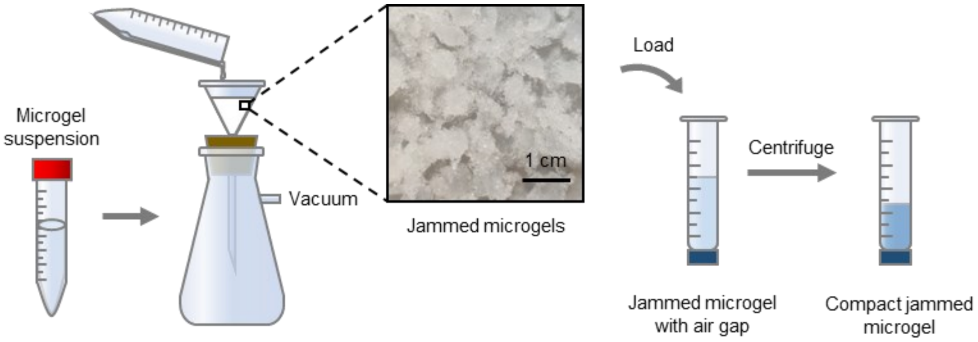

Figure 2.4. Preparation of the microgels inks for printing. The microgel suspension was vacuum filtrated and centrifuged to yield jammed microgel inks ready for printing.

2.2 Physical and Structural Characterizations

2.2.1 Swelling test

As-prepared PAAc/Chit hydrogels were cut into 50 mm × 20 mm × 1.5 mm strips. Each sample was immersed in 1 L DI water for 24 hours. Hydrogels after transition were then removed from the baths, and their length, width, and thickness were measured using a digital caliper. The volume of the hydrogels was calculated as the product of length, width, and thickness, while the volume ratio was determined as the post-treated volume over the initial volume x 100%.

2.2.2 Degradation

In vitro hydrolytic degradation study of the ionic junction was conducted using Dulbecco's phosphate-buffered saline (DPBS, Sigma-Aldrich, 56064C) with or without enzymes. Ionic junctions were punched from a large piece of printed ionic junction into cylindrical disks (D = 6.35 mm, T = 3 mm). Each sample was submerged in 15 mL DPBS at 37 °C under 10 rpm shaking with medium replaced daily. At each time interval, samples were removed from the medium, thoroughly washed with deionized water, and lyophilized. Dry weight was determined as the mass percentage ratio of lyophilized samples at each time interval to the original lyophilized sample. The enzymatic degradation medium was prepared right before use by adding 5 mg collagenase (≥20,000 U/mg, MP Biomedicals, 02100831-CF) and 5 mg lysozyme (type I, >125 U/mg, MP Biomedicals, 02195109-CF) in every 100 mL DPBS. In addition, 0.01% (w/v) sodium azide (Sigma-Aldrich, 71289-5G) was added into the medium to prevent the growth of microorganisms.

To study the electrical performances against degradation time, degradation was performed with similar methods, except each rectangular strip of printed ionic junction (L = 20 mm, W = 15 mm, T = 1.5 mm) was submerged in 50 mL of DI water and punched into cylindrical disks (D = 5.56 mm) for electrical measurements. The degradation circuit was printed with QC microgel ink and crosslinked under UV lamp. Each circuit was submerged in DPBS (70 mL) at 37 °C under 10 rpm shaking with medium replaced daily.

2.2.3 Microscope

All microscope images were obtained using Olympus CKX41 optical microscope. The size distribution of microgels were obtained by measuring the diameter of 780 microgels for each species via ImageJ.

2.3 Mechanical Characterizations

2.3.1 Rheological properties

All rheological characterizations were conducted on a torsional rheometer (TA Instruments, Discovery HR-2 rheometer) with a steel parallel plate (upper plate diameter: 20 mm) and 1000 μm gap at temperature of 25 °C. The Trios software (TA Instruments) was used to control the rheometer and for acquisition and analyzation of data. For each test, freshly prepared material was injected in the middle of the two parallel plates and completely filled the gap. After removing excess material, a solvent trap (TA Instruments) was used to avoid dehydration during measurements.

Strain rate dependent viscosity measurements were performed with logarithmic sweep of shear frequency (0.01 – 100 Hz) at 0.5% shear strain. The storage (G') and loss (G'') moduli and complex viscosity (η) were recorded. To characterize the shear yielding behavior, amplitude sweeps were conducted with logarithmic sweep of either shear strain (0.01%–500%) or shear stress (0.5 – 3000 Pa) at 1 Hz shear frequency. G', G'', and shear strain (γ), and shear stress were recorded. The shear yielding point for each sample was identified as the shear strain and stress at which G' and G'' equal. To determine the ability of materials to self-recover from liquid state to solid state, 3 consecutive cycles of alternating low (0.5%, 120s) and high (100%, 120s) shear strain at 1 Hz shear frequency were applied. For study of the crosslinking kinetics and printing time window for the PAAc/Chit hydrogels after the addition of EDC/NHS, isothermal time sweeps were performed at 0.5% shear strain and 1 Hz shear frequency, while the *G'* was recorded.

2.3.2 Tensile properties

Tensile testing was performed to determine the basic stress-strain behavior of materials and to extract mechanical properties such as elastic modulus, tensile strength, and stretchability. In this section, tensile testing was conducted on the PAAc/Chit polyelectrolyte complex hydrogels.

To prepare, samples were shaped into rectangular strips. PAAc/Chit hydrogels were cut into strips of length 30 mm, width 5 mm, and thickness 0.3 mm, and glued (Krazy Glue) to rigid polyethylene terephthalate (PET) clamps on both ends.

To measure the tensile properties, samples were pulled unidirectionally by a mechanical testing machine (Instron, model 5965, 10 N load cell, 2530-10N) at a displacement rate of 30 mm min^{-1} while force and displacement were recorded. The nominal stress was obtained by dividing the force by the original cross-sectional area. The nominal strain was obtained by dividing the change in length by the original length. The stretch (λ) was obtained by dividing the actual length by the original length.

2.3.3 Fracture toughness

Two methods are used to determine the fracture toughness of hydrogels. The pure shear test was used for determining the fracture toughness of DN Agar/PAAm ionic junction devices, while the trousers tear test was chosen to characterize the fracture toughness of the PAAc/Chit polyelectrolyte complex hydrogels.

Pure shear test. The fracture energy of assembled DN Agar/PAAm ionic junctions were measured with pure shear tests. Each sample was composed of two oppositely charged DN hydrogels sandwiched along the thickness direction, with width 60 mm, and total thickness 3 mm. Polymethyl methacrylate (PMMA) clamps were glued (Krazy Glue) to the samples. The distance between the two clamps was the sample length (L = 5 mm). A pair of notched and unnotched samples was used to obtain one data point. For notched samples, a notch of length 20 mm was introduced by a razor blade in the middle of the gauge section of the specimen. Samples were pulled unidirectionally by an Instron machine (model 5965, 1 kN load cell, 2580-1KN) at a strain rate of 2 min^{-1} while force (F) and displacement (δ) were recorded. The nominal stress (S) was obtained by dividing the force by the original cross-sectional area (A_0). The stretch (λ) was obtained by dividing the actual length (L) by the original length (L_0). Critical stretch (λ_C) was determined as the stretch at maximum stress for notched samples, denoting the event of crack running. Fracture energy (Γ) was calculated using the engineering stress–stretch ($S - \lambda$) curve from unnotched samples as: $\Gamma = H \int_1^{\lambda_C} S d\lambda$.

Trousers tear test. The fracture energy of the PAAc/Chit hydrogels were characterized using trouser tear test. Samples were cut into strips of length 20 mm, width 10 mm, and thickness (T) 0.3 mm. A notch of length 5 mm was introduced along length direction by a razor blade in the middle of the width direction. Rigid PET sheets were glued to each half of the notch (width direction) on opposite sides (thickness direction) of the sample. Samples were pulled unidirectionally by an Instron machine (model 5965, 10 N load cell, 2530-10N) at a displacement rate of 0.5 mm s^{-1} while force (F) and displacement (δ) were recorded. Since backings are attached to the arms of the hydrogels, the external energy input from the tensile testing machine was assumed to be all dissipated at the crack tip. As such, the force/width plateau denoted the equilibrium state and was used to calculate the fracture toughness. Fracture energy (Γ) was calculated by dividing two times the average force at plateau (F_{avg}) by the thickness of the specimen as: $\Gamma = 2F_{avg}/T$.

2.3.4 Adhesion energy measurement

Two methods are used to determine the adhesion energy. T-peeling test was used to determine the adhesion energy between different units of the ionic junctions. It is also used to obtain the adhesion performance of PAAc/Chit hydrogels to porcine skin and other hydrogels. The modified lap shear test was implemented to determine the adhesion energy of the PAAc/Chit polyelectrolyte complex hydrogels with porcine heart.

T-peeling test. Two pieces of oppositely charged DN hydrogels strips of length 80 mm, width (W) 15 mm, and thickness 1.5 mm were adhered with one end open, forming a bilayer with an edge crack of 5 mm. Similarly, the as-prepared PAAc/Chit hydrogels were shaped into strips of length 50 mm, width (W) 20 mm, and thickness 1.5 mm. Fresh porcine skins were purchased from local market, cut into strips, and fat tissues were removed. The as-prepared PAAc/Chit hydrogels were brought into contact with adherends (PAAm/Alg hydrogel or porcine skin) of same shape and stabilized for 24 hours to form adhesion. Rigid PET sheets were glued (Krazy Glue) to the back of the adherends to limit elongation and ensure all work done by the machine was dissipated by the crack tip. Free ends of the gels were pulled unidirectionally by an Instron machine (model 5965, 10 N load cell, 2530-10N) at a constant rate of 100 mm min^{-1} while force (F) and displacement (δ) were recorded. The adhesion energy (Γ_{adh}) was calculated by dividing two times the average force at plateau (F_{avg}) by the thickness of the specimen as: $\Gamma_{adh} = 2F_{avg}/W$.

Modified lap shear test. The PAAc/Chit polyelectrolyte mixtures with 10 mg mL^{-1} EDC/NHS were shaped into strips of length (L) 20 mm, width (W) 10 mm, and thickness 1 mm. Fresh porcine heart was purchased from the local market and cut into strips of same sizes. Rigid PET sheets were glued to the back of the samples. To form adhesion, as-prepared PAAc/Chit hydrogels were brought into contact with the tissues with an edge initial crack (C) of 5 mm. Free ends were pulled unidirectionally with an Instron machine (model 5965, 10 N load cell, 2530-10N) at a constant rate of 0.5 mm s^{-1} while force (F) and displacement (δ) were recorded. The adhesion energy (Γ_{adh}) was calculated as the area under the force displacement curves until critical displacement (δ_C) that corresponds to the maximum force and divided by the adhesion area: $\Gamma_{adh} = \frac{\int_0^{\delta_C} F d\delta}{(L-C)W}$.

2.4 Electrical Characterizations

In this thesis, three types of electrical characterizations were conducted on the hydrogels, including electrical conductivity of the ionic material, electromechanical coupling, and electrochemical characterizations.

2.4.1 Electrical conductivity

Two methods were used to measure the electrical conductivities of the ionic hydrogels. In either method, electrical conductivity (σ) was calculated from the measured electrical resistance (R) and the geometrical size of the sample including length (L) and cross-sectional area (A), according to the following formula: $\sigma = \frac{L}{R(A)}$.

By default, the resistances of hydrogels were measured as the real part of the electrical impedance using an LCR meter at 1 kHz alternating-current (ac) frequency. The as-prepared PAAc/Chit hydrogels were cut into rectangular strips of length (L) of 30 mm, width (W) of 20 mm, and thickness (T) of 1.5 mm, while the phase-transitioned (PT) ones had length (L) 15 mm, width (W) 10 mm, and thickness (T) 1 mm. Agar/PAAm ionic conductors were printed with ionic microgels into strips of length (L) 20 mm, width (W) 5 mm, and thickness (T) 1.5 mm. The cross-sectional area of the samples was calculated as $A = WT$. Samples were attached with carbon paper electrodes (Sigracet 22 BB, SGL Carbon, Germany) on both sides and connected to the LCR meter with alligator clips.

Electrical resistances of the Agar/PAAm p-type and n-type gels were obtained as the bulk resistance (R_B) from fittings of the ac-impedance spectroscopy data. Samples were punched in cylindrical slabs of diameter (D) 5.56 mm and length (L) 3 mm. The cross-sectional area of the samples was calculated as $A = 0.25D^2$. Samples were sandwiched between two carbon electrodes and encapsulated in PDMS spacers and connected to a potentiostat (VersaSTAT 3, AMETEK Inc.).

2.4.2 Electromechanical characterizations

Electrical resistance measurements were performed during tensile testing to characterize the electromechanical coupling of the polymeric electronic materials. Ionic conductors were printed into strips of length (L) 20 mm, width 5 mm, and thickness 1.5 mm, and connected with carbon paper electrodes (Sigracet 22 BB, SGL Carbon, Germany) on both sides. The specimens were stretched using an Instron machine (model 5965, 10 N load cell, 2530-10N) at a displacement rate of 50 mm min^{-1}, while a LCR meter (U1733C, Keysight Technologies) measured the electrical resistance (R) at 1 kHz ac frequency and 1 Hz sampling rate. The stretch (λ) was obtained by dividing the actual length (L) by the original length (L_0). The linearity was obtained as the R^2 value of the fitted curve. The GF was calculated as the ratio of the change in output electrical resistance ($\Delta R/R_0$) to the change in input, either stretch value ($\Delta\lambda$) or bending angle of fingers (Δa), as the following: $GF = \frac{\Delta R/R_0}{\Delta\lambda}$ or $GF = \frac{\Delta R/R_0}{\Delta a}$.

2.4.3 Electrochemical characterizations

Unless stated otherwise, DN hydrogels with various polyelectrolytes were punched from a cast or printed bulk gel into cylindrical disks of diameter (*D*) 5.56 mm and height (*L*) 1.5 mm, where cross-sectional area (*A*) was calculated as $A = 0.25D^2$. Samples were fabricated by assembling gels in PDMS (Sylgard 184, Dow Corning) spacers and sandwiching them between two carbon paper electrodes (Sigracet 22 BB, SGL Carbon, Germany). Linear sweep voltammetry was performed using a potentiostat (VersaSTAT 4, AMETEK Inc.) with two-electrode setup, where the working electrode was connected to the positive terminal of the devices while the counter and reference electrode were connected to the negative terminal. Each sample was subjected to -6V reverse bias for 2 min for steady state distribution of counterions followed by a voltage sweep from -6V to 6V at 50 mVs^{-1} sweep scan rate while current (*I*) through the ionic junctions were measured. Current densities (*J*) were obtained by dividing the current with cross-sectional area (*A*) of the ionic junction as $J = I/A$. Rectification ratios were calculated as the current density ratio at +5 V to that of -5 V. AC-impedance spectra were measured using VersaSTAT 3 potentiostat (AMETEK Inc.) under two-electrode setup over a frequency range of 1 MHz to 0.1 Hz and an ac amplitude of 40 mV. ZView2 software (Scribner Associates) was used to fit the impedance data. All fitting processes resulted in chi-squared values less than 0.01.

2.5 Devices Fabrication and Characterizations

2.5.1 Ionic bipolar junction transistors

The ionic transistors were fabricated with p-type and n-type PAAm/Agar hydrogels. Two pieces of square-shaped p-type gels (5 mm x 5 mm x 1 mm) were 3D-printed with microgel inks, 2 mm apart, on top of a piece of rectangular-shaped n-type gel (12 mm x 5 mm x 1 mm). After curing under UV irradiation in N_2 environment for 30 minutes, the device was assembled with a PLA spacer and three carbon paper electrodes. Linear sweep voltammetry and cyclic voltammetry were performed using a potentiostat (Interface 1010E, GAMRY). The threshold voltages were determined by applying V_{EC} = 6 V and sweeping the V_{EB} from -1 V to 5 V at 50 mVs^{-1} scan rate. On/off performance was characterized by applying constant V_{CE} = -1 V and alternating V_{EB} between 5 V and 0 V. The performance of the ionic transistor was assessed by measuring the I_C, applying constant V_{EB} of -1 V to 6 V, and either sweeping V_{CE} from -6 V to 0 V at 50 mVs^{-1}, or imposing stepwise alternating voltage of -5 V and -1 V at 0.01 Hz. Root-mean-square (RMS) of I_C at on state to off state from six successive cycles were calculated as the on/off ratio.

2.5.2 Ionic full-wave rectifier.

The ionic full-wave rectifier was printed on glass substrates with patterned carbon paper electrodes. The glass substrates were treated with 5-min air plasma before printing. Four ionic diodes in a particular configuration were printed on freshly treated substrates to construct the full-wave rectifier. The structure was designed on SolidWorks (Dassault Systems) and G-code was generated by PrusaSlicer (Prusa). To characterize the rectifier, we generated alternating input and measured output signal using a set of data acquisition systems (NI 9263, NI9215, National Instruments) controlled by LabVIEW (National Instruments).

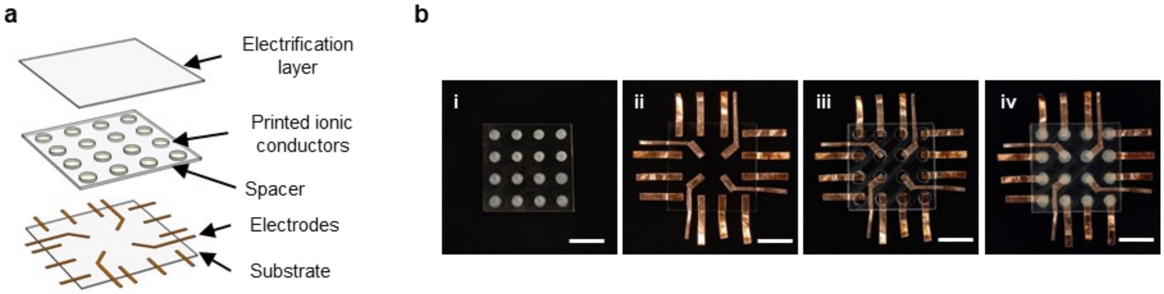

Figure 2.5. Structure of the ionic touchpad. (a) Schematic illustration of the ionic touchpad in exploded view. (b) Digital images of the structure and assembly process of the ionic touchpad. (i) Ionic hydrogels printed on a thin PDMS layer. (ii) Conductive copper tapes adhered to a thin PDMS layer. (iii) A PDMS spacer adhered to the PDMS substrate with electrodes. (iv) Assembly of the ionic hydrogels sub-assembly to the copper electrode sub-assembly to finish the build of the ionic touchpad. Scale bar 2 cm.

2.5.3 Ionic touchpad

The ionic touchpad was first fabricated by 3D printing of ionic microgels containing NaCl on PDMS (Sylgard 184, Dow Corning) substrates. Adhesion between the granular hydrogel and the elastomer was achieved following a previous protocol[100,101,128]. The elastomer substrates were first cleaned with ethanol and dried under N_2 flow. Then, the substrates were treated with 5-min air plasma, submerged in benzophenone (10 wt.% in ethanol) for 5 minutes, rinsed with ethanol, and dried under N_2 flow. A matrix of 4-by-4 cylindrical ionic hydrogels (D = 5 mm, H = 0.8 mm) were 3D-printed on freshly treated substrates with 1 cm center distances, followed by UV crosslinking in N_2 environment for 30 minutes. Next, we treated another thin piece of PDMS (0.4 mm) with 5-min air plasma then patterned copper tapes on it. Lastly, the ionic conductor sub-assembly, a PDMS spacer, and the electrode sub-assembly were assembled. The structure and assembly process were illustrated in Figure 2.5. Each individual sensor was connected to a 100 MΩ resistor, and the voltages across the resistors were measured as the output signals. Signals were captured by a data acquisition (DAQ) system (NI 9205, National Instruments) at 1 kHz under differential mode, and the DAQ was interfaced via LabVIEW (National Instruments). Figure 2.6 presents the connection diagram of the touchpad to the DAQ system. Signals from each pixel were first normalized with the mean of its corresponding peaks obtained during calibration. Then, filtered voltage signals were plotted on 3D bar plots as visual representations.

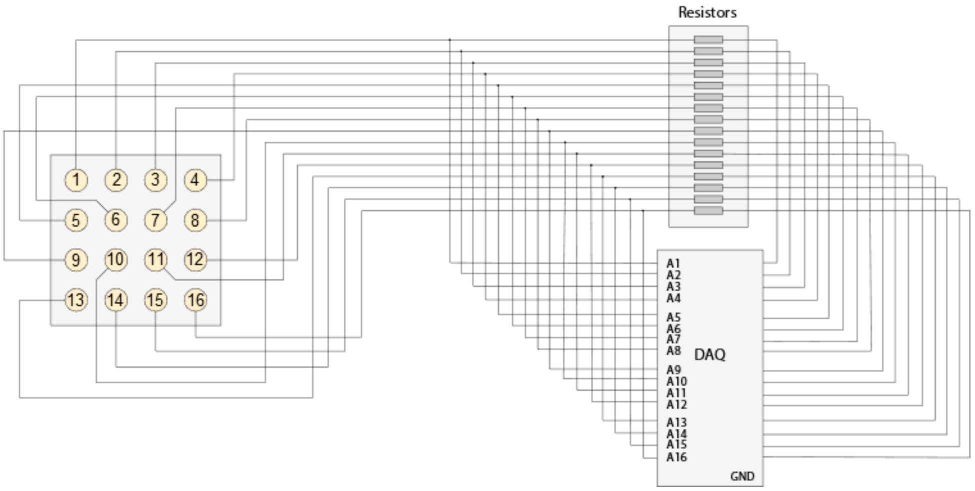

Figure 2.6. Schematic representation of the readout circuit for the ionic touchpad. Each pixel was connected to a resistor and the voltage across it was measured as the output signal. The signals are collected by a DAQ system that measures voltages in differential mode.

2.6 Statistical Analysis

All data are preprocessed by eliminating the maximum and minimum samples as outliers if any. Data are normalized with the corresponding mean value obtained during pre-measurement calibration. All quantitative analysis results were obtained from at least three valid samples. Data was expressed as the mean ± standard error of the mean. Unpaired Student’s t-test was used to calculate the p values. Different asterisks (*: $p < 0.05$, **: $p < 0.01$ and ***: $p < 0.001$) were considered statistically significant. GraphPad Prism software was used for statistical analysis.

CHAPTER 3

3D Printing of Polyelectrolyte Complex Hydrogels

Extrusion 3D printing of hydrogels demands inks with proper viscosity and shear-thinning behaviors, while for ionotronic devices, attributes like high stretchability, strength, and toughness are crucial for reliability and durability. When printing hydrogel-based ionotronic devices, one often faces the trade-off between the printability of hydrogel precursors and the mechanical properties of the resulting devices. To address this trade-off, this chapter introduces 3D-printable and ionically conductive PAAc/Chit polyelectrolyte complex hydrogels, featuring a unique phase-transitioning mechanism for mechanical enhancement post-printing. The bioinspired material system design is first presented, and the phase transitioning effect is revealed. The toughening mechanism is deciphered through a comprehensive characterization and analysis of mechanical performances, considering factors such as polymer ratio, total polymer concentration, kinetics, triggering pH, and coupling reagents. Adhesion performances to diverse substrates, including hydrogels and biological tissues are discussed, accompanied by an examination of adhesion mechanisms. The subsequent section covers the characterization of electrical properties, including conductivities and electrochemical coupling effects. The study then delves into 3D printing quality, addressing the printing time window and printability for hydrogels with various concentrations, along with exploring diverse phase transition scenarios during printing. The chapter concludes with demonstrations of the potential applications of the PAAc/Chit hydrogels for strain sensors, tissue mimetics, patterned adhesion, and morphing structures.

3.1 Design of the PAA/Chit polyelectrolyte complex hydrogel

In nature, sandcastle worms (*Phragmatopoma californica*) build intricate underwater hives using a unique hydrogel comprising of condensed and oppositely charged polyelectrolytic components[167]. As illustrated in Figure 3.1a, the natural two-part hydrogel contains oppositely charged proteins, with polycations Pc1,2,4,5 enriched in lysine, histidine, glycine, and tyrosine residues, and polyanion Pc3 consists of phosphoserine[168]. They can be secreted and solidified upon exposure to sea water of higher pH[169,170]. Inspired by the natural protein-based hydrogel produced by sandcastle worms, a printable tough adhesive hydrogel was designed based on electrostatically condensed, oppositely charged polyelectrolyte complex coacervates. Ultra-high molecular weight (⩾ 1250 kDa) PAAc polymer and water-soluble Chit polymer were used as the polymer backbone of the hydrogel. These two polymers are selected due to the charges they carry on their polymer chains (negatively charged PAAc, positively charged Chit), their responsiveness to pH change, and their well-studied properties. The pristine coacervates possess high ionic strength and behave as an injectable and printable fluid to be printed into defined structures. By ion exchange with the surrounding, it can undergo triggered condensation and phase transition into a tough matrix. The presence of hydrogen bonds at the interface and robust matrices enhances adhesion to a variety of substrates. (Figure 3.1b).

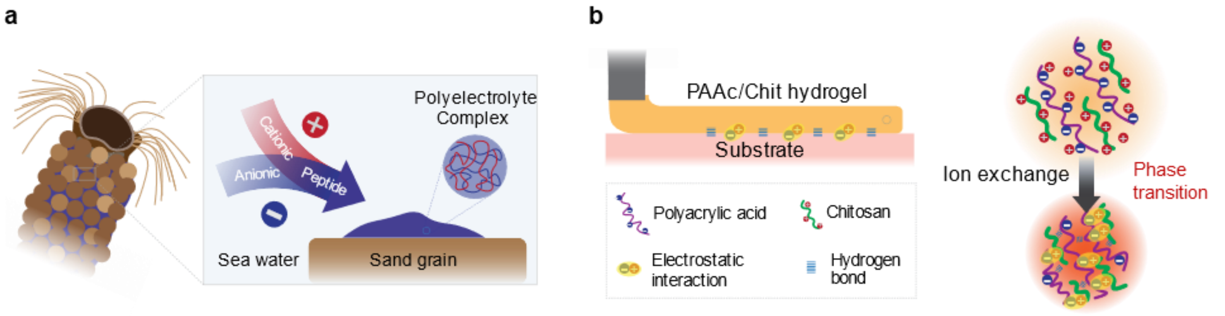

Figure 3.1. Schematic illustration of the bioinspired design of PAAc/chit polyelectrolyte complex hydrogels. (a) Sandcastle worms produce polycation and polyanion that can form polyelectrolyte complex. The polyelectrolyte complex is able to adhere to sand grains and build desirable structures when contacting sea water. (b) The material design of the PAAc/Chit polyelectrolyte complex hydrogel follows a similar mechanism. Biopolymer PAAc (polyanion) and Chit (polycation) form polyelectrolyte complex that is injectable and printable. The polyelectrolyte complex can go through phase transition after ion exchange and exhibit substantial mechanical enhancement effect. Adhesion to various substrates is achieved by the abundant hydrogen bonds.

The designed material system possesses three main advantages. First, the mixture of the oppositely charged polymer solutions yield a highly viscous but shear-thinning hydrogel, rendering it intrinsically printable, without the inclusion of rheological modifiers. The PT PAAc/Chit hydrogels feature a condensed polymer network. As depicted in Figure 3.2, the apparent macroscopic observations include the volumetric shrinkage and transparent-to-opaque appearance. By design, the ion exchange process provokes electrostatic interactions, hydrogen bonding, and topological entanglements between the polymer chains, resulting in drastically enhanced mechanical properties for the printed structures. Therefore, introducing a triggered mechanical enhancement mechanism offers a practical solution to concurrently achieve hydrogel printability and matrix toughness.

The use of both macromolecule crosslinkers (PAAc and Chit) bypasses the use of often cytotoxic monomer and crosslinker necessary to form stretchable networks[106,111,171,172]. A myriad of supramolecular interactions enriched by pH-induced phase transition provide strong physical bonds which dissipate energy under deformation. When interacted with biological tissues, or other hydrogels, strong interfacial physical and covalent bonds form. Together with the tough hydrogel matrix, robust interfacial adhesion can be achieved.

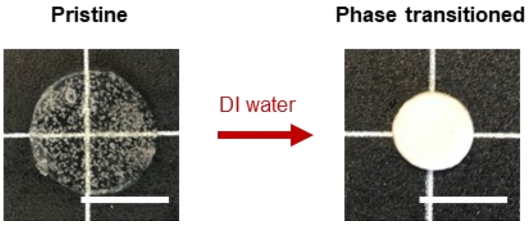

Figure 3.2. Digital image of the PAAc/Chit hydrogel which undergoes phase transition after submerging in DI water. Scale bar, 1 cm.

Another attribute of this system is ionic conductivity due to the mobile counterions of the polyelectrolytes PAAc and Chit. The polyelectrolytes in aqueous state dissociate into charged ionized groups in the polymer backbone and counterions in the water of the bulk hydrogel. The mobile counterions carry charges and their transportation in water that is contained in the polymer network conduct electricity. The intrinsic ionic conductivity, the decoupled printability and mechanical performances, and the excellent adhesion promises the PAAc/Chit hydrogel to be used as a suitable material in printable ionotronics.

3.2 Phase Transition and Mechanical Properties

3.2.1 Mechanical enhancement

The PT PAAc/Chit hydrogel presented markedly enhanced mechanical properties. To quantify and compare the mechanical performances of the hydrogels pre- and post- phase transition, pure shear tests were conducted.

As shown in Figure 3.3a, unnotched samples were stretched uniaxially on a tensile testing machine, with sample width much greater than the length. Both materials could elongate to more than two times their original length, evincing the abundance of hydrogen bonds in the material system. From the representative stress-strain characteristics presented in Figure 3.3b, while the as-prepared hydrogels could only be stretched to 4 times their original length until rupture, the PT hydrogels exhibited a stretch limit of 9. The condensed polymer network after phase transition resulted in material stiffening and strengthening. Consequently, significant improvements were observed in the calculated mechanical performances. This is evinced by a 50-fold increase (from 4.6 to 230 kPa) in elastic modulus, and 16-fold increase (from 12 to 206 Pa) in tensile strength, compared to the as-prepared PAAc/Chit hydrogels (Figure 3.3c-d).

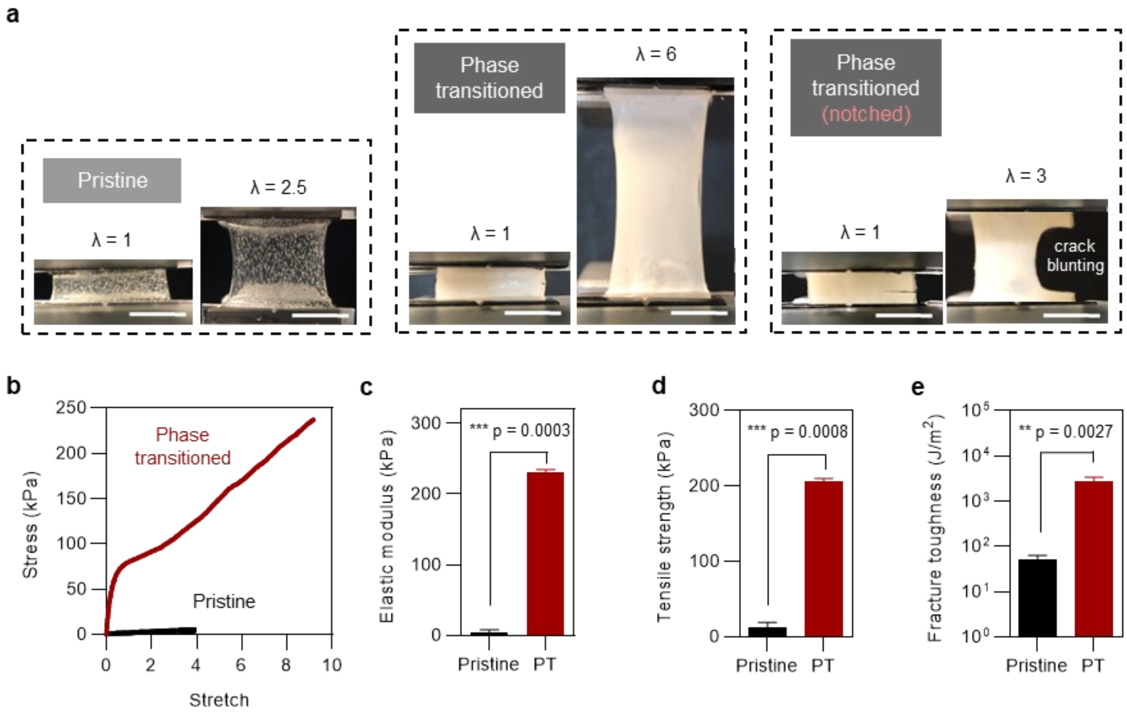

Figure 3.3. Mechanical enhancement of the PAAc/Chit hydrogel. (a) Digital images of the PAAc/Chit hydrogels in pristine or PT state, with a notched sample showing crack blunting behavior. Scale bar, 1 cm. (b) Representative stress-stretch curve of the unnotched samples, (c) corresponding elastic modulus, (d) tensile strength, (e) and fracture toughness obtained from pure shear tests. Scatter plots are presented from

representative data. Data are expressed as the mean ± SD from n = 3 samples. Statistical significance is analyzed from Student's t-test (**: P<0.01, ***: P<0.001).

To characterize the fracture toughness and visualize the crack growth mode, an edge notch in the middle of the probing region is introduced to the samples. The PT PAAc/Chit hydrogel displayed remarkable crack resistance. During stretching, the crack blunted dramatically instead of running across the sample. This could effectively deconcentrate the stress at the crack tip, allowing the intact region of the sample to continue dissipate energy despite the crack, resulting in high toughness. With the obtained critical stretch value, the fracture toughness was calculated and presented in Figure 3.3e. The fracture toughness elevated from 53 to 2679 J m^{-2}, demonstrating a 51-fold enhancement. The energy dissipation effect was also proven during uniaxial tensile loading-unloading tests within small strains (Figure 3.4). While the pristine hydrogel showed negligible hysteresis, the PT counterpart displayed clearly diverged loading and unloading stress-strain paths, indicating hysteresis loss.

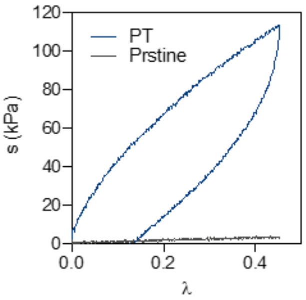

Figure 3.4. Mechanical performances of PAAc/Chit hydrogels during loading-unloading tests. Representative stress-strain curve for pristine and PT PAAc/Chit hydrogels during tensile loading-unloading tests within small strain.

3.2.2 Polymer ratio

The phase transition behavior depends on the interplay of PAAc and Chit in the polyelectrolyte complex. PAA hydrogel is highly hydrophilic and hygroscopic, as it can absorb a large amount of water and swell. Chit can be dissolved in acidic solutions but forms a hydrogel when pH is elevated. However, neither PAAc nor Chit SN hydrogel possess high toughness. It was discovered that within a certain range of polymer ratios, the PAAc and Chit mixture could undergo drastic condensation and phase transition into tough hydrogels when immersed underwater or in saline solution, and when in contact with biological tissue surfaces. However, other polymer ratios would result in imbalanced charges and yield significant swelling and brittle matrix with poor mechanical properties.

To investigate the effect of polymer ratio to the physical and mechanical properties of the PAAc/Chit hydrogels, the ratio of PAAc–Chit was varied while keeping the PAAc concentration constant. Fracture toughness and volume ratio were measured as quantitative criteria. Different weight ratios of PAAc and Chit were mixed thoroughly to yield an array of PAAc/Chit hydrogels. The hydrogels were immersed in DI water for complete transition, either contraction or swelling. Volume ratio was defined as the volume of the PT hydrogels to that of the as-prepared ones. The fracture toughness was measured by trouser tear tests (Figure 3.5a).

Representative force/thickness–displacement curves obtained from trouser tear test are presented in Figure 3.5b. Tearing of the PAAc/Chit hydrogels resulted in an initial increase in the measured force, followed by a plateau region, and eventually a catastrophic drop. The fracture energy results were shown in Figure 3.5c. When the Chit concentration is low, the hydrogel was brittle and transparent, because of extensive swelling in DI water and the absence of a phase transition. As the Chit: PAAc ratio increased, the fracture toughness drastically increased from 58 J m^{-2} and reached a plateau value of around 2000 J m^{-2}. The two-order-of-magnitude toughness amplification was accompanied by the extensive volumetric shrinkage of the hydrogel upon the increase of Chit content. Both phenomena could be attributed to the phase transition behavior, which condensates the polymers and promotes the ionic crosslinks within the hydrogels. From both tests, the critical Chit: PAAc ratio was identified to be 0.222, at which fracture toughness surpassed 100 J m^{-2} (criteria for tough hydrogel) and volume ratio dropped below 1 (from swelling to contraction). The PAAc9/Chit3 with 0.333 Chit: PAAc ratio was selected as the default hydrogel formulation for the rest of this study.

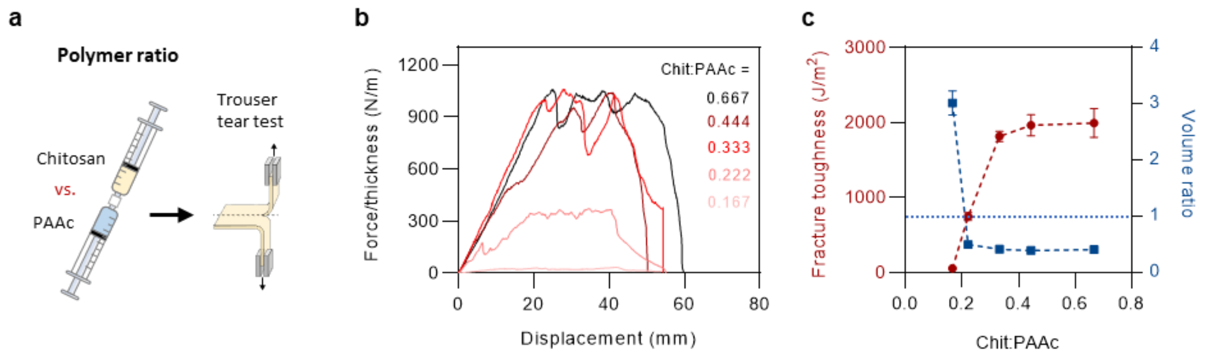

Figure 3.5. Effect of Chit: PAAc ratio on the phase transition and mechanical properties of the PAAc/Chit hydrogels. (a) Schematic illustration of the polymer ratio study. (b) Representative force/thickness–displacement curves from trouser tear tests and (c) the corresponding fracture toughness and volume ratio of the hydrogels with different Chit:PAAc polymer ratios after phase transition. Scatter plots are presented from representative data. Data are expressed as the mean ± SD from n = 3 samples.

3.2.3 Polymer content

With the selected polymer ratio Chit: PAAc of 0.333, the effect of total polymer content of the PAAc/Chit hydrogels was studied next. The hydrogels were prepared at total polymer concentrations of 4%, 8%, 12%, and 16% (w/v) and submerged in DI water for phase transition. Similarly, volume ratio of post-to-pre phase transition and fracture toughness was measured as evaluation criteria.

During trouser tear tests, as the two arms of the hydrogels were pulled apart, all hydrogels demonstrated crack blunting behavior, as shown in the representative photo in Figure 3.6a. This phenomenon underlined the significance of the optimized polymer ratio to the tough and crack resistance characteristics of the PAAc/Chit hydrogels. A force/width plateau was obtained for hydrogels of all polymer contents (Figure 3.6b). As total polymer concentration increased from 4% to 16%, the fracture toughness demonstrated a five-time increment from 440 to 2270 J m^{-2}. In the meantime, the volume ratio of the hydrogels increased marginally from 0.3 to 0.5 (Figure 3.6c). The results suggested that as the polymer concentration increased, denser polymer networks were formed. More physical entanglements, electrostatic interactions, and hydrogen bonds contributed to the energy dissipation, constructing a tougher material system. However, at the same time, the extent to which the polymers condensed were slightly impeded, resulting in higher macroscopic volume ratios.

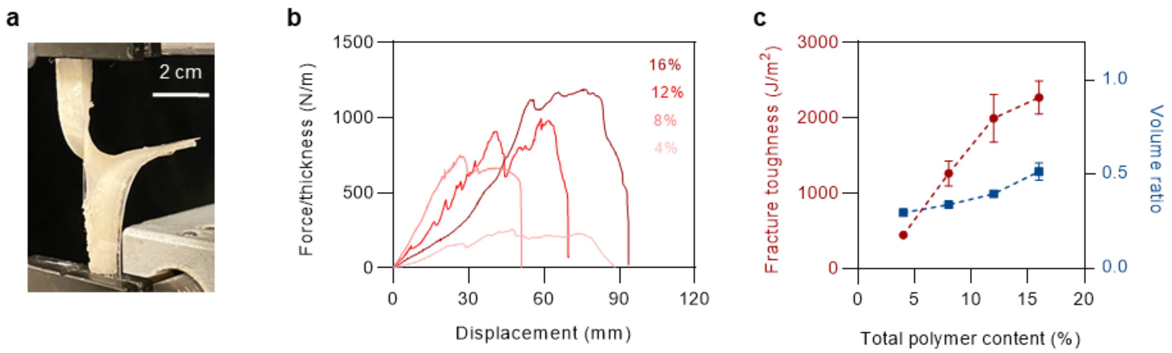

Figure 3.6. Effect of the total polymer content on the mechanical properties of PAAc/Chit hydrogels. (a) Digital image of the PAAc9/Chit3 hydrogel, (b) representative force/thickness–displacement curves from trouser tear tests, and (c) the corresponding fracture toughness and volume ratio of the hydrogels with different total polymer contents. Scatter plots are presented from representative data. Data are expressed as the mean ± SD from n = 3 samples.

3.2.4 Kinetics

To gain deeper understanding in the phase transition mechanism, kinetics studies were conducted by investigating how the mechanical and physical properties evolve with the time submerging in DI water. By hypothesis, the kinetics of phase transition involves both the diffusion of ions out of the hydrogel and the formation of new physical bonds between polymer chains.

Figure 3.7a illustrates the procedure of this study. The hydrogels were submerged in baths of DI water for predefined time periods and their volume ratio and fracture toughness were measured at each timestamp. The representative force/width–displacement curves were presented in Figure 3.7b, and the calculated volume ratio and fracture toughness were shown in Figure 3.7c. As the PAAc9/Chit3 hydrogels were immersed in water for prolonged time, higher extent of ion exchanges between the hydrogel with the environment occurred, reaching higher degrees of phase transition, and forming denser polymer networks. Consequently, the hydrogel volume ratio gradually decreased while the fracture toughness elevated until reaching plateaus after around 24 hours of immersion. The speed for both changes were high at first and slowed down at the vicinity of the plateau. This result further supported the theory that ion exchanges induced polymer condensation and caused macroscopic phase transition. It also served as calibration for future experimental operations.

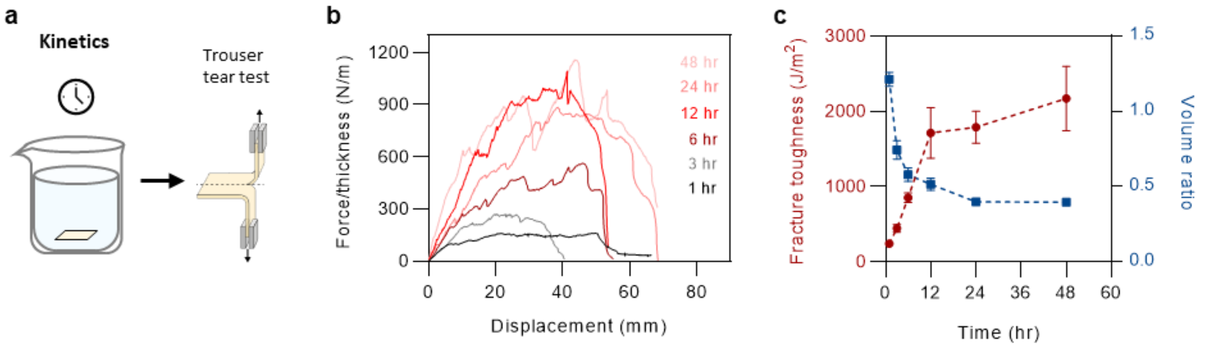

Figure 3.7. Kinetics of the phase transition of the PAAc/Chit hydrogels. (a) Schematic illustration of the kinetics study. (b) Representative force/thickness–displacement curves from trouser tear tests and (c) the corresponding fracture toughness and volume ratio of the hydrogels after immersing in DI water for predefined time stamps. Scatter plots are presented from representative data. Data are expressed as the mean ± SD from n = 3 samples.

3.2.5 Reservoir pH

To reveal the phase transition mechanism and explore its robustness, the PAAc9/Chit3 hydrogels were immersed in reservoirs of different pH values for 24 hours. Their volume ratio, fracture toughness, and tensile characteristics were evaluated.

Figure 3.8a–c presented the representative force/width–displacement curves during trouser tear tests for the PAAc9/Chit3 hydrogels after phase transition in baths of different pH. The PAAc9/Chit3 hydrogel exhibited excellent robustness to the environment pH, showing relatively stable fracture toughness of around 2200 J m^{-2} at the pH range of 3–9. A further raise of the pH level compromised the ionic interaction between the PAAc and Chit polymers and thus led to a weakened polymer network and attenuated the fracture toughness. A similar trend was observed in the volume changes. Hydrogels contracted to 0.4 times their initial volume after submerging to moderate pH environments, while demonstrated diminished degree of polymer network condensation and hence higher volume ratio (Figure 3.8c).

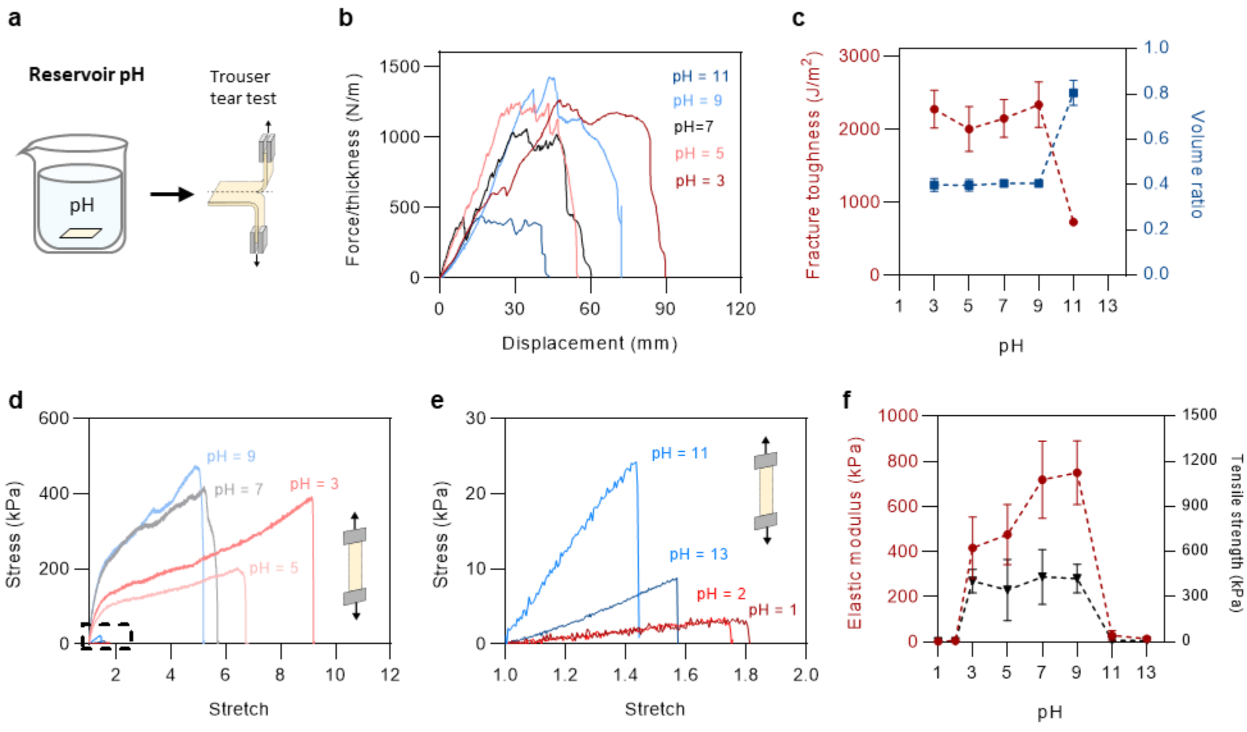

Figure 3.8. Effect of reservoir pH on the phase transition and mechanical properties of the PAAc/Chit hydrogels. (a) Schematic illustration of the reservoir pH study. (b) Representative force/thickness–displacement curves from trouser tear tests and (c) the corresponding fracture toughness and volume ratio of the hydrogels after immersing in reservoir of different pH values. (d) Representative stress-stretch curves with (e) enlargement at low strain region and (f) corresponding elastic modulus and tensile strength obtained from uniaxial tensile tests for the hydrogels after immersing in reservoir of different pH values. Scatter plots are presented from representative data. Data are expressed as the mean ± SD from n = 3 samples.

The effect of reservoir pH was further validated with uniaxial tensile tests. The representative stress-strain curves were plotted in Figure 3.8d with enlargement in the low strain region in Figure 3.8e. PAAc9/Chit3 hydrogels after phase transition in pH of 3–9 could be stretched more than 5 times their initial length until rupture. In contrast, those immersed in baths of pH of 1, 2, 11, and 13 displayed substantially lower stretchability (stretch number < 2). Elastic moduli and tensile strengths agreed well with the previous findings. Compared to pH of 3–9, the elastic moduli and tensile strengths of hydrogels that were immersed in extremely low and extremely high pH baths demonstrated two-orders-of-magnitude decreases, from ~600 to ~10 kPa and from ~400 to ~4 kPa, respectively. Despite the compromises, the pH at which phase transition and mechanical enhancement occurred still spanned a large range, denoting the environmental robustness of the phase transition mechanism.

3.2.6 Effect of covalent crosslinks

Given the carboxylate groups presented in the PAAc and the primary amine groups in Chit, covalent crosslinks could readily form with the addition of carbodiimide coupling reagent EDC/NHS[173]. The covalent crosslinks were hypothesized to synergize with the hydrogen bonds and electrostatic interactions in the material and further enhance the mechanical performances. To verify this, the mechanical and physical properties of the as-prepared and PT hydrogels with varying EDC/NHS concentrations were characterized by pure shear tests and volume ratio measurements.

Three concentrations of the EDC/NHS (5, 10, and 20 mg mL^{-1}) were tested. As shown in Figure 3.9a, increasing the coupling reagent concentration minimally affected the post-to-pre volume ratio of the PAAc9/Chit3 hydrogels during phase transition. These results indicate that the phase transition is governed by the ion exchange process and is negligibly affected by covalent crosslinks. As such, physical interactions play a predominant role in shaping physical properties.

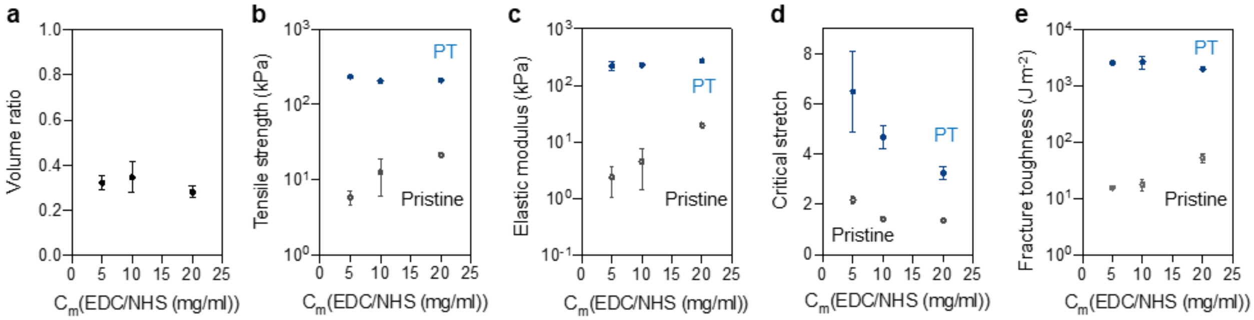

Figure 3.9. Effect of the amount of EDC/NHS to mechanical performances of the PAAc/Chit hydrogels in pristine state or PT state. Effects of the concentration of EDC/NHS on (a) PT: pristine volume ratio, (b) tensile strength, (c) elastic modulus, (d) critical stretch, and (e) fracture toughness of the PAAc/Chit hydrogels during pure shear tests. Data are expressed as the mean ± SD from n = 3 samples.

The input of EDC/NHS and the resulting covalent crosslinks have multifaceted effects on the mechanical properties of the hydrogels. In pure shear tests, several performance indexes could be obtained, including tensile strength and elastic modulus from the unnotched samples, and critical stretch from notched samples, as well as fracture toughness. Both tensile strength and elastic moduli of the pristine samples were greatly enhanced by the addition of EDC/NHS (Figure 3.9b-c). The values showed an order of magnitude increase when the coupling reagent concentration raised from 5 to 20 mg mL^{-1}. However, these effects were not as significant after phase transition, with a slight augmentation in elastic moduli and negligible changes in tensile strength. The results highlighted the stiffening effect of the additional covalent crosslinks to the hydrogels and confirmed the dominance of physical interactions in the PT hydrogels. On the other hand, Figure 3.9d shows that both the pristine and PT notched samples demonstrated drastic decrease in critical stretches when increasing the number of covalent crosslinks. This result is consistent with the implications from the Lake-Thomas model[174]. Consequently, whereas increasing coupling reagent content significantly augmented the fracture toughness of the originally soft pristine hydrogels, the fracture toughness of the PT samples displayed an increase followed by a decrease (Figure 3.9e). The result coincided with previous findings of the inverse relationship between fracture toughness and elastic modulus[21]. As such, to optimize for fracture toughness without significantly compromising stretchability, concentration of 10 mg ml^{-1} was chosen for other tests.

3.2.7 Adhesion

Aside from the excellent bulk properties, the PAAc/Chit hydrogels can form strong adhesion with diverse substrates. The adhesion performances were evaluated by adhesion energy measured by T-peeling or modified lap shear tests.

Figure 3.10a shows that the PAAc9/Chit3 hydrogels achieved tough adhesion to various substrates, including biological tissues (skin and heart) and PAAm/Alg tough hydrogel. The high interfacial toughness (> 300 J m^{-2}) could be observed by the cohesive failure in the hydrogels during peeling (Figure 3.10b). Although the adhesion energy is lower than those achieved using preformed patch adhesives, it outperforms clinically used injectable hydrogel adhesives such as COSEAL and TISSEEL (~ 50 J m^{-2})[175–177]. When the PAAc/Chit hydrogel interacted with biological tissues or other hydrogels, the initial adhesion was enabled by the physical interaction between the substrates and the carboxylic-acid rich PAAc. The effect was also observed when interacting with a rat liver in-vivo (Figure 3.10c). The PAAc/Chit then underwent condensation and phase transitioned into a tough matrix, which further amplified the energy-dissipation capacity of the matrix. To further enhance the adhesion performance, the PAAc/Chit hydrogel system has the capacity to incorporate the carbodiimide coupling reagent EDC/NHS. Not only could the coupling reagents covalently crosslink PAAc and Chit backbone polymer networks, but they also facilitate covalent bond formation between the hydrogel network and tissue surfaces[50]. Robust adhesion could also potentially be formed underwater[178–181]. The tough hydrogel matrix along with the strong bonding on the interface enabled enhanced adhesion performance.

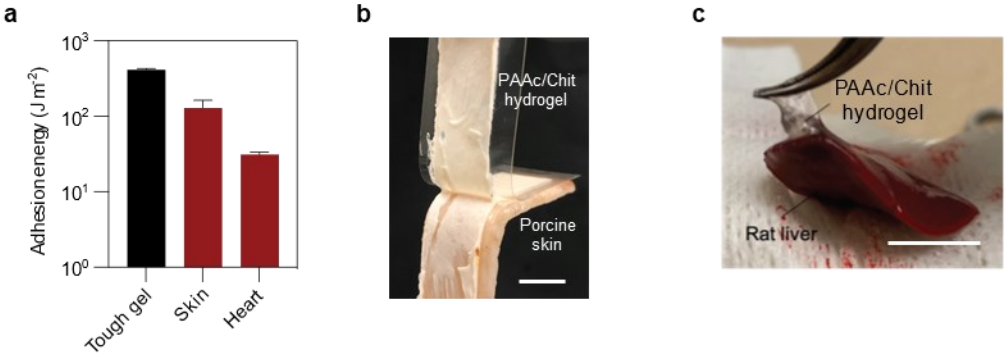

Figure 3.10. Adhesion performances of the PAAc/Chit hydrogels to diverse substrates. (a) Adhesion energy of the PAAc9/Chit3 hydrogels to PAAm/Alg tough hydrogel and other biological tissues such as porcine skin and heart. (b) Digital image of the PAAc/Chit hydrogel on porcine skin during T-peeling test, showing cohesive failure. (c) Digital image of the PAAc/Chit hydrogel forming strong adhesion on rat liver in-vivo. Scale bar, 1 cm. Data are expressed as the mean ± SD from n = 3 samples.

3.3 Electrical characteristics

The electrical conductivities were characterized for both the pristine and PT PAAc/Chit hydrogels, while electromechanical performances were only investigated for the PT hydrogels. These two tests provide insights into the electrical behaviors of the ionic materials, benchmark their performances, and offer guidelines for their use as ionic conductors or strain sensors in ionotronics.

3.3.1 Electrical conductivity

The electrical conductivity of the PAAc9/Chit3 hydrogels were obtained from the resistance value in ac-impedance measurements at 1 kHz frequency. As shown in Figure 3.11a, the pristine hydrogels exhibited electrical conductivity of around 0.55 S m^{-1}, regardless of the polymer concentrations. In contrast, polymer content contributes to the enhancement of conductivities for the PT hydrogels. Increasing the total polymer concentration from 8% to 16% (w/v) resulted in a 1.4-fold rise of the conductivity (from 0.022 to 0.053 S m^{-1}). Despite the augmentation, the performances were still one-order-of-magnitude lower than their pristine counterparts. The compromised ionic conductivity is hypothesized to be attributed to the combined effect of loss of mobile ions and reduced ionic mobility, which is elaborated in the discussion section.

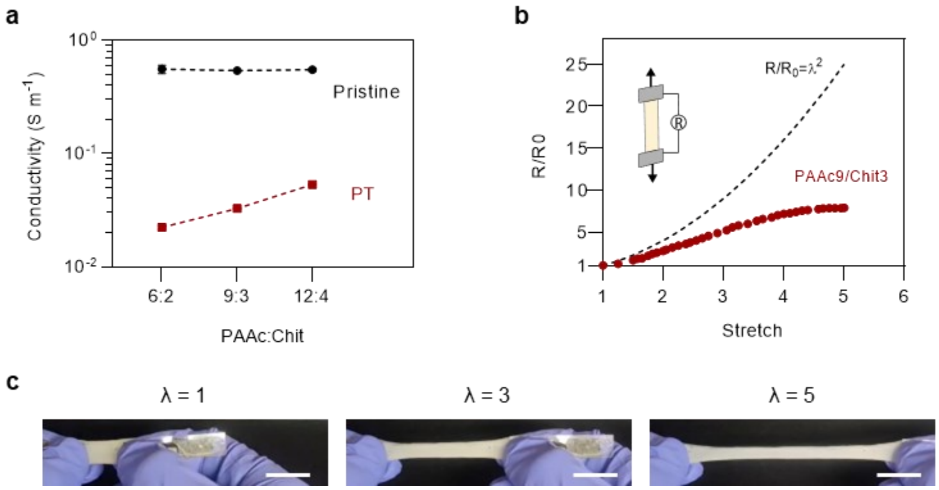

Figure 3.11. Electromechanical characterizations of the PAAc9/Chit3 hydrogels. (a) Conductivity of the pristine and PT PAAc/Chit hydrogels with different polymer content. (b) Normalized resistance as a function of stretch, with theoretical predictions for elastic ionic conductors. (c) Digital images of the PAAc9/Chit3 hydrogels during tensile stretching with electrical resistance measurement. Scale bar, 2 cm. Scatter plots are presented from representative data. Data are expressed as the mean ± SD from n = 4 samples.

3.3.2 Electromechanical characteristics

The electromechanical coupling of the PAAc/Chit hydrogels is important when applied to application scenarios involving frequent deformations. For conductors, stable conductivity or unchanged electrical resistance are desired to ensure reliable transmission of power or electrical signals. While for strain or pressure sensors, small changes in the dimensions are expected to be associated with larger changes in electrical responses to provide sensitive readouts.

The electrochemical coupling effect of the PT PAAc9/Chit3 hydrogels was investigated by measuring the electrical resistance during uniaxially tensile stretching. The electrical resistance was obtained as the resistance value in ac-impedance and was normalized by the initial resistance of the undeformed hydrogels. The results are presented in Figure 3.11b-c. The normalized resistance increased gradually as the hydrogels were stretched. The resistance-stretch curve displayed a linear relationship before stretch value reached 4 and demonstrated a gradual decreasing slop. The linear region possessed remarkable linearity, with a R^2 value of 99.6% in the linear regression analysis and GF of 2.22. The rise in resistance value did not follow the theoretical model predicted for ideal elastic conductors. In fact, the electrical resistance of the PT PAAc/Chit hydrogel counters the geometric effect, demonstrating a much slower increase. This is hypothesized to be due to the substantial changes in the dense polymer networks during large deformation, which affects their interactions with the mobile ions. Despite the moderate sensitivity, the linear region in electromechanical coupling curve stands to be useful in sensor design.

3.4 3D Printing

The pristine PAAc/Chit hydrogels with high ionic strength behave as a liquid and can be implemented as inks for extrusion-based 3D printing. 3D printing allows for precise deposition of the phase transitioning materials to construct high-resolution customizable 3D structures. The printed structures will go through mechanical enhancement after phase transition under diverse conditions and can be used in applications such as ionotronics, tissue repair, and as surgical tissue phantoms. In this section, to establish the printing method, the printing time window, printability, and phase transition after printing was investigated.

3.4.1 Time window

The mixture of PAAc soft gel and Chit solutions was stable, but the coupling reagent EDC/NHS gradually reacted with the polymers upon addition. The pristine ink was printable, but overtime, covalent crosslinks was formed, and the ink transitioned into a viscoelastic material that had compromised printability.

To investigate the reaction kinetics of EDC/NHS with the PAAc/Chit hydrogels and calibrate the time window during practical 3D printing operations, an oscillatory time sweep was performed using a rheometer. Two materials were studied in this test: a phase transitioning PAAc9/Chit3 containing 9% (w/v) PAAc and 3% (w/v) Chit; and a non-phase transitioning PAAc6/Chit1 with 6% (w/v) PAAc and 1% (w/v) Chit. As shown in Figure 3.12a-b, *G'* of both inks increased over time, validating the effect of EDC/NHS in the formation of covalent crosslinks. *G'* of PAAc9/Chit3 rose from 527 Pa to 629 Pa, while *G'* of PAAc6/Chit1 demonstrated a ~2-fold increase from 116 Pa to 194 Pa. The results were as expected, since PAAc9/Chit3 possesses a higher total polymer content than PAAc6/Chit1, and thus exhibited larger moduli. In the meantime, the loss moduli stayed relatively constant for both materials. No crossover point was observed for either material, and *G'* was always larger than the *G"*, indicating solid-like behavior for both materials at low shear strain of 0.5% and low frequency of 1 Hz.

The printing time window after the addition of EDC/NHS was determined empirically to be the time period during which *G'* increased 50% of the total increase until plateau and can be formulated as: $G'_{window} - G'_{t=0} = 0.5(G'_{plateau} - G'_{t=0})$, where G'_{window} and $G'_{t=0}$ represents the storage modulus at the end of the printing time window and at the beginning of the test, respectively. The results were plotted in Figure 3.12c. Both materials possessed time windows of around 40 minutes, with PAAc9/Chit3 having slightly shorter ones. The printing time windows were long enough for the preparation of inks into cartridges, calibration of the bioprinter, and the printing process, but not too long for the printed structure to wait for stabilization. Adjusting the EDC/NHS amount could potentially tune the time window.

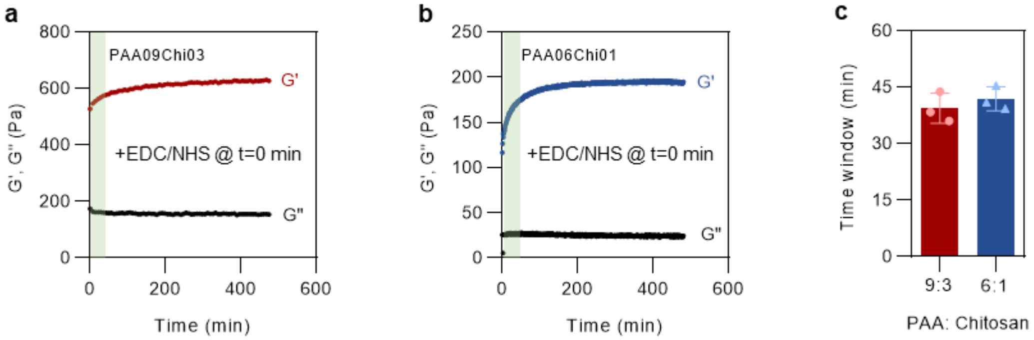

Figure 3.12. Printing time window characterization for the PAAc/Chit hydrogel inks. (a) *G'* and *G"* as a function of time during isothermal oscillatory time sweep at shear frequency of 1 Hz and shear strain of 0.5% right after addition of EDC/NHS to the materials at t = 0. Hydrogels include 9% PAAc and 3% Chit (PAAc9/Chit3) and (b) 6% PAAc and 1% Chit (PAAc6/Chit1). Green region indicates the calculated printing time window. (c) Time window for the two hydrogels. Scatter plots are presented from representative data. Data are expressed as the mean ± SD from n = 3 samples.

3.4.2 Printability

The printability of the PAAc/Chit hydrogels was characterized by rheology. The printability was evinced by four material attributes: shear yielding, shear thinning, self-recovery, and yielding point. The PAAc/Chit hydrogels exhibited solid characteristics under static states. As shown in Figure 3.13a, upon application of an external force, the PAAc/chit hydrogel started to extrude from the printer nozzle. To characterize this, as shear stress increased, the *G'* for hydrogels of all concentrations maintained a steady level, until reaching a critical point. They demonstrated shear yielding behavior, signified by the drastic storage modulus drop during shear stress sweep (Figure 3.13d). Higher total polymer content resulted in a higher *G'* before yielding, with *G'* increasing from 75 Pa to 350 Pa to 660 Pa when the polymer concentration increased from 8% to 12% to 16% (w/v).

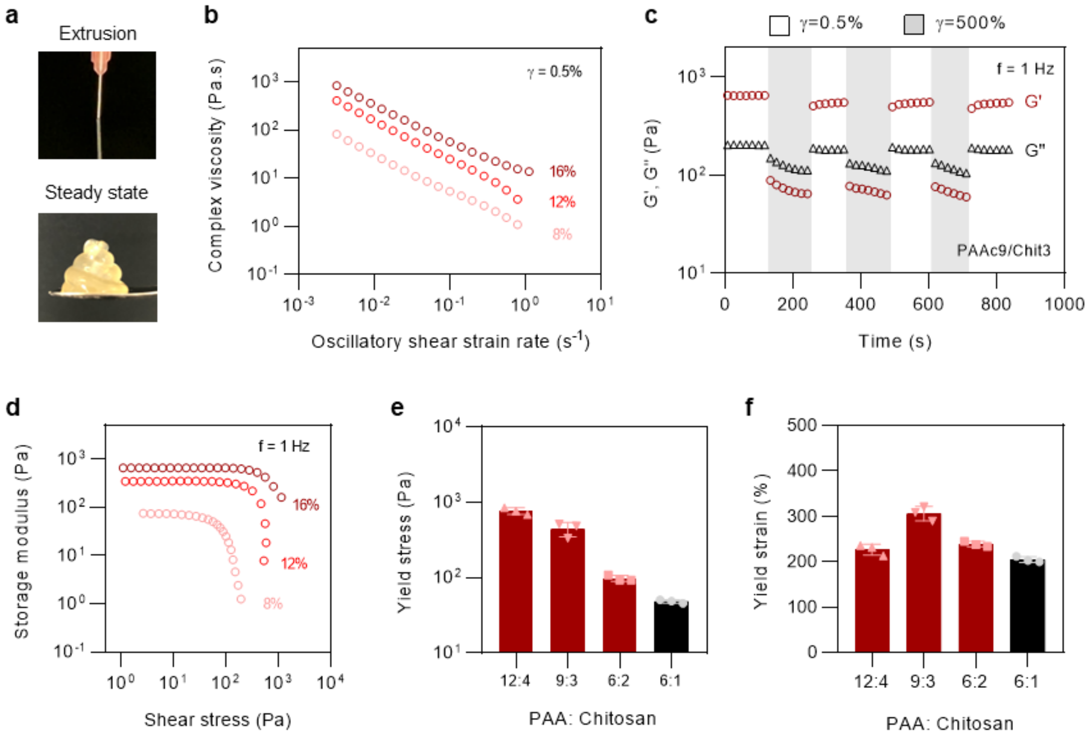

Figure 3.13. Rheological characterizations of the PAAc/Chit hydrogels of 3:1 PAAc: Chit ratio. (a) Digital images of the PAAc9/Chit3 hydrogel during extrusion and at steady state. (b) Complex viscosity as a function of shear rate at shear strain $\gamma = 0.5\%$ at oscillatory frequency $f = 1$ Hz for PAAc/Chit hydrogels with different total polymer content. (c) *G'* and *G"* through high shear strain ($\gamma = 500\%$) to low shear strain ($\gamma = 0.5\%$) oscillatory time sweep cycles at frequency $f = 1$ Hz for PAAc9/Chit3 hydrogels. (d) *G'* as a function of shear stress at oscillatory frequency $f = 1$ Hz for PAAc/Chit hydrogels with different total polymer content. (e) Yield stress and (f) yield strain obtained from the shear stress sweep. The yielding points are determined by the points where *G'* and *G"* intersect. Scatter plots are presented from representative data. Data are expressed as the mean ± SD from n = 3 samples.

After yielding, the hydrogel started to behave like a liquid. Flowing of the hydrogels resulted in increases of the shear rates. Figure 3.13b demonstrated that as oscillatory shear rate increased, the complex viscosities decreased nonlinearly at small shear strain of 0.5%. Shear thinning behavior of the PAAc/Chit hydrogels ensured smooth and continuous extrusion upon initiation.

After exiting from the nozzle, the PAAc/Chit hydrogels are expected to self-recover from the liquid state to solid state. To validate this point, self-recovery tests were conducted by applying cyclic oscillatory time sweep with high (500%) and low shear strains (0.5%). Each period was designed to be 120 s to ensure the material reached a steady state at corresponding strain condition. The results were presented in Figure 3.13c. At low strain, *G'* was larger than *G"*, indicating a solid state. Upon applying a high strain that was high enough to yield the material, *G"* was immediately higher than *G'*, suggesting a liquid state. The instantaneous recovery to solid state was evinced by the rapid transition of moduli when switching back to low strain. The self-recovery process was repeated for three cycles to assure reliability.

A yielding point in the range of 100 – 1000 Pa would facilitate extrusion of the ink and ensure structural rigidity for the printed structure to hold[182]. As shown in Figure 3.13e, the PTAs yield at 98 Pa to 442 Pa to 765 Pa shear stresses as the total polymer content increased from 8% to12% to 16%. The yielding stresses also corresponded to yielding strains of 240%, 306%, and 230% for the inks, respectively (Figure 3.13f). Considering the yield stress and complex viscosity, the PAAc9/Chit3 was selected as the model hydrogel for the rest of this study. In addition, the non-phase transitioning PAAc6/Chit3 hydrogel was also validated with the shear yielding, shear thinning, and self-recovery abilities to be used in later studies (Figure 3.14).

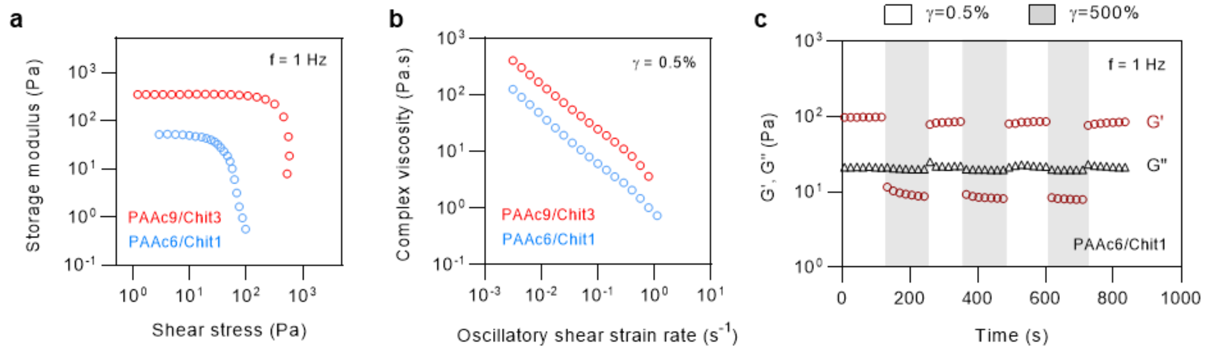

Figure 3.14. Rheological characterizations of the PAAc6/Chit1 hydrogels. (a) *G'* as a function of shear stress. (b) Complex viscosity as a function of shear rate at shear strain $\gamma = 0.5\%$. (c) *G'* and *G"* through high shear strain ($\gamma = 500\%$) to low shear strain ($\gamma = 0.5\%$) oscillatory time sweep cycles. Unless otherwise

stated, rheological tests were conducted at oscillatory frequency f = 1 Hz. Scatter plots are presented from representative data from n = 3 samples.

3.4.3 Printing and phase transition by diverse trigger

Unlike most strategies for 3D printed hydrogels that require gelation or post-crosslinking for a second polymer network, the PAAc/Chit hydrogels strengthen the existing polymer network post-printing. Combining with 3D printing, this unique triggering effect and diverse conditions to induce pH changes in the material were explored in several intriguing applications (Figure 3.15a).

First, Figure 3.15b presented a printed miniature octopus with PAAc9/Chit3 hydrogel, demonstrating high resolution and excellent shape fidelity. The as-printed structure was translucent. Instead of immersing in DI water, the octopus underwent phase transition when immersed in saline (0.9% NaCl) solution that mimicked the human body fluids in vitro. The octopus underwent isotropic contraction and maintained its structure, while appearing to be opaque and white after the transition. The isotropic shape change preserved the designed structural features and promised the application of this material in printing ionotronics with controlled device structures.

The pH change could also stem from the printing substrates. As illustrated in Figure 3.15c, when printed directly on a piece of porcine skin, the “M” shaped PAAc/Chit hydrogel experienced pH change and rapidly phase transitioned into a white tattoo. In this case, due to the strong adhesion between the printed hydrogel and skin surface, the contraction was anisotropic. The majority of the shrinkage occurred in the out-of-plane direction, while the stroke of the letter “M” narrowed moderately. This feature is useful for printing planar structures.

Similarly, hydrogels can also provide the environment for pH change and can be employed as substrates during printing of the PAAc/Chit hydrogels. As shown in Figure 3.15d, a planar mesh structure was directly printed on a piece of PAAm/Alg tough hydrogel substrate. The printed mesh phase transitioned within 10 minutes and stably adhered to the substrate. As such, the mesh could deform along with stretching of the substrate hydrogel and subsequently returned to its original shape after releasing of the force (Figure 3.15e). The hybrid structure maintained structural integrity throughout the process.

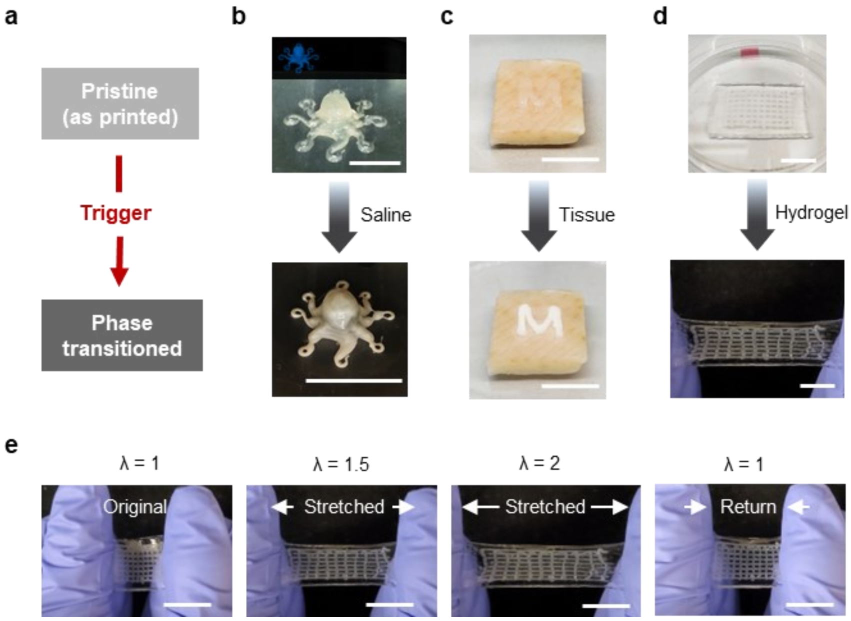

Figure 3.15. Phase transition of printed structures via diverse triggers. (a) Schematic illustration of printed PAAc/Chit hydrogel structures phase transition after benign triggers. Digital images of pristine and PT (b) 3D-printed octopus triggered by saline, (c) printed letter "M" triggered by contacting porcine skin, and (d) printed mesh triggered by contacting PAAm/Alg hydrogel. (e) The printed PAAc/Chit hydrogel mesh on PAAm/Alg hydrogel hybrid can be stretched and return to its original shape after release. Scale bar 1 cm.

3.5 Demonstration of Applications

In this section, with the optimized material formula, established mechanical characteristics, phase-transitioning mechanisms, printing parameters, and electrical properties, the potential applications of this 3D printable PAAc/Chit hydrogel are demonstrated. These include an ionotronic strain sensor, 3D printing of tissue mimetics, patterned adhesions, and printing of morphing structures.

3.5.1 Strain sensors

The first demonstrated application is a printed strain sensor. The PAAc/Chit hydrogel is physically stable under ambient light and temperature conditions. Together with its high stretchability, toughness, and resistance-stretch linearity, the PT PAAc/Chit hydrogel is suitable for use as a resistive strain sensor. To demonstrate this, the hydrogel was employed as a strain sensor to detect the bending angles of a finger. To fabricate the device, two carbon electrodes were attached to both sides of a piece of PAAc9/Chit3 hydrogel, and the hybrid structure was affixed to the back of a finger at a knuckle.

The measured resistance elevated with the increase of finger bending angle from 0° to 80°, attributed to the shape change associated with the elongation of the PAAc/Chit hydrogel (Figure 3.16c). The resistance value subsequently dropped back when finger returned to a straight position. Figure 3.16a demonstrated both slow and fast full-range motions with good repeatability. Following cycles of bending, a minor baseline shift in resistance was observed, due to the plastic deformation in the material. To quantitatively assess the performance of this strain sensor, resistance values were measured at various bending angles, and the results were presented in Figure 3.16b. The device displayed a linear response with an R^2 value of 93.04%. From the slope from the linear fitting, the GF was determined to be 0.7 kΩ deg^{-1}.

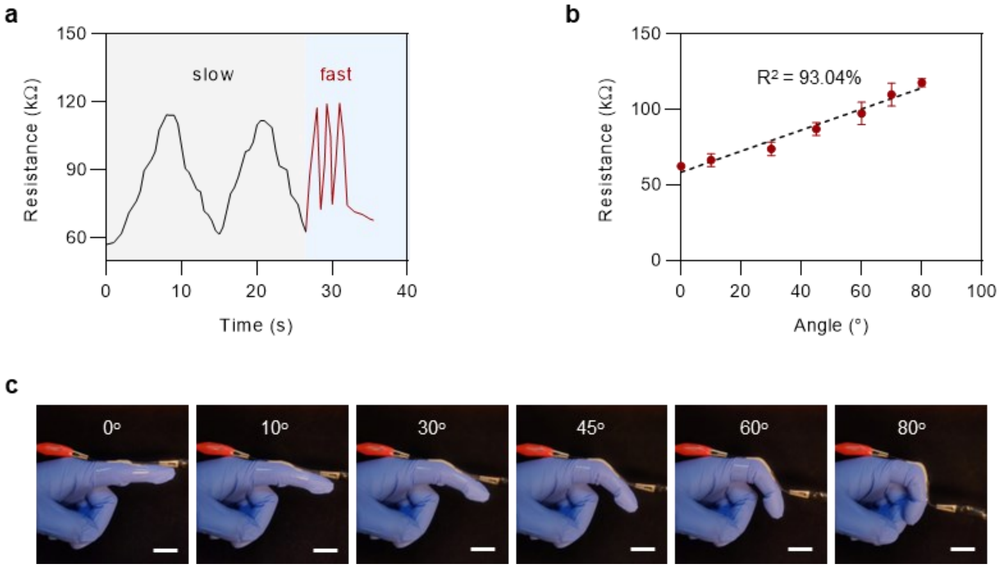

Figure 3.16. Soft and stretchable strain sensor for detecting finger bending angle. (a) Electrical resistance measurements as a function of time during bending of finger, with two slow movements and three fast ones. (b) Resistance as a function of bending angle. Black dotted line represents linear fitting result. (c) Digital images of finger bending from 0° to 80°. Scatter plots are presented from representative data. Data are expressed as the mean ± SD from n = 3 samples. Scale bar, 2 cm.

3.5.2 Tissue mimetics

Next, we demonstrated 3D printing of tissue mimetics. As the PT PAAc/Chit hydrogel are strong and tough, they serve as suitable candidates to mimic the load-bearing tissues such as aorta, tendon, ligament, meniscus, and intervertebral discs (IVD). 3D printing endows the tissue mimetics with accurate shapes and structures. Along with the flexibility in material system design, it enables customization to accommodate for shape and property variations among different patients in the case of repairs or implants.

Figure 3.17a–d presents an array of 3D-printed tissue mimetics, including an aorta, tendon, and lateral and medial meniscus using the PAAc9/Chit3 hydrogel inks. The printed structures closely mirrored the computer-aided design (CAD) models, showcasing outstanding resemblance to the intended shapes. They appeared translucent in light yellow color, with slightly visible printing filaments. Merging of the filaments were achieved by the hydrogen bonds between homogeneous materials and could be facilitated with the addition of EDC/NHS. Notably, the perimeters and infills of the filaments were designed to simulate the fiber orientation in native tissues, so as to exploit the effect of load bearing and tear resistance. The printed tissue mimetics stabilized for 24 hours post-printing, and phase transitions were triggered by submergence in DI water. As illustrated by the medial meniscus in Figure 3.17d, the phase transition initiated from the surface of the structure, where the surface transformed into white before appreciable volume change. The entire phase transition process required 48 hours, leading to considerable reductions in volume.

The printed hydrogel mimetics resembled the tough and crack-resistant features of the native load-bearing tissues. To demonstrate this, an initial crack was introduced on the 3D-printed meniscus and blood vessel mimetics. Upon stretching, no crack propagation was observed even when supraphysiological strain is applied (Figure 3.17e). The crack-resistance could be ascribed to the tough hydrogel matrix and the printed filament orientation, indicating the potential of the PAAc/Chit hydrogels to be used as tough biological tissue substitutes.

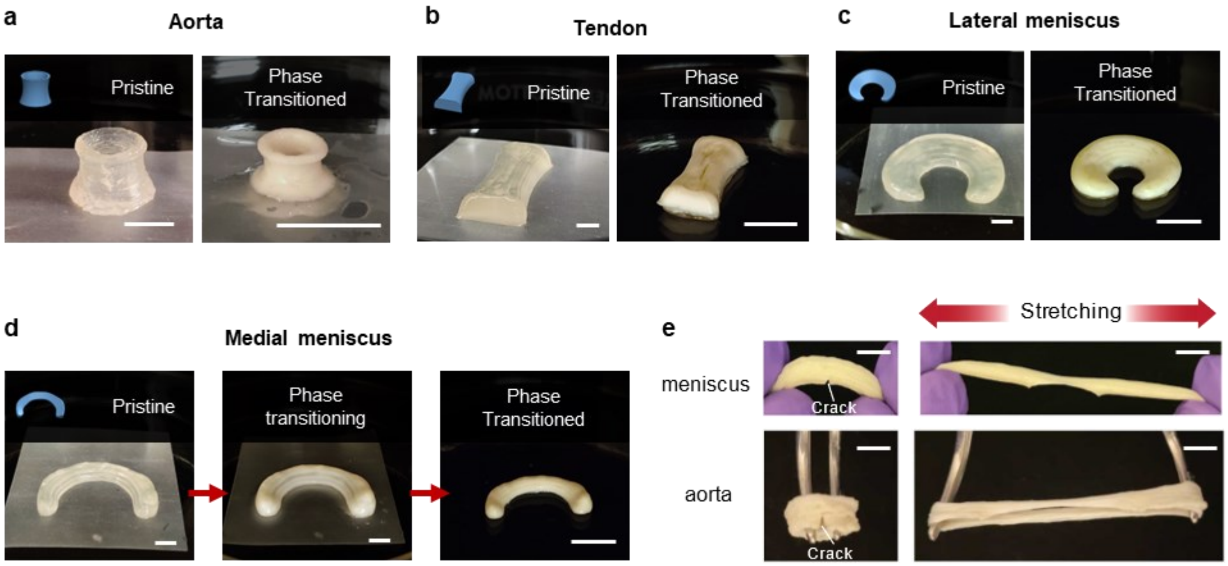

Figure 3.17. 3D-printed tissue mimetics. (a) 3D CAD models and digital images of the 3D-printed tissue mimetics before and after phase transitioning, including aorta, (b) tendon, and (c) lateral meniscus. (d) 3D CAD models digital images of the 3D-printed medial meniscus showing the phase transition process. (e) 3D-printed tissue mimetics are stretchable, tough, and crack-resistant. Scale bar, 0.5 cm.

3.5.3 Patterned adhesion

In this demonstration, we focus on combining the printability and adhesiveness of our material system. Leveraging the pattern ability and adhesiveness of the PAAc/Chit hydrogels, the boundary of the adhesive region could be precisely defined, creating arbitrary patterns on substrate surfaces or air/liquid pocket between two substrates.

As shown in Figure 3.18a,b, PAAc/Chit hydrogels were selectively printed in between two pieces of PAAm/Alg hydrogels to create air pockets and liquid channels. To create the air pocket, PAAc9/Chit3 inks were directly printed on one piece of substrate hydrogel in the shape of a planar rectangle with a circular cutout in the middle. Next, another piece of hydrogel was placed on the printed inks to complete the hydrogel pocket hybrid. The PAAc/Chit hydrogel underwent phase transition to form adhesion and stabilized the whole assembly. The circular cutout defined the shape and size of the un-adhered pocket region, while the peripherals enabled adhesion. To validate the patterned adhesive, two arms of the PAAm/Alg hydrogel were stretched similar to T-peeling tests. Adhesive failure was observed for the hydrogel pocket hybrid, where the adhesive, PAAc/Chit hydrogel, ruptured. Despite the fact, the air pocket was vastly obvious with clear boundaries between adhered and non-adhered regions. The printed pocket could potentially be generalized to create selective wound patches. Delicate wound beds could be protected with the non-adhesive region, while strong adhesion to surrounding healthy tissues could be formed to promote tissue regeneration and wound closure[183]. Alternatively, as the pocket was also liquid-tight, it could be applied as drug depots for drug delivery applications[184].

Similarly, a fluidic channel was created, as demonstrated in Figure 3.18 b. The channel was thin with distinct edges and largely preserved the designed shape features. Upon slow injection of water that was colored with red dye from the inlet on the left, the water went through the non-adhesive region between two gels, filling up the cavities, and exited from the outlet on the right. Since the adhesion interface is robust and flexible, the resulting device was highly deformable and no leakage through the PAAc/Chit adhesive interfaces was observed.

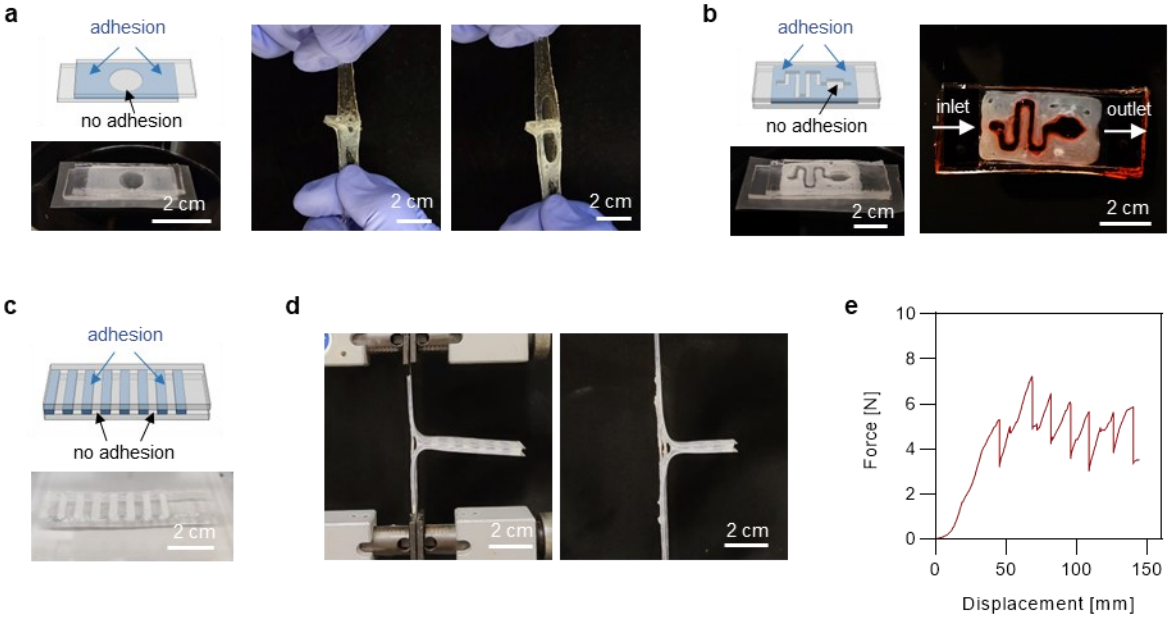

Figure 3.18. Patterned adhesion achieved by 3D printing PAAc/Chit hydrogels. (a) 3D CAD models and digital images of 3D-printed pouch, (b) fluidic channel, and (c) strips formed by selective adhesion of two pieces of PAAm/Alg tough hydrogels with the PAAc/Chit hydrogels. (e) Representative force–displacement curve for T-peeling tests of the selectively adhered PAAm/Alg tough hydrogels.

Next, selective adhesive was further demonstrated in Figure 3.18c. Adhesive PAAc/Chit hydrogel was printed as grids with predefined intervals to adhere two pieces of PAAm/Alg hydrogels. The distinctive adhesion performances between adhered and non-adhered regions were visualized with T-peeling tests. As the adherends were pulled in the direction perpendicular to the grid direction, PAAc/Chit hydrogel strongly adhered to the adherends, while gaps appeared in non-adhesive region. This effect was especially evinced by the elongated PAAc/Chit hydrogel shown in Figure 3.18d, as they dissipated energy and enhanced the adhesion performances in that specific region. The representative force–displacement curve was presented in Figure 3.18e, which featured a sawtooth shape. Increases of the forces corresponded to the adhesion region, whereas sudden drop in forces indicated ruptures of the adhesives. Valleys of the force curves did not reach zero due to the small intervals between the PAAc/Chit adhesives, where the next strip of adhesive started to dissipate energy before complete debonding of the two adherends. To further increase the adhesion contrast, a larger interval between strips could be implemented. This result also illuminated the high customizability of this printable adhesive to fit diverse application scenarios.

3.5.4 Morphing structures

Combining printability with shape changing characteristics could lead to 3D-printed morphing structures. Whereas most hydrogels swell in water, the PAAc/Chit hydrogels allow one to tune its swelling or shrinkage via polymer ratio. By manipulating this highly tunable property, 4D printing, that is 3D printing with shape, property, or functionality change ability upon predetermined stimuli, could be achieved[185–187].

To prove this concept, PAAc9/Chit3 hydrogel grids were printed on a single rectangular shaped PAAm/Alg hydrogel substrate in predefined directions (Figure 3.19a). Bands with 1.2 mm width and 2 mm intervals were patterned on the substrate hydrogels. Through ion exchange from the substrate hydrogel, the PAAc9/Chit3 hydrogels went through phase transition and strongly adhered to the substrate, forming a cohesive assembly. When immersed in a reservoir of DI water, the PAAc9/Chit3 hydrogels experienced phase transition and contracted in volume. In the meantime, the substrate hydrogel swelled and increased its volume until reaching an equilibrium. Despite the distinct volume change, the two hydrogels remained bonded, due to the strong adhesion between the two hydrogels. Swelling of the substrate hydrogel was highly anisotropic. Volume expansion in the direction along the PAAc9/Chit3 hydrogel bands and at the contacting surface was significantly constrained, whereas, swelling in other directions and locations were marginally affected. Consequently, the hydrogel assemblies curled up along the band direction towards the contacting surface. Such shape changes were highly controllable with 3D-printed bands and were demonstrated with in-plane band directions of 0°, 45°, and 90° with respect to the x-axis.

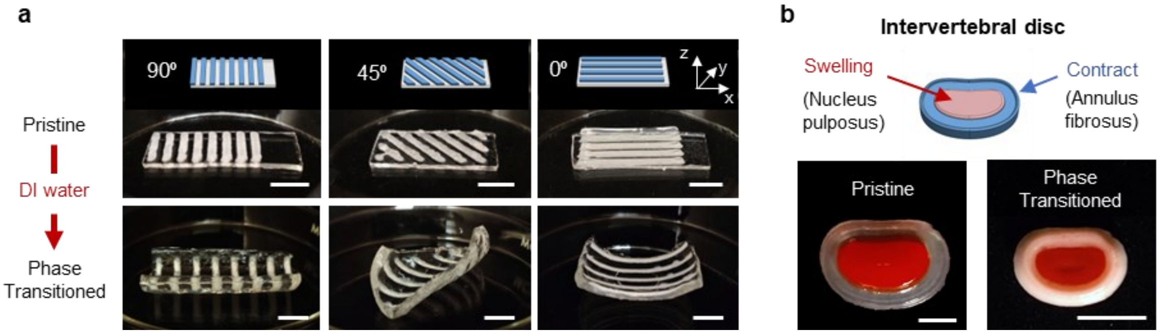

Figure 3.19. 3D-printed morphing structures. (a) 3D CAD models and digital images of 3D-printed PAAc/Chit hydrogels on PAAm/Alg tough hydrogel hybrids that experienced shape morphing when submerged in DI water. The curled shapes were controlled by the printing direction of the PAAc/Chit strips. Scale bar, 1 cm. (b) 3D CAD models and digital images of 3D-printed intervertebral discs with swelling PAAc6/Chit1 to mimic inner nucleus pulposus and contracting PAAc9/Chit3 to mimic outer annulus fibrosus. Scale bar, 0.5 cm.

4D printing could also be achieved using PAAc/Chit hydrogels of different polymer ratios. As discussed in Section 3.2, while PAAc9/Chit3 hydrogel contracts in DI water, the PAAc6/Chit1 hydrogel swells instead. With the printability of both formulations confirmed in Section 3.4. an IVD with outer annulus fibrosus (AF) and inner nucleus pulposus (NP) structure was 3D-printed (Figure 3.19b). The tough AF tissue was printed with PAAc9/Chit3 hydrogel in concentric pattern to mimic the native lamellar structure. Conversely, the soft and viscoelastic NP tissue was printed with PAAc6/Chit1 hydrogels in red. The two parts seamlessly merged thanks to hydrogen bonds and EDC/NHS. When submerged in a reservoir of water, the outer PAAc9/Chit3 phase transitioned and tended to restrict the swelling of the inner PAAc6/Chit1 radially. The mismatched mechanical behavior is a resemblance to the native IVD and manifested by the appearance of surface wrinkle. Consequently, the two structures exerted counter forces to each other, and ultimately led to a compact and stable IVD mimetics. This demonstration illuminated the capability of this single material system in biomimetic 4D printing.

CHAPTER 4

3D Ionic Microgel Printing of Ionic Devices

The toughening strategy based on phase transitioning of polyelectrolyte complex presented in Chapter 3 could substantially improve the mechanical performances of post-printed structures. However, this strategy and the resulting devices face limitations, including size shrinkage, low conductivity, and limited electrical functionalities. Overcoming these limitations calls for new 3D printing strategies. Aside from ionic conductive components, diversifying the ionic elements within ionotronic devices could lead to more functionalities. To do so, this chapter presents a new 3D printing strategy, featuring ionic microgels and DN crosslinking. The design of the material system is described, and the 3D IMP method is elaborated. Characterizations of the printing quality, electrical and electrochemical behavior, as well as mechanical performances are presented. At last, a variety of ionotronic devices, including ionic bipolar junction transistors, ionic full-wave rectifiers, and ionic touchpads are further demonstrated. The presented 3D printing technology and findings in this chapter motivate the future development of high-performance ionotronics.

4.1 Design of the 3D Ionic Microgel Printing

To design materials that support extrusion-based 3D printing of ionic devices, there are several design criteria to satisfy: (1) high printing quality for successful deposition of the materials according to designed device 3D architecture; (2) ink modularity for optimization of individual inks and spatial combination of materials after printing without inter-material contamination; (3) mechanical robustness to accommodate to the large deformations when interfacing with human during daily activities and to ensure stable and durable operation during device lifespan; and (4) inter-component adhesion to prevent delamination and reinforce structural integrity.

To satisfy these requirements, a strategy that combines microgel printing with DN crosslinking method is proposed. As illustrated in Figure 4.1a, jammed microgels containing different ionic species such as polyanion (p-type), polycation (n-type), or mobile ions (ionic conductor) form diverse ink modules. These ink modules can be independently tailored in terms of printability, mechanical performance, and charge densities by tunning the ionic species concentrations and the matrix polymer concentrations. In the meantime, these ink modules can freely combine during printing process for complex spatial configurations to satisfy device design requirements. Unlike most 3D printing methods that rely on liquid precursors, 3D IMP has three main advantages. First, the intrinsic printability of microgel inks decouples printability from mechanical properties and ionic functionalities, circumventing the tedious balancing process during the design of 3D printable ionotronic devices[39,188]. Second, the microgel ink modules, owing to their solid nature, do not diffuse and undermine the ionic functions during printing. After ink deposition, the microgels can be closely packed to form intimate contact between the homogeneous or heterogeneous species, establishing ionic interaction through the microgel surfaces. While the ionic species are encapsulated in individual microgels, the microgel acts as a physical barrier for the diffusion of ionic species or their migration under electric field. Therefore, unlike liquid inks that tend to flow and diffuse, the ionic microgels do not mix during printing or operation, ensuring stable ionic functions. Third, the microgel inks are porous, which allows monomers, crosslinkers, and initiators to diffuse into and in between microgels before printing and to polymerize into a second network after printing. As such, we could not only toughen the individual microgels but also fuse them together within a percolating network for a tough and cohesive device[110].

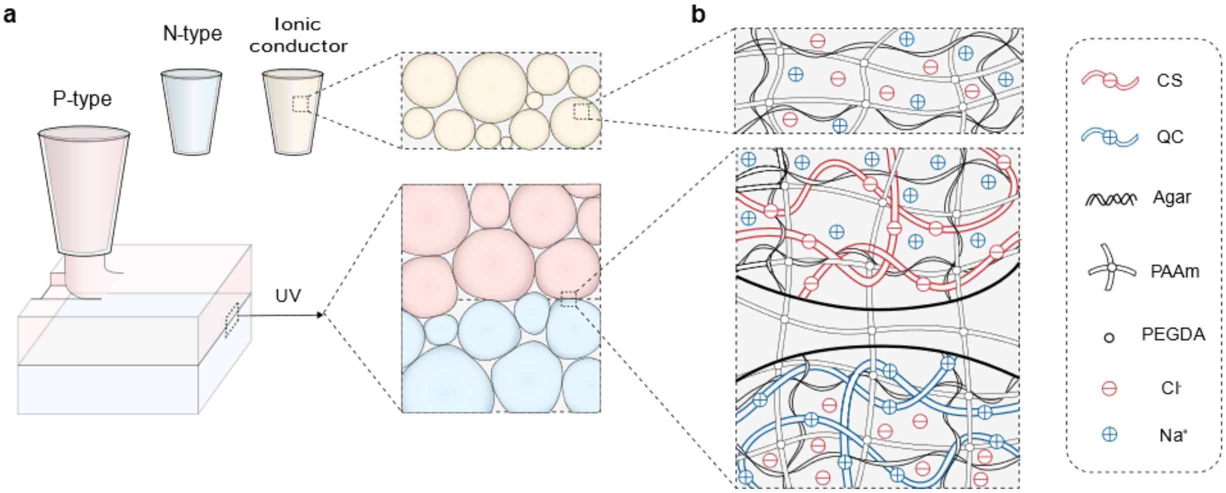

Figure 4.1. Schematic illustration of the 3D IMP. (a) Schematic of 3D IMP of p-type and n-type, as well as ionic conductors. (b) Schematic of the material design including the DN polymer backbone and various ionic species.

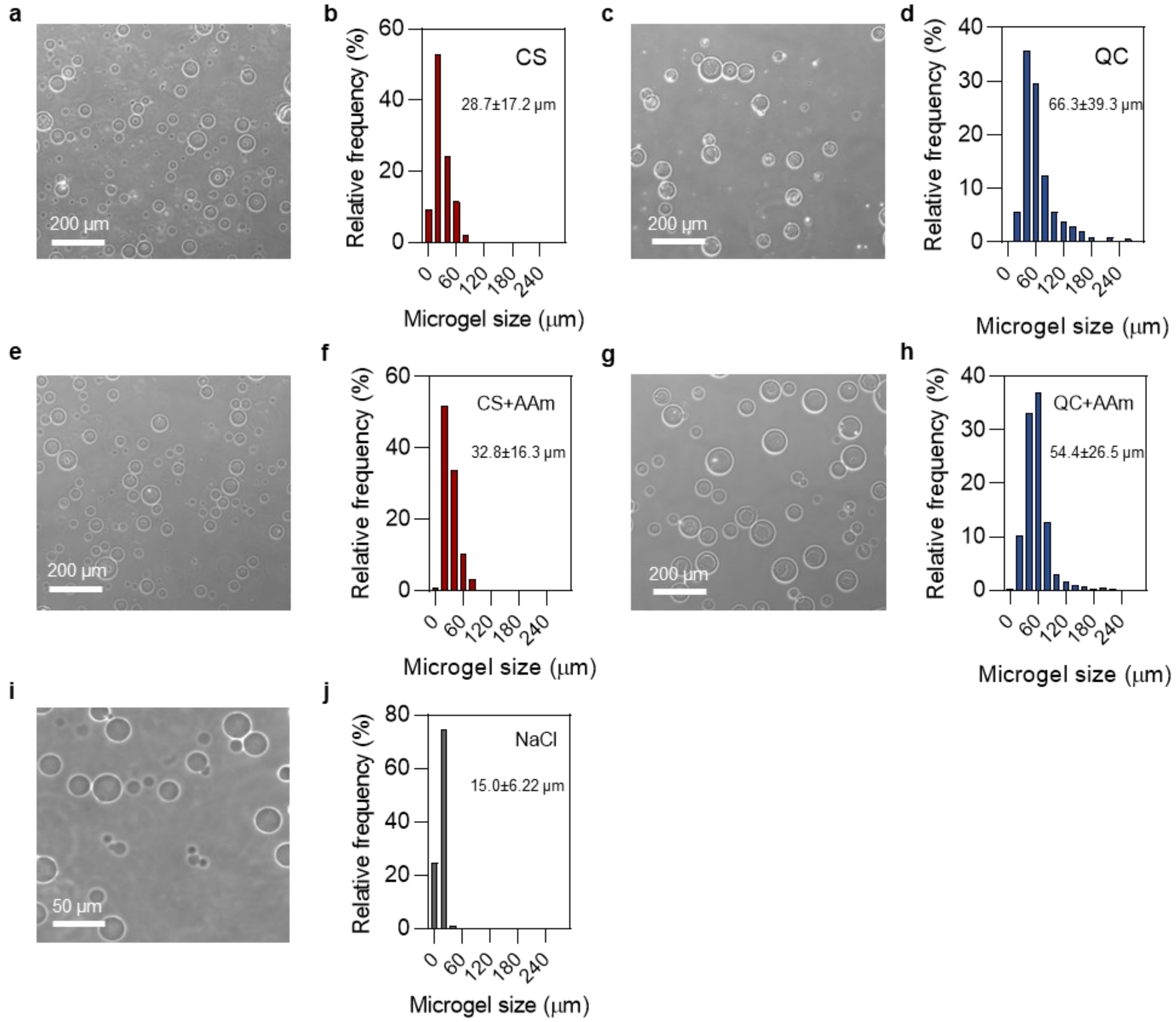

Figure 4.2. Optical microscope image and size distribution of microgels suspended in different solutions. (a, b) CS microgels suspended in DI water, (c, d) QC microgels suspended in DI water, (e, f) CS microgels suspended in PAAm gelling solutions, (g, h) QC microgels suspended in PAAm gelling solutions, and (i, j) NaCl microgels suspended in 3 M NaCl and PAAm gelling solutions. Size distribution of microgels were obtained by measuring the sizes of 780 microgels for each kind via ImageJ.

In this study, the base material system that constitutes the matrix was Agar/PAAm DN microgels embedded in a secondary PAAm network (Figure 4.1b). The agarose hydrogels go through gelation by forming physical crosslinks (coil to helix transition) when the hot agarose aqueous solution temperature drops below a critical temperature, typically around 35 °C[189,190]. The PAAm hydrogel network forms covalent crosslinks with AAm as monomer, PEGDA as degradable crosslinker, and I2959 as the photoinitiator. The two materials are selected due to their general electrical neutrality, ability to form tough DN hydrogels with one physical and one covalent crosslink, and ease of fabrication. To build an ionic conductor, 3M NaCl was added to the microgels and acted as the main charge carries[51,86]. To form p-type hydrogels, negatively charged chondroitin sulfate sodium (CS) was doped into the microgels and immobilized within the polymer network, while positively charged quaternary chitosan ammonium (QC) was added to the microgels to form n-type hydrogels. These two polyelectrolytes were selected over the negatively charged PAAc and positively charged chitosan used in the previous chapter due to the following two reasons. First, PAAc and Chit are weak polyelectrolytes that partially dissociate and release counterions in aqueous solutions according to the pH conditions, whereas CS and QC are strong polyelectrolytes and possess fixed charges on their polymer chains. Second, CS and QC possess one of the highest charge densities among biopolymers. These two attributes are crucial merits for high-performance hydrogel ionotronics.

The ionic microgels were produced by batch emulsion, where hydrogel precursors form droplets under agitation and crosslink into microgel particles. Optical microscope images were used to determine the morphology and size distribution of three different species of microgels suspended in DI water or PAAm gelling solution. As shown in Figure 4.2, all resulting microgels were in spherical shape and heterogenous in size. The CS doped microgels exhibited mean diameter of 28.7±17.2 µm with relatively concentrated distribution (Figure 4.2a-b). On the other hand, the QC doped microgels were larger, with mean diameter of 66.3±39.3 µm and more dispersed distribution (Figure 4.2c-d). The NaCl doped microgels turned out to be the smallest, with mean diameter of 15.0±6.22 µm (Figure 4.2i-j). This is potentially due to the viscosity difference of the agarose precursor with the addition of different polyelectrolyte solutions. The higher the viscosity, the larger the microgel size. The microgels demonstrated high physical stability when suspended in diverse mediums. Figure 4.2e-h demonstrated that the PAAm gelling solution minimally affected the average size and distribution of the microgels. Apart from the microgel precursor viscosity, their sizes could also be tuned with agitation parameters of the oil emulsion during gelation, such as stirring speed[191]. To narrow the size distribution, cell strainers, commercially available with various mesh sizes, could be applied to screen particles for desirable ranges. This method is low-cost and has high throughput compared with other approaches such as microfluidics[192].

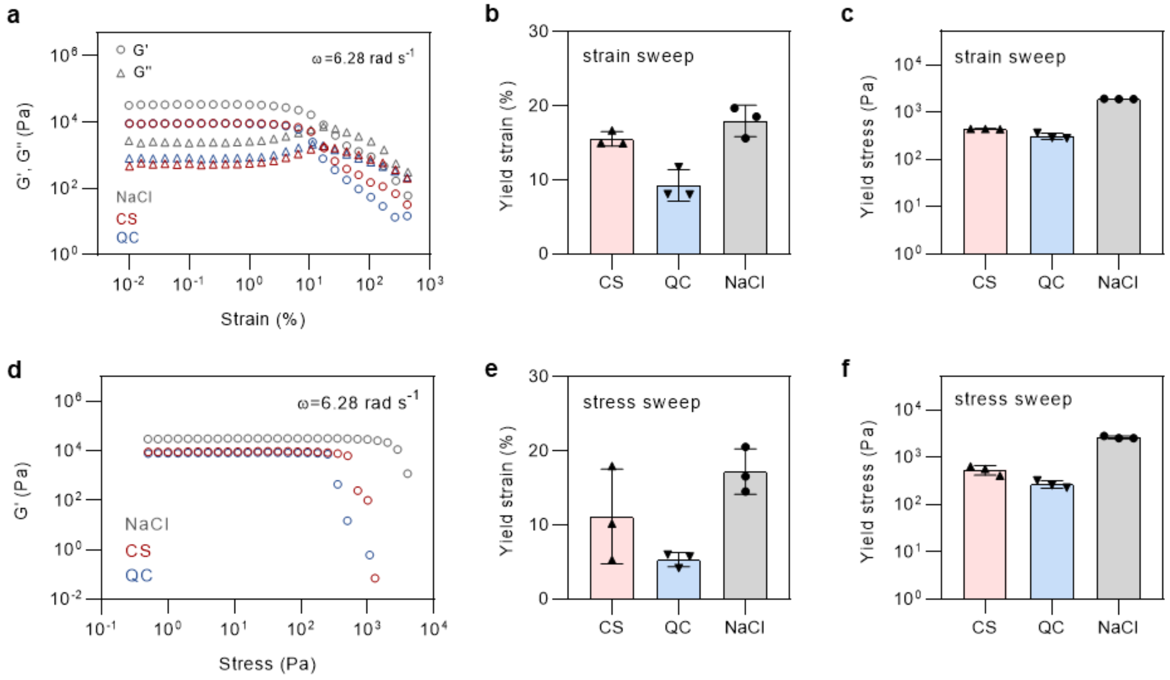

Figure 4.3. Shear yielding characteristics during oscillatory amplitude sweep of the microgel inks. (a) *G'* and *G"* as a function of shear strain. (b) Yield strain and (c) yield stress obtained from the shear strain sweep. (d) *G'* as a function of shear stress. (e) Yield strain and (e) yield stress obtained from the shear stress sweep. The yielding points are determined by the points where *G'* and *G"* intersect. Unless otherwise stated, rheological measurements were performed at angular frequency $\omega = 6.28$ rad s^{-1} for agarose microgels with CS (9 wt.%), or QC (5 wt.%), or NaCl (3 M). Scatter plots are presented from representative data. Data are expressed as the mean ± SD from n = 4 samples.

4.2 Printing Quality

To establish the 3D IMP method and investigate the printing quality, printability of the microgel inks, shape fidelity of the printed structures, and printing resolution were characterized.

4.2.1 Printability

Printability of the ionic microgel inks were characterized using rheology. Successful printing of the ionic microgel inks involves three key processes: extrusion of the microgel ink from the nozzle, a liquid-to-solid transition after extrusion, and a steady solid state after the transition. To ensure smooth implementation of the three processes, the microgel inks are required to possess three corresponding properties: shear thinning and shear yielding behavior, self-recovery ability, and proper yield strength.

Extrusion of the microgel inks was initiated by an external pressure exerted onto a piston that pushes the bulk of the ink contained in a cartridge. The external pressure source was chosen to be pneumatically controlled in this study due to its ubiquity in commercial bioprinters. Under static states, the inks appeared to have high viscosity and behaved like a solid, where *G'* is larger than *G"* (Figure 4.3a). As the external pressure exerted shear stress onto the jammed microgel inks, the granular materials yielded and showed liquid-like behavior, where *G"* was larger than *G'*. This shear yielding characteristic could be ascribed to the phase transitioning of the microgels inks when energy was input into the granular material system, forcing the grain assemblies to be out of thermodynamic equilibrium. Once the extrusion was initiated, the ink started to flow, and the shear rate was increased. Figure 4.4 shows the effect of increased shear rate to the complex viscosities of the microgel inks during oscillatory shear frequency sweep. As the oscillatory shear rate increased, the viscosities of all three microgel inks decreased, showing shear-thinning behavior. The decreased viscosities ensured continuous microgel ink flow during extrusion.

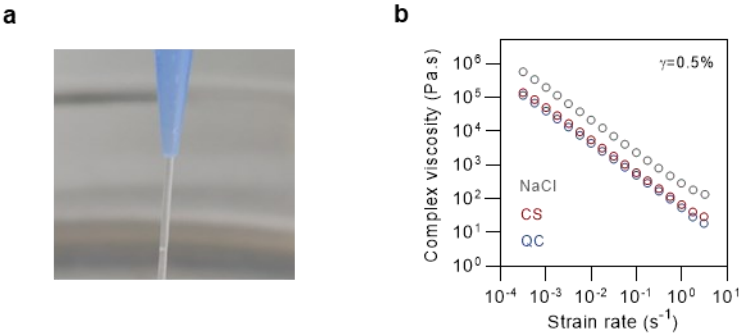

Figure 4.4. Shear thinning characteristics of the microgel inks during extrusion. (a) Digital image of the microgel ink during extrusion. (b) Representative complex viscosity as a function of shear rate at shear strain $\gamma = 0.5\%$ at angular frequency $\omega = 6.28$ rad s^{-1} for agarose microgels with CS (9 wt.%), or QC (5 wt.%), or NaCl (3 M).

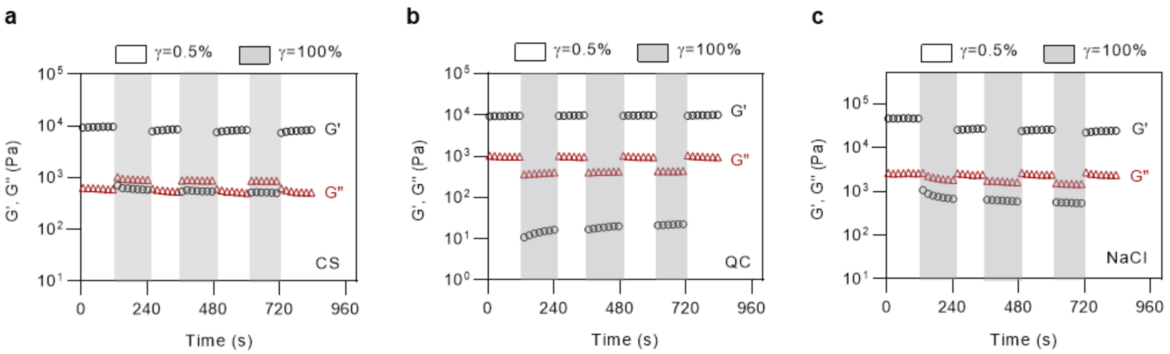

Figure 4.5. Self-recovery characteristics for the microgel inks. *G'* and *G"* through high shear strain (γ = 100%) to low shear strain (γ = 0.5%) isothermal time sweep cycles at angular frequency ω = 6.28 rad s^{-1} for agarose microgels with (a) CS (9 wt.%), (b) QC (5 wt.%), and (c) NaCl (3 M). Scatter plots are presented from representative data.

After extrusion, the microgel inks are expected to rapidly transition from liquid to solid states so as to stabilize at predefined location. To investigate this phenomenon, cyclic isothermal time sweep of high shear strain (100%) and low shear strain (0.5%) was applied to the inks. All microgel inks demonstrated repeated moduli recovery from a liquid state at a high shear strain to a solid state at a low shear strain (Figure 4.5). For deposited microgels to maintain the 3D architectures, the inks should possess high enough yield strain and yield stress. Figure 4.3b-c, plotted the yielding point of the microgels obtained from oscillatory strain sweep tests. Specifically, the critical shear strains for CS, QC, and NaCl inks are 15%, 9%, and 18%, and correspond to shear stresses of 440 Pa, 309 Pa, and 1901 Pa, respectively. This yielding behavior is also seen in oscillatory stress sweep tests, where *G'* of all inks drastically drop at the respective yielding points (Figure 4.3d-f). Note that the yielding points were also not two high (yield strain <100%, yield stress <5 kPa) to hinder the initiation of ink extrusion that might cause clogging of the nozzles. In addition, all above mechanical behaviors of the inks are insensitive to inclusions such as PAAm gelling solutions (Figure 4.6), which further confirmed the compatibility of ionic microgels with the DN crosslinking method. The combination of shear-thinning, shear yielding, and self-recovery properties promises the printability of the 3D IMP strategy.

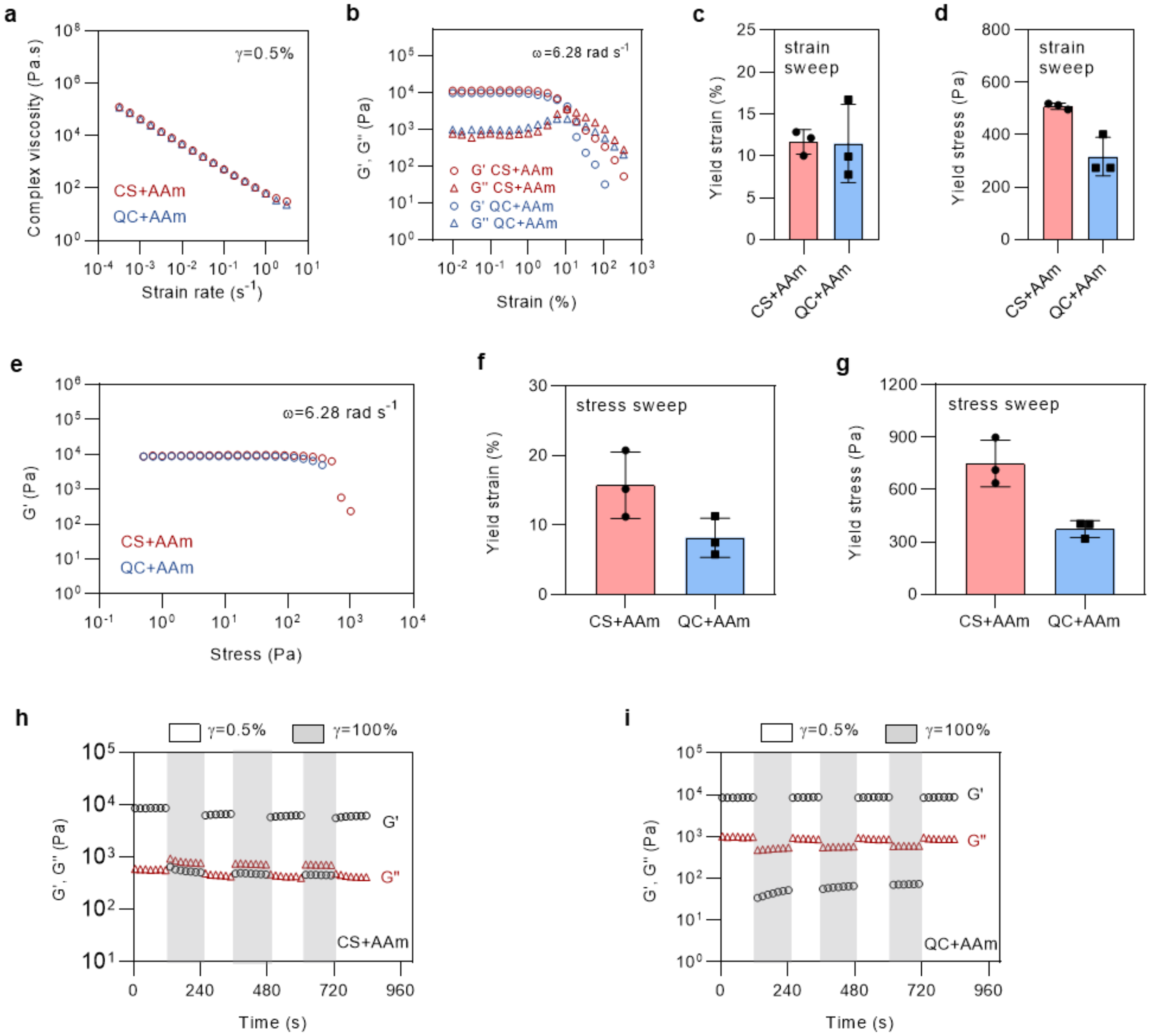

Figure 4.6. Rheological characterization of microgel ink after infiltration of PAAm gelling solution, including AAm monomer, PEGDA crosslinker, and I2959 photoinitiator. (a) Complex viscosity as a function of shear rate. (b) *G'* and *G"* as a function of shear strain. (c) Yield strain, and (d) yield stress at shear yielding point obtained from strain sweep test for agarose microgels with CS (9 wt.%) or QC (5 wt.%). (e) *G'* as a function of shear stress. (f) Yield strain, and (g) yield stress at shear yielding point obtained from shear sweep test. (h) Self-recovery behavior through high shear ($\gamma = 100\%$) to low shear ($\gamma = 0.5\%$) strain cycles at for agarose microgels with CS (9 wt.%) and (i) QC (5 wt.%). Unless otherwise stated, measurements were performed at angular frequency $\omega = 6.28$ rad s^{-1} and shear strain $\gamma = 0.5\%$. Scatter plots are presented from representative data. Data are expressed as the mean ± SD from n = 4 samples.

4.2.2 Shape fidelity

To evaluate the shape fidelity of printed structures, we printed an array of structures with CS (red) and QC (blue) microgel inks. As shown in Figure 4.7a-d, the printed shapes highly resembled the CAD models, showcasing the high fidelity offered by the 3D IMP method. Serpentine and spiral structures are continuous and uniform in width and height, and the gaps between heterogeneous inks were distinct, showing neither under- nor over-printing issues (Figure 4.7a-b). The sharp turning corners of the serpentine structure and the smooth circles of the spiral structure manifested the high printing quality. An ionic diode in a double trapezoidal shape is made with a precisely defined contact junction (Figure 4.7c). The narrowing width of the ionic junction design (down to 1 mm) could intensify the potential drop across the junction and enhance the diode effect[29,193].

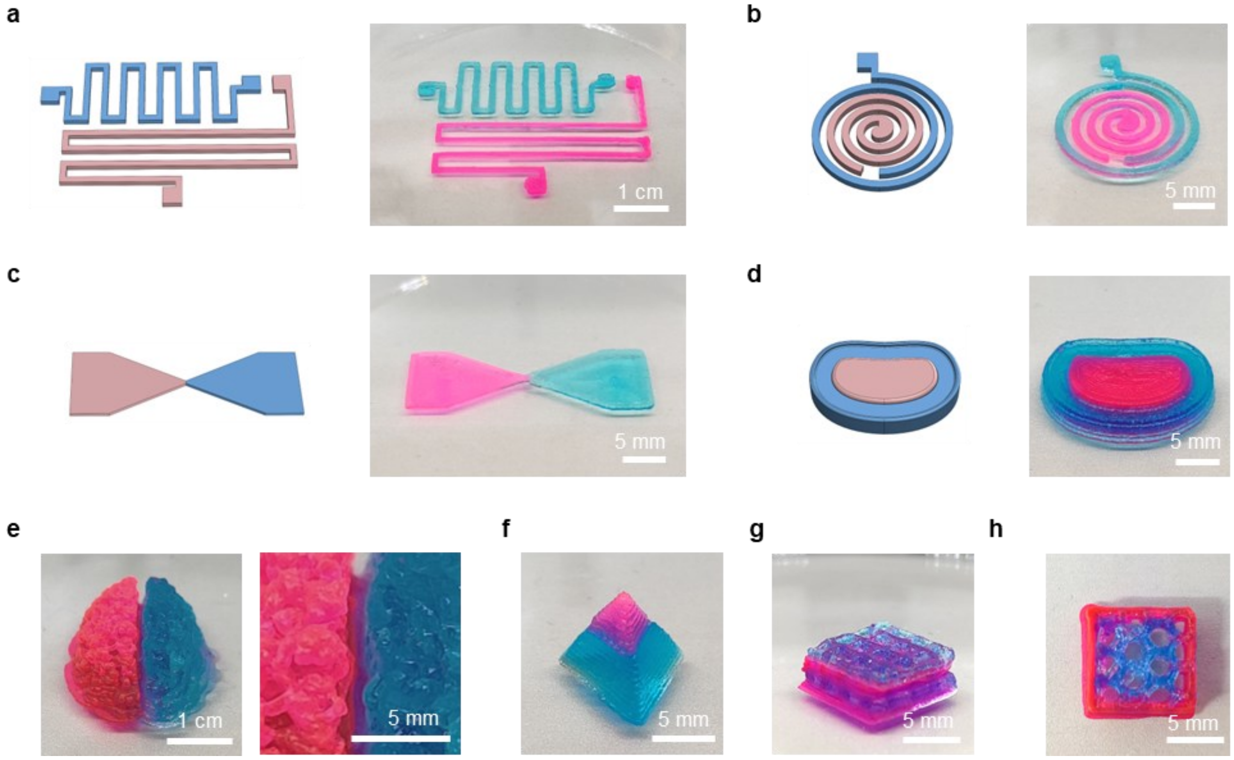

Figure 4.7. Shape fidelity characteristics of the printed structures by 3D IMP. All structures were printed in one run with two materials, with p-type in red and n-type in blue. CAD model and digital images of (a) planar serpentine circuit, (b) spiral circuit, (c) trapezoidal-shaped ionic junction, (d) intervertebral disc, (e) miniature brain, (f) pyramid, (g) alternating grid, and (h) honeycomb cube.

Besides these planar structures, a variety of 3D structures were successfully fabricated, including an IVD model with outer annulus fibrosis and inner nucleus pulposus, a miniature brain, a pyramid with different tip materials, a block with alternating grid layers, and a cube with internal hive structures (Figure 4.7d-h). The high printing fidelity is especially evidenced with the miniature brain, printed layer-by-layer with two hemispheres using different inks (Figure 4.8). The brain displays a thin but distinct gap between two hemispheres and detailed cerebral cortex features.

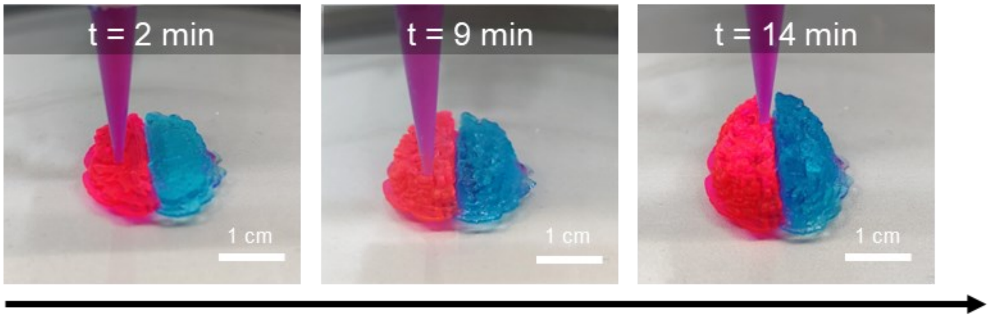

Figure 4.8. Digital image of the 3D IMP process. Microgel inks were deposited layer-by-layer to print the miniature human brain structure, with p-type in red and n-type in blue. deposited

4.2.3 Printing resolution

In this study, the printing resolution was affected by three factors: the nozzle size, the printing pressure, and ink write speed. To calibrate the printing resolution, short filaments of length 1 cm were printed on glass substrates and line width were measured as a function of the above three parameters. These results were displayed in Figure 4.9. For both CS and QC microgel inks, smaller nozzle size (higher gauge number), lower printing pressure, and higher ink write speed resulted in thinner filaments, thus higher printing resolution. CS inks generally exhibited higher resolution compared to QC inks at the same printing pressure and speed, due to the smaller microgel sizes and slightly higher apparent viscosity.

Despite the detailed guidelines provided by this study, there are two key points to be aware of during the resolution optimization process. Frist, microgel sizes need to be considered when selecting nozzles. Microgels of diameter close to half the inner diameter of the nozzle tend to clog the nozzle and paralyze the extrusion process. This issue could be resolved by stepwise screening, producing microgels of limited maximum sizes according to the printing resolution requirements.

Second, excessive printing speed or insufficient pressure might give rise to discontinued filaments, resulting in under-printing issues that could compromise the devices' functions. Conversely, excess pressure or inadequate speed might cause over-printing problems, where deposited materials would be excessively compressed in the in-plane direction. With these two potential problems taken into consideration, extrusion pressures and writing speeds that produce line width close to the nozzle inner diameter is preferred to prevent the abovementioned issues.

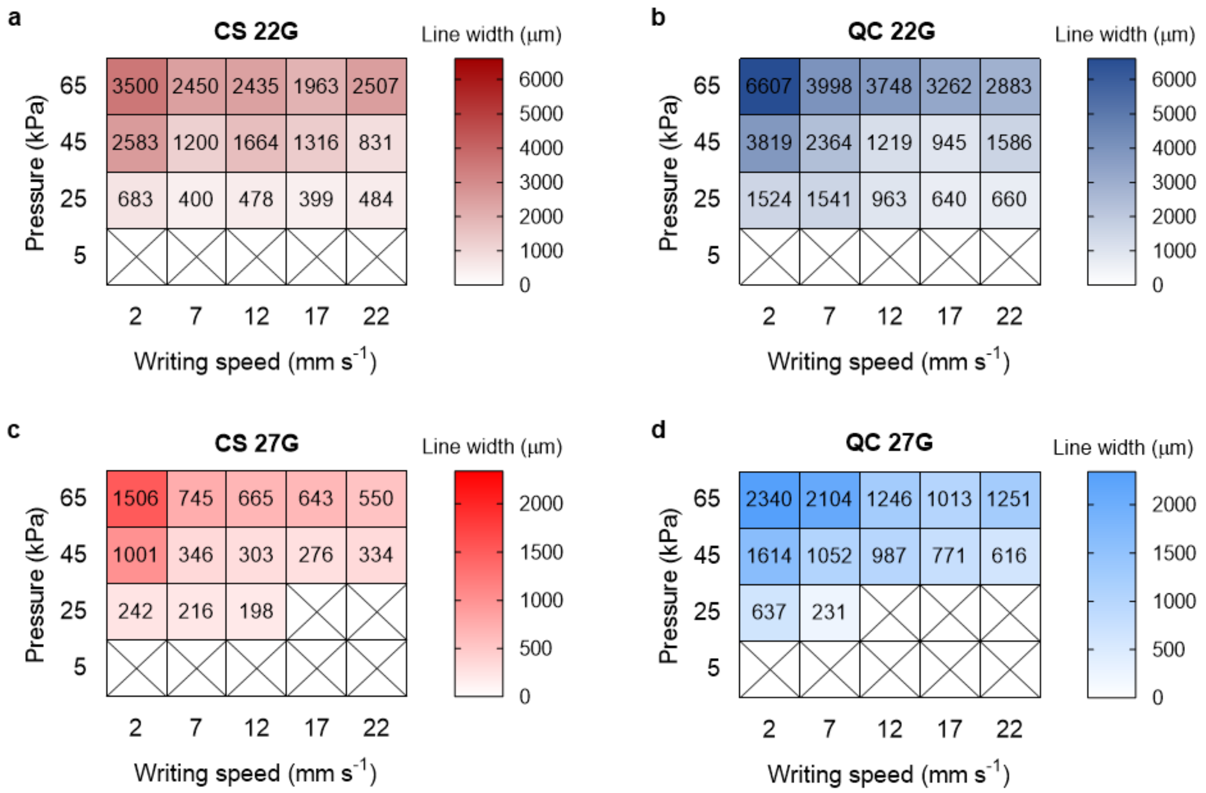

Figure 4.9. Printing resolution characterization of the microgel inks. Printed line width as a function of pressure and ink write speed with 22G nozzle for (a) CS and (b) QC microgel inks, as well as with 27G nozzle for (c) CS and (b) QC microgel inks. "X" represents failure of microgel ink extrusion. Data are expressed as the mean ± SD from n = 6 samples.

4.3 Electrical properties

In this section, with the developed 3D IMP method, the electrical properties of the printed devices were investigated. Two fundamental ionotronic elements were chosen to be studied. First, a classical ionic conductive conductor was constructed, and its electromechanical coupling effect was examined. Next, an ionic junction with asymmetrical current conductivity was investigated. Its current rectification performances, affecting factors, optimizations, and functional principles were studied in detail.

4.3.1 Ionic conductors

The ionic conductor was 3D-printed with ionic microgels containing 3M NaCl. The ionic conductivity of the ionic conductor was calculated from the electrical resistance value measured at 1 kHz frequency alternating current (AC). To compare, the conductivities for printed p-type (9% CS) and n-type (5% QC) ionic conductors were calculated from the mean value of fitted bulk resistance from electrochemical impedance spectroscopy (EIS). The results were displayed in Figure 4.10a. The conductivity of the ionic conductor was 2 S m^{-1}, much higher than that of the p-type (0.406 S m^{-1}) and n-type (0.147 S m^{-1}) hydrogels. The values were all in the reported range of hydrogel-based ionic conductors[194–196]. The superior ionic conductivity of the printed ionic conductor is due to the high mobile ion concentration.

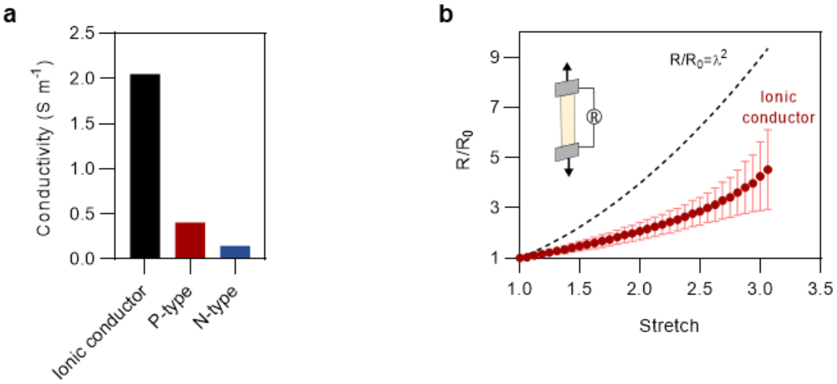

Figure 4.10. Characterizations of the printed elastic ionic conductor. (a) Comparison of the ionic conductivities of the printed ionic conductor to printed p- and n-type hydrogels. (b) Characterizations of the electromechanical coupling behavior of the printed ionic conductor. Dash line shows the theoretical relationship for a non-compressible elastic conductor. Data are expressed as the mean ± SD from n = 3 samples.

To examine the performance of the printed ionic conductor as a classical elastic conductor, the electromechanical coupling behavior was characterized. As shown in Figure 4.10b, as the printed ionic conductor was unidirectionally stretched to λ times its initial length, the normalized electrical resistance (R/R_0) increased nonlinearly with stretch. Theoretically, ionic conductors generally exhibit constant conductivity during deformation. For non-compressible materials, the change in electrical resistance can mainly be ascribed to the geometry change and should follow the relationship: $R/R_0 = \lambda^2$. Experimentally, our results did not fully follow the theoretical scaling, where the increase of the normalized resistance increased slower than theoretical prediction. This was mostly likely due to the ionic microgel printing process, producing materials that are physically porous.

4.3.2 Ionic junctions

An ionic junction was formed with p-type (negatively charged polyelectrolyte) and n-type (positively charged polyelectrolyte) hydrogels. As shown in Figure 4.11a, when the p- and n-type units contact, mobile counterions equilibrate at the vicinity of their respective fixed polyelectrolytes to maintain local charge balance[197,198]. At the heterojunction interface, entropy drives mobile ions to migrate to the opposite sides of the junction. Whereas attribute to the locally unbalanced charges, the fixed polyelectrolytes exert an internal electrical field directed from n-type to p-type, propelling cations to drift back to the p-type side and anions back to the n-type side. Balancing of the two ion flows at equilibrium leads to the formation of an ion-depleted ionic double layer (IDL) forms at the heterojunction interface. The thickness of the ion-depletion layer is mainly affected by polyelectrolyte concentration, device geometry, and external electric field[197,199,200]. The IDL reinforces the asymmetrical ion distribution and regulates ion flow under external electric fields. Consequently, ionic junctions exhibit current rectification behavior similar to silicon diodes, where currents are preferentially conducted from p-type to n-type while inhibited in the opposite direction (Figure 4.11b).

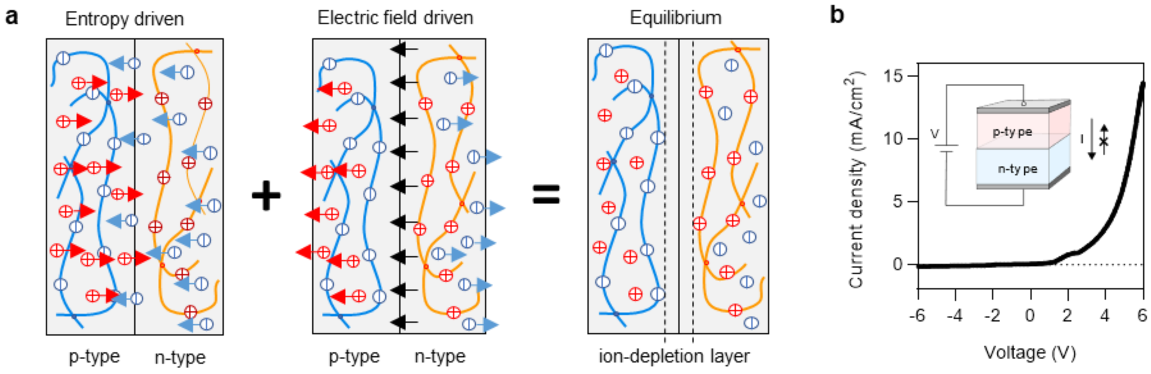

Figure 4.11. The formation and basic function of the ionic junction. (a) Schematic illustration of the formation of the ion-depletion layer at the interface of the ionic junction formed by contacting a p-type and a n-type hydrogels. The equilibrium state can be reached under the combined effect of entropy and electric field. (b) Characteristic of the ionic junction showing current rectification behavior similar to silicon diodes.

4.3.3 Current rectification

To benchmark the electrical performance of the ionic junctions, ionic diodes in the form of one single ionic junction was investigated. The ionic diode was sandwiched between two microporous carbon electrodes and encapsulated in spacers (Figure 4.12). Carbon electrodes with micro-porous layer were used to increase the capacitance of the EDL at hydrogel-electrode interfaces and thus concentrate the potential drop at the ionic junction with a low-capacitance IDL[199]. Linear sweep voltammetry was implemented on the ionic diodes. The applied voltage (from -6 V to 6 V) was defined as the electrical potential of p-type terminal with respect to that of n-type terminal. A voltage of magnitude 6 V was selected to prevent severe electrochemical reaction at the hydrogel-electrode interfaces. The performances were evaluated by current rectification ratio that is calculated as the current density ratio at positive to negative voltages of the same magnitude.

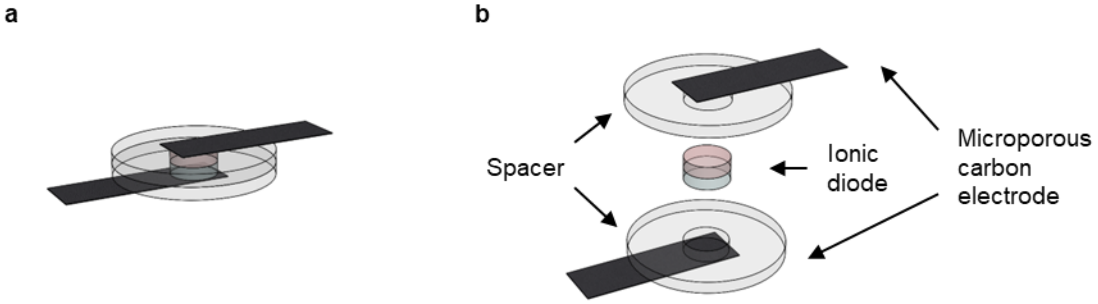

Figure 4.12. Device structure of the ionic diode. (a) Assembled view and (b) exploded view of the ionic diode with microporous carbon electrode.

As expected, both the printed and cast ionic diodes exhibited an asymmetrical current density-voltage (J-V) behavior. At external voltage below the built-in potential of about 2 V, the current densities were low (-0.16 mA cm^{-2} at -6V). While after passing the threshold voltage, current density increases dramatically and reaches 14.4 mA cm^{-2} and power of 86.4 mW cm^{-2} at 6 V(Figure 4.13a,b). The inferior current density of the printed ionic diodes could be attributed to two reasons. First, the washing step of microgels after emulsion removed mobile ions and polyelectrolytes from the system. To confirm this hypothesis, the rectification performance of the cast ionic diodes with or without desalination was compared. Ionic diode consisting of oppositely charged hydrogels that were fabricated by solution casting were desalinated by immersing in reservoir of DI water for 7 hours. As shown in Figure 4.13c-d, desalination decreased the current density magnitude in both forward and reverse biasing regions and caused a 4-time drop in rectification ratio. Second, the rough surfaces of the granular layers decrease the effective contact area at the interface, thus limiting the current magnitude. To validate this theory, cast ionic diode was washed with the same procedure as the ionic microgels. This eliminated the effect of washing steps to the two fabrication methods, leaving the rough surface from the printed ionic diodes as the only difference. Their rectification performances were compared in Figure 4.13e-f. Though slight lower current density and rectification could be observed for the printed ionic diodes, their difference displayed no significant difference. To avoid the washing step, a remedy could be using extrusion fragmentation to fabricate the ionic microgels[192,201].

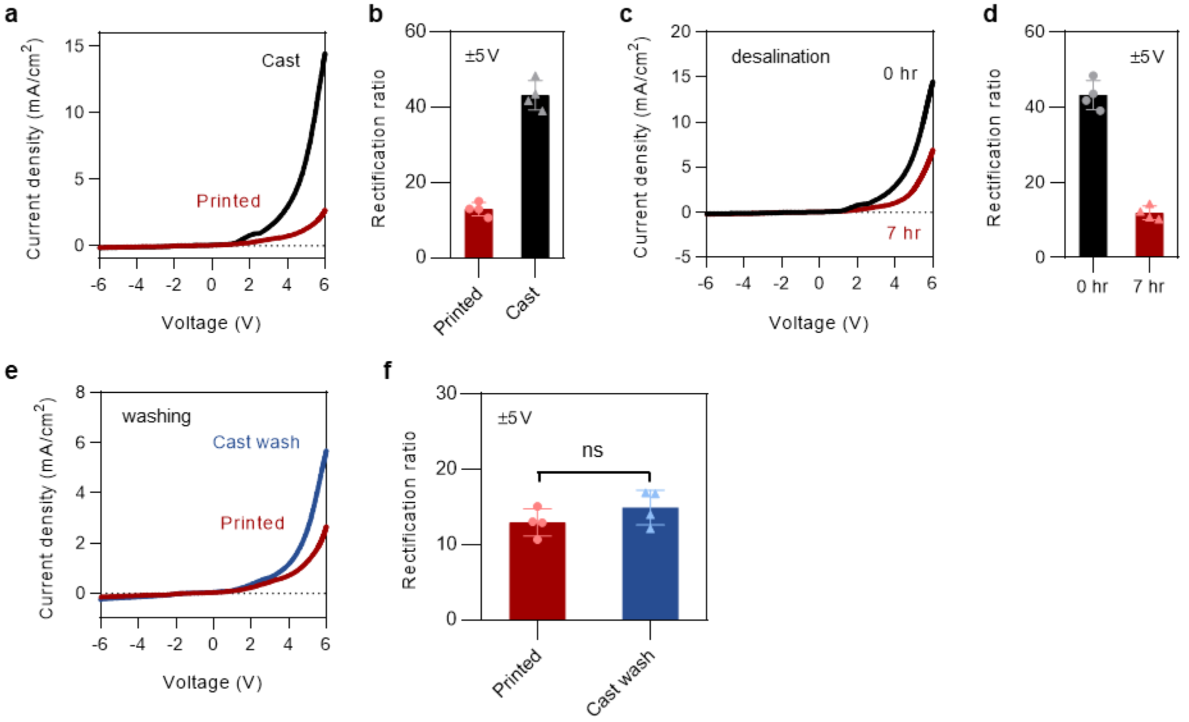

Figure 4.13. Effect of different fabrication methods on current rectification behavior of ionic diodes. Current density as a function of biasing voltage and corresponding rectification ratio at ±5 V for (a, b) cast and 3D printed ionic diodes, (c, d) pristine and desalinated cast ionic diodes, and (e, f) printed and cast ionic diode that went through the same washing procedures. Scatter plots are presented from representative data.

Data are expressed as the mean ± SD from n = 4 samples. Statistical significance is analyzed from Student's t-test (ns: P≥0.05).

Next, to confirm that the diode effect stems from the interface of oppositely charged hydrogels, the ionic diodes with hydrogels containing the same charges on both sides, hydrogels without doped polyelectrolytes, and those with only one charged side were compared. Whereas hydrogels of two sides with the same charges or with one neutral side showed symmetrical J-V characteristics and rectification ratios of around unity, the CS/QC ionic diode displays a rectification ratio of 43 at ±5 V (Figure 4.14 a-e). The results highlighted the importance of two oppositely charged hydrogel layers as the constituents in forming the ionic diode.

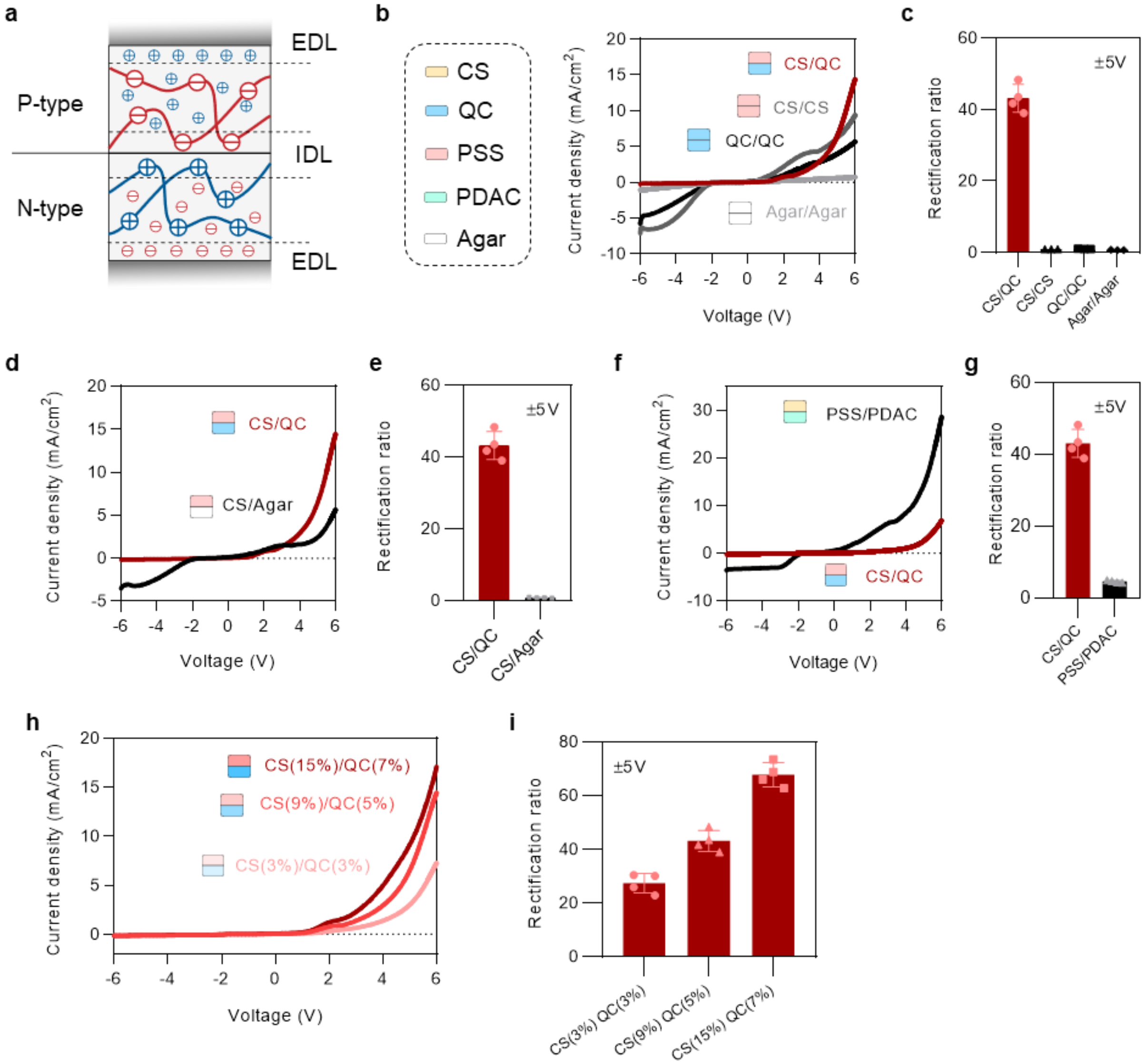

Figure 4.14. Electrical characterizations of ionic diodes. (a) Schematic illustration of the EDL formed at gel-electrode interfaces and IDL formed at the ionic diode interface. Current density as a function of biasing voltage and corresponding rectification ratio at ±5 V for ionic junctions of (b, c) two sides with opposite, same, and no charges, (d, e) two oppositely charged hydrogel diodes and junctions with only one charged side, (f, g) different polyelectrolyte species: CS as p-type and QC as n-type vs. PSS as p-type and PDAC as n-type, and (h, i) varying polyelectrolyte concentrations. Unless otherwise specified, the gel layers are casted with 9 wt. % CS and 5 wt. % QC and a total gel layer thickness of 3 mm and scan rate of 50 mV s^{-1}. Scatter plots are presented from representative data. Data are expressed as the mean ± SD from n = 4 samples.

The current rectification performance could be affected by the polyelectrolyte species, concentration, device thickness, sweep scan rate, and mechanical deformation. First, the highly charged biopolymers CS and QC offered superior performances. As compared in Figure 4.14f-g, the CS/QC diodes show 9 times higher rectification ratio than the PSS/PDAC diodes that were widely used in prior works[25,29]. Next, tuning the polyelectrolyte concentration affected the current rectification. As shown in Figure 4.14i, the rectification ratio increased with the polyelectrolyte concentration. This phenomenon could be understood as follows. As the polyelectrolyte concentrations elevated, reverse leakage currents remained low, due to the increased number of fixed charges that screen mobile counterions as well as protons and hydroxides generated from the hydrolysis of water. On the other hand, forward currents were enhanced due to the increased amount of mobile counter ions brought by the polyelectrolytes (Figure 4.14h). However, further increases of the concentration would undermine the ink processability due to decreased microgel strength. Lastly, the rectification effect can be augmented by reducing the gel thickness to 1 mm (88 at ±5 V) or decreasing the sweep scan rate to 10 mV s^{-1} (123 at ±4.5 V) (Figure 4.15). The results were consistent with previous studies[198,202].

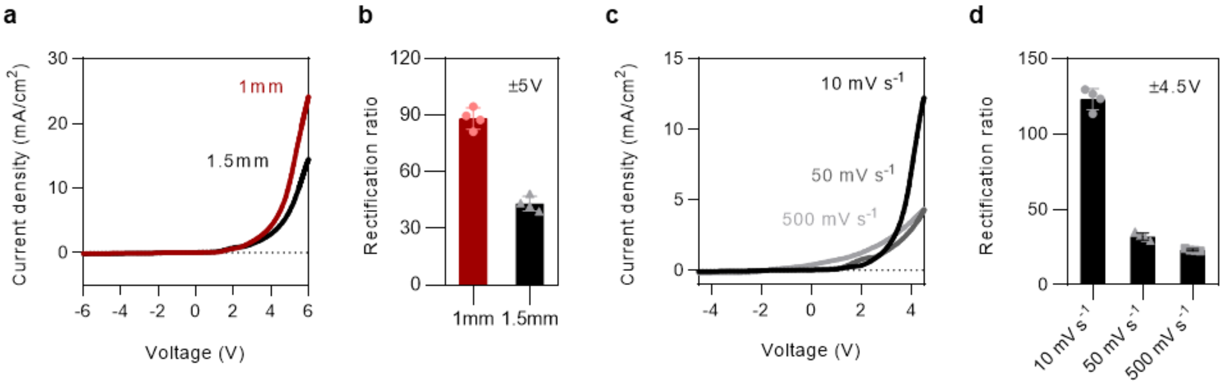

Figure 4.15. Effect of hydrogel layer thickness and sweep scan rate during LSV on current rectification behavior of ionic diodes. (a) Current density as a function of biasing voltage and (b) corresponding rectification ratio at ±5 V for ionic diodes with single layer thickness of 1 mm and 1.5 mm. (c) Current density as a function of biasing voltage and (b) corresponding rectification ratio at ±4.5 V for ionic diodes during LSV with sweep scan rate of 10 mV s^{-1}, 50 mV s^{-1}, and 500 mV s^{-1}. Scatter plots are presented from representative data. Data are expressed as the mean ± SD from n = 4 samples.

Table 4.1. Summary of the material, rectification ratio, and fabrication methods of polyelectrolyte gel diodes.

Material	Polyelectrolytes	Rectification ratio	Fabrication method	Reference
Agar hydrogel	PSS/PDAC	36 @ ±5 V	Casting & manual assembly	202
Ionic polymer in microchip	$PSS/PVBPPh_3$	295 @ ±4 V	Photolithography	203
Agar-CNT hydrogel	PSS/PDAC	9 @ ±5 V	Casting & manual assembly	32
PPy polymer on P(AAm-co-AAc) hydrogel	P(AAm-co-AAc)/PPy	17.2 @ ±2 V	Casting & electrochemical deposition	204
Agar-PAAm hydrogel	PAMPS/ PDMAPAA-Q	47 @ ±5 V	Casting & manual assembly	31
Copolyelectrolyte hydrogel in microchip	PSPA/PDMAPPA-Q	31 @ ±4 V	Laser engraving & lithography	36
PAAm hydrogel	PSS/PDAC	18.5 @ ±4.5 V	Casting & manual assembly	29
Agar-PAAm hydrogel	PSS/PDAC	5 @ ±5 V	Casting & manual assembly	25
Agar hydrogel	pCNC/nCNC	70 @ ±5 V	Casting & manual assembly	28
Ionoelastomer	PES/PAT	50 @ ±0.35 V	Drop-casting	199
Agar-CNT- AgNW hydrogel	PSS/PDAC	13 @ ±5 V	Casting & manual assembly	33
Ionic polymer in microchip	PSS/PDAC	16 @ ±1 V	Photolithography	205

Other effects such as mechanical deformations on the rectification performances of the ionic diodes have been studied extensively and will not be the focus of this thesis[27,29,199,205]. In general, geometry changes induced by stretching will cause variations in the voltage distribution across the gels and interfaces, thus affecting the current rectification performance. The performance of our devices is notably among the highest value reported for polyelectrolyte gel-based diodes (Table 4.1).

4.3.4 Electrochemical rectification mechanism

To investigate the electrochemical rectification mechanism of the ionic junctions, electrochemical impedance spectroscopy (EIS) was conducted, and the impedance data was fitted with equivalent circuit models. Ac-impedance measurements were performed on the CS/QC heterojunction and the homojunctions (CS/CS and QC/QC). Figure 4.16a displays the frequency bode plot with the equivalent circuit in the inset, while Figure 4.16b shows the Nyquist plot for the three types of junctions. The CS/QC heterojunction demonstrated significantly higher impedance and phase angle at low frequency compared to homojunctions, elucidating the formation of the IDL. This is because the IDL is depleted with mobile ions, leading to high bulk resistance (R_B) and low effective capacitance (*C*) from the constant phase element (*CPE*). The corresponding values for the fitting parameters are presented in Table 4.2.

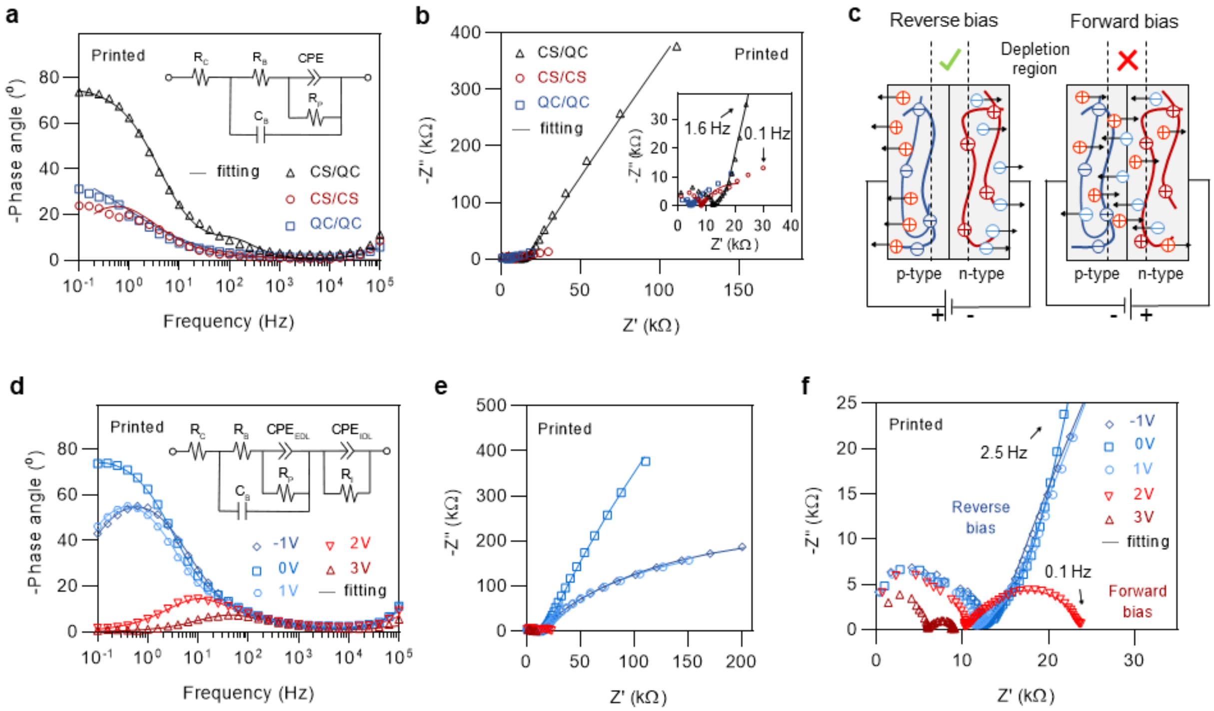

Figure 4.16. Electrochemical characterizations of the printed ionic junction. (a) Bode phase plot and (b) Nyquist plot with enlargement in the low frequency region in the inset for ac-impedance measurements of printed CS/QC heterojunction, and CS/CS, QC/QC homojunctions with fittings to the equivalent circuit

model in the inset. (c) Schematic illustration of the ionic junction under reverse bias and forward bias state. (d) Bode phase plot and (e) Nyquist plot with (f) zoom in view for ac-impedance measurements of the printed CS/QC ionic junction under dc biases with fittings to the equivalent circuit model in the inset. Scatter plots are presented from representative data from n = 3 samples.

In addition, we carried out impedance measurements with direct-current (dc) biases. Increasing the biasing voltage beyond a threshold voltage switches the ionic junction from reverse bias to forward bias regime (Figure 4.16c). The switching of operation states is indicated by the substantial impedance drops and low phase angles at low frequencies (Figure 4.16d-f). In this case, mobile ions start to drift through the depletion region, temporarily paralyzing the IDL. The increase of IDL capacitance causes EDL to allocate more potential drop, where the overpotential exceeds 0.828V and leads to the electrolysis of water at the electrodes[206]. This effect leads to the reduction of R_B, polarization resistance (R_P), and interfacial resistance (R_I) at the IDL, as well as the substantial increase of effective IDL capacitance (C_{IDL}) and decrease of ion depletion layer thickness (δ_{IDL}) (Table 4.3, Table 4.4). Due to the permeated PAAm network that infiltrates into and between ionic microgels, the transmission behavior of electrical signals in ionic microgels is believed to resemble that of the bulk ionic junctions; that is, mobile ions transport in aqueous medium through the polymer network of much larger meshes[18,200,207]. The above electrochemical characteristics can be seen with both printed and cast devices (Figure 4.17, Table 4.5, Table 4.6), The results proved that the printing method minimally affected the functionality of ionic junctions, thus further supported the reliability of the 3D IMP method for ionotronic fabrication.

Table 4.2. Fitting parameters for ac-impedance measurement of printed CS/QC, CS/CS and QC/QC, according to the equivalent circuit model shown in Figure 4.16a.

	R_C (kΩ)	**R_B (kΩ)**	**CPE**		**C_B (nF)**	**R_P (kΩ)**	**C (F cm^{-2}) b)**
			Y0 (s^n Ω^{-1} cm^{-2})	**n**			
CS/QC	12.5	4.83	3.52×10^{-6}	0.842	326	4.85×10^{4}	6.77×10^{-6}
CS/CS	7.95	0.304	3.24×10^{-5}	0.690	805	25.7	1.68×10^{-5}
QC/QC	3.40	0.842	7.38×10^{-5}	0.620	4.18	44.4	5.54×10^{-5}

a) Impedance of CPE is calculated as $Z_{CPE} = Q_0^{-1}(j\omega)^{-n}$, where Q_0 is a constant, n is a constant ranging from 0 to 1, ω is angular frequency, and j is imaginary number; b) Effective capacitance of IDL (C_{IDL}) and EDL (C_{EDL}) are calculated according to Brug model[208] as $C = Q^{1/n} R_B^{(1/n-1)}$, where C is the effective capacitance, R_B is the bulk resistance, Q and n are constants in CPE.

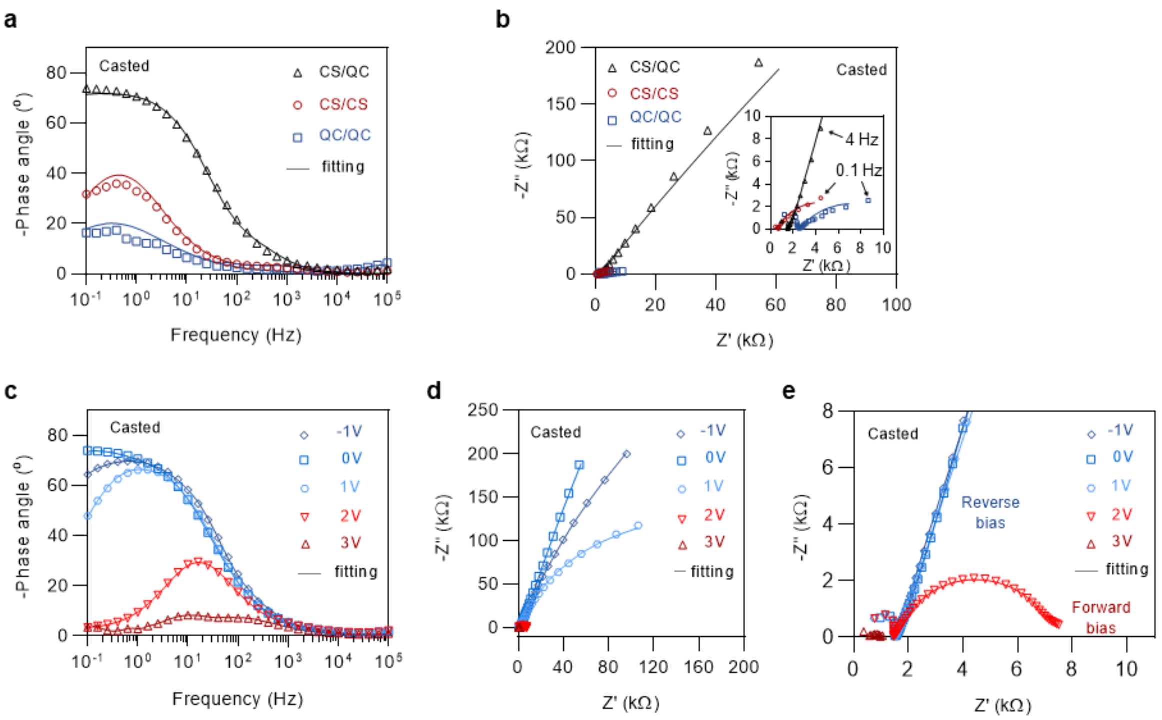

Figure 4.17. Electrochemical impedance spectroscopy results for cast ionic junctions. (a) Bode phase plot and (b) Nyquist plot for ac-impedance measurements of cast CS/QC heterojunction, and CS/CS, QC/QC homojunctions. Inset shows an enlargement in the low frequency region. (c) Bode phase plot and (d) Nyquist plot with (e) enlargement in the low frequency region for ac-impedance measurements of the cast ionic junction under dc biases. Scatter plots are presented from representative data from n = 3 samples.

Table 4.3. Fitting parameters for ac-impedance measurement of printed CS/QC junction under dc bias, according to the equivalent circuit model shown in Figure 4.16d.

dc bias	R_C (kΩ)	R_B (kΩ)	CPE_{EDL}		C_B (nF)	CPE_{IDL}		R_P (kΩ)	R_I (kΩ)
			Y_{EDL} ($s^n\ \Omega^{-1}\ cm^{-2}$)	n_{EDL}		Y_{IDL} ($s^n\ \Omega^{-1}\ cm^{-2}$)	n_{IDL}		
-1 V	5.17	2.27	3.88×10^{-6}	0.771	206	8.74×10^{-11}	0.986	571	7.28
0 V	6.82	5.38	9.11×10^{-6}	0.546	0.117	3.77×10^{-6}	0.883	6.67	7.99×10^{3}
1 V	5.17	4.63	5.22×10^{-6}	0.790	447	1.19×10^{-9}	0.800	499	6.82
2 V	5.17	1.40	5.02×10^{-6}	0.738	245	1.28×10^{-9}	0.800	12.1	5.33
3 V	5.17	0.776	6.31×10^{-6}	0.800	1.31	4.51×10^{-6}	0.761	2.488	0.570

Table 4.4. Effective capacitance and thicknesses of the IDL and EDL for the printed ionic junctions

dc bias	**C_{IDL} [F cm^{-2}]**	**δ_{IDL} [µm] [a)]**	**C_{EDL} [F cm^{-2}]**	**δ_{EDL} [nm]**
-1 V	3.0×10^{-9}	23	3.9×10^{-6}	17
0 V	3.7×10^{-9}	18	3.1×10^{-6}	23
1 V	4.2×10^{-9}	16	8.0×10^{-6}	8.7
2 V	3.4×10^{-9}	20	3.6×10^{-6}	19
3 V	1.5×10^{-7}	1.7	1.2×10^{-4}	0.57

[a)] Thickness (δ) is calculated according to Gouy-Chapman[209] model as $\delta = \varepsilon_0 \varepsilon_r A C^{-1}$, where ε_0 is the vacuum dielectric permittivity, ε_r is the relative dielectric permittivity, A is the contact area of the two oppositely charged gels, and C is the effective capacitance.

Table 4.5. Fitting parameters for ac-impedance measurement of cast CS/QC, CS/CS and QC/QC according to the equivalent circuit model shown in Figure 4.16da.

	R_C (kΩ)	**R_B (kΩ)**	**CPE**		**C_B (nF)**	**R_P (kΩ)**
			Y_0 (s^n Ω^{-1} cm^{-2})	**n**		
CS/QC	1.53	0.680	6.69×10^{-6}	0.798	966	9.06×10^{3}
CS/CS	0.599	0.0721	2.23×10^{-4}	0.730	3.50×10^{3}	7.19
QC/QC	2.24	0.297	1.53×10^{-4}	0.574	6.20	9.25

Table 4.6. Fitting parameters for ac-impedance measurement of cast CS/QC junction under dc bias, according to the equivalent circuit model shown in Figure 4.16d.

dc bias	**R_C (kΩ)**	**R_B (kΩ)**	**CPE_{EDL}**		**C_B (nF)**	**CPE_{IDL}**		**R_P (kΩ)**	**R_I (kΩ)**
			Y_{EDL} (s^n Ω^{-1} cm^{-2})	**n_{EDL}**		**Y_{IDL} (s^n Ω^{-1} cm^{-2})**	**n_{IDL}**		
-1 V	1.53	9.73	4.22×10^{-6}	0.719	2.33×10^{3}	7.25×10^{-6}	0.815	1.73×10^{3}	480
0 V	1.50	51.6	2.95×10^{-6}	0.766	7.16×10^{3}	3.24×10^{-5}	0.606	2.70×10^{3}	8.98×10^{4}
1 V	1.51	0.112	1.79×10^{-5}	0.700	350	1.21×10^{-5}	0.923	411	130
2 V	1.46	0.178	9.94×10^{-6}	0.764	445	3.61×10^{-3}	0.819	5.71	0.729
3 V	0.564	0.192	8.63×10^{-3}	0.670	1.02×10^{5}	3.22×10^{-5}	0.753	0.208	0.210

4.4 Mechanical Properties

Mechanical robustness is of great significance for ionic devices to maintain physical integrity and operate reliably. Hydrogel ionotronics are often designed for applications that involve interaction with the human body. Therefore, to accommodate for potential deformations, devices are expected to be stretchable and tough. In this section, ionic junctions were chosen to be the model ionic device, given that they are composed of more than one ionic component. The stretchability, fracture toughness, and inter-component adhesion was investigated.

4.4.1 Stretchable and tough

The stretchability and fracture toughness of the ionic junction were evaluated by pure shear test. The ionic junctions were fabricated by laminating two layers of oppositely charged hydrogels using either 3D IMP or traditional precursor casting methods. Under pure shear tests, both DN printed and cast unnotched samples were capable to be stretched along their planar direction more than 20 times their initial lengths before rupture. Conversely, the cast SN agarose ionic junctions, which composed of the same material as the agarose microgels, exhibited maximum strain of only 10% (Figure 4.18 a-c). The stretchability of DN ionic junctions well exceeded that of the SN agarose counterpart (Figure 4.18d-e). The results underline the importance of the PAAm network and the microgel-reinforced DN design of our ionic junctions.

The ionic junctions are layered materials and are prone to mixed mold cracking during stretch[210]. To study the fracture behavior and characterize the fracture toughness, we tested notched specimens to measure the critical stretch ratio when the notch starts to extend. By integrating the area under the engineering stress-stretch curve of unnotched specimens up to the critical stretch ratio, we calculated the fracture toughness of the cast and printed junctions to be 3431 J m^{-2} and 1204 J m^{-2}, respectively (Figure 4.18f). No delamination occurs during the whole process, indicating strong adhesion between the two ionic units (Figure 4.18g). While lower than those of cast devices, the fracture toughness and strength of printed devices are more than 100 times that of agarose hydrogels (~3 J m^{-2}). The dramatic toughening mechanism is attributed to the synergy between the covalently crosslinked PAAm network and the energy dissipation of dispersed DN microgels[211].

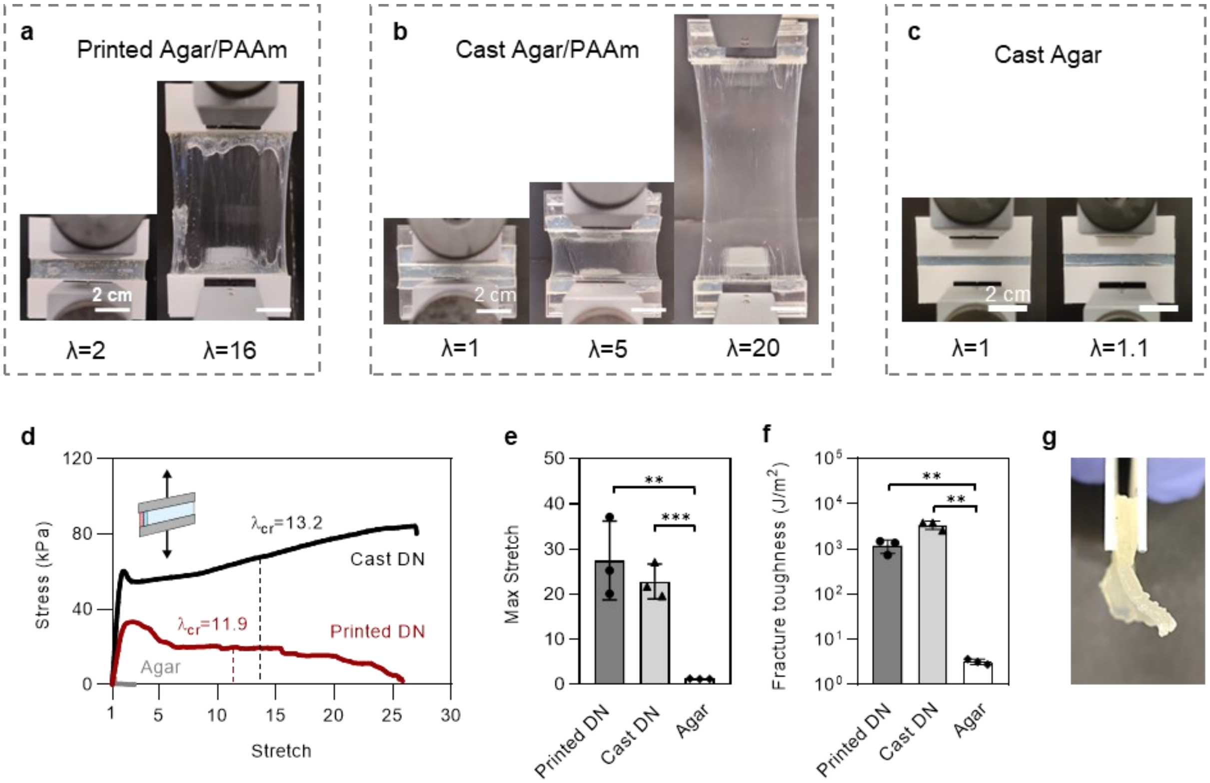

Figure 4.18. Mechanical properties of the ionic junctions. Digital image of unnotched hydrogel samples: (a) printed DN Agar/PAAm, (b) cast DN Agar/PAAm, and (c) cast SN agarose (Agar) ionic junctions during pure shear tests. (d) Representative stress–stretch curves for unnotched samples. Dash lines indicate the critical stretch values obtained from stretching of the notched samples. (e) Maximum stretch and (f) fracture toughness of ionic junctions fabricated with 3D IMP and precursor casting. (g) Digital image of an unnotched printed DN ionic junction after rupture in pure shear tests. The cross-sectional view indicates two layers of the ionic junction rupture at the same location without any delamination. Data are expressed as the mean ± SD from n = 4 samples. Statistical significance is analyzed from Student's t-test (**: $P<0.01$, ***: $P<0.001$).

4.4.2 Cohesion

As the ionic junctions are heterogenous, the adhesion between different units is important for their performance. T-peeling tests were performed, as illustrated in Figure 4.19a, to characterize the adhesion performances between two ionic units. The adhesion energy values are calculated from two times the plateau value of the force/width versus displacement data (Figure 4.19b). The values are shown in Figure 4.19c. Remarkably, the printed ionic junctions display an adhesion energy of 579 J m^{-2}, 3 times higher than the cast counterpart (144 J m^{-2}) and 100 times higher than SN agarose junctions (6.5 J m^{-2}). The enhanced adhesion performance is ascribed to the mechanical interlocking of microgels between adjacent layers. While the cast hydrogel ionic junctions exhibited smooth interfaces between p- and n-type layers, the ones printed with ionic microgels possessed rough interfaces (Figure 4.19d-e). This effect is evidenced by the rough fracture surface and the cohesive failure of the printed ionic junctions, where the crack kinks into the bulk of the hydrogel (Figure 4.19a). The excellent mechanical properties of the ionic junctions assure their physical integrity and reliability in practical applications.

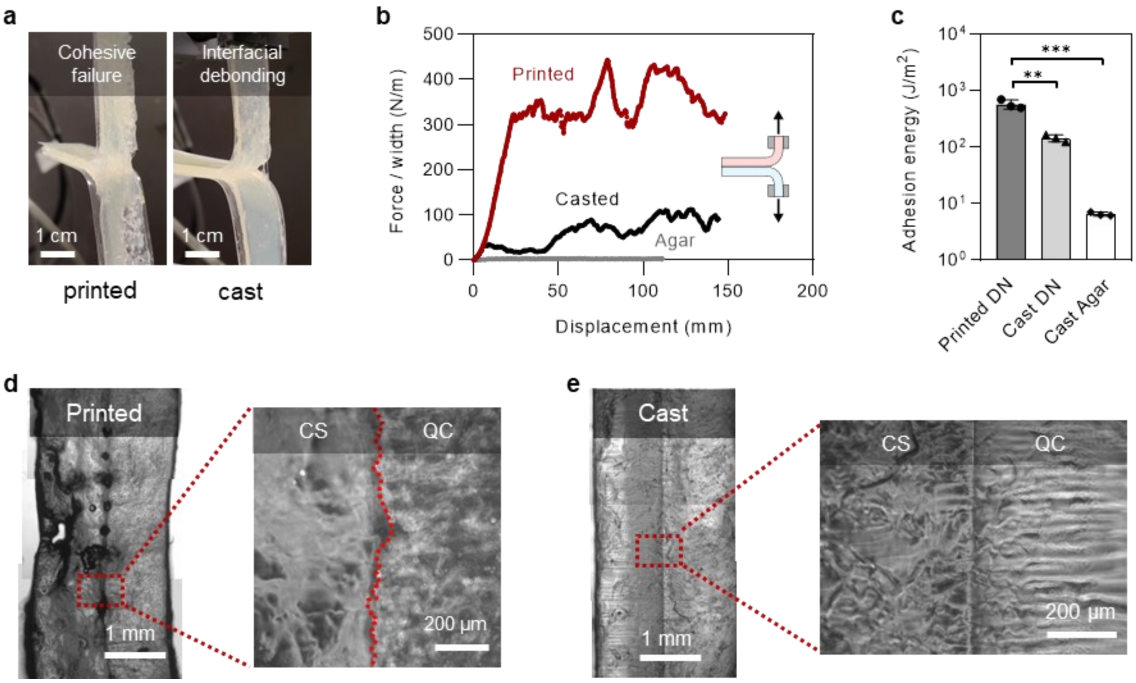

Figure 4.19. Cohesive properties of the ionic junction. (a) Digital images, (b) representative force/width - displacement curves, and (c) corresponding adhesion energy for T-peeling tests of two layers of ionic junctions fabricated with 3D IMP or precursor casting. (d) Optical microscope images of the printed and (e) cast ionic junction, with CS on the left and QC on the right. Zoom-in views displayed the interfaces between the two layers. Data are expressed as the mean ± SD from n = 4 samples. Statistical significance is analyzed from Student's t-test (**: P<0.01, ***: P<0.001).

4.4.3 Degradation

Ionotronic device that could operate within their lifespan and be degraded afterwards is highly desirable. Degradability was designed to our ionotronic material system and evaluated via an in-vitro degradation test. The material design, macroscopic changes, dry weight loss, and electrical performances of the ionic junction under degradation were presented.

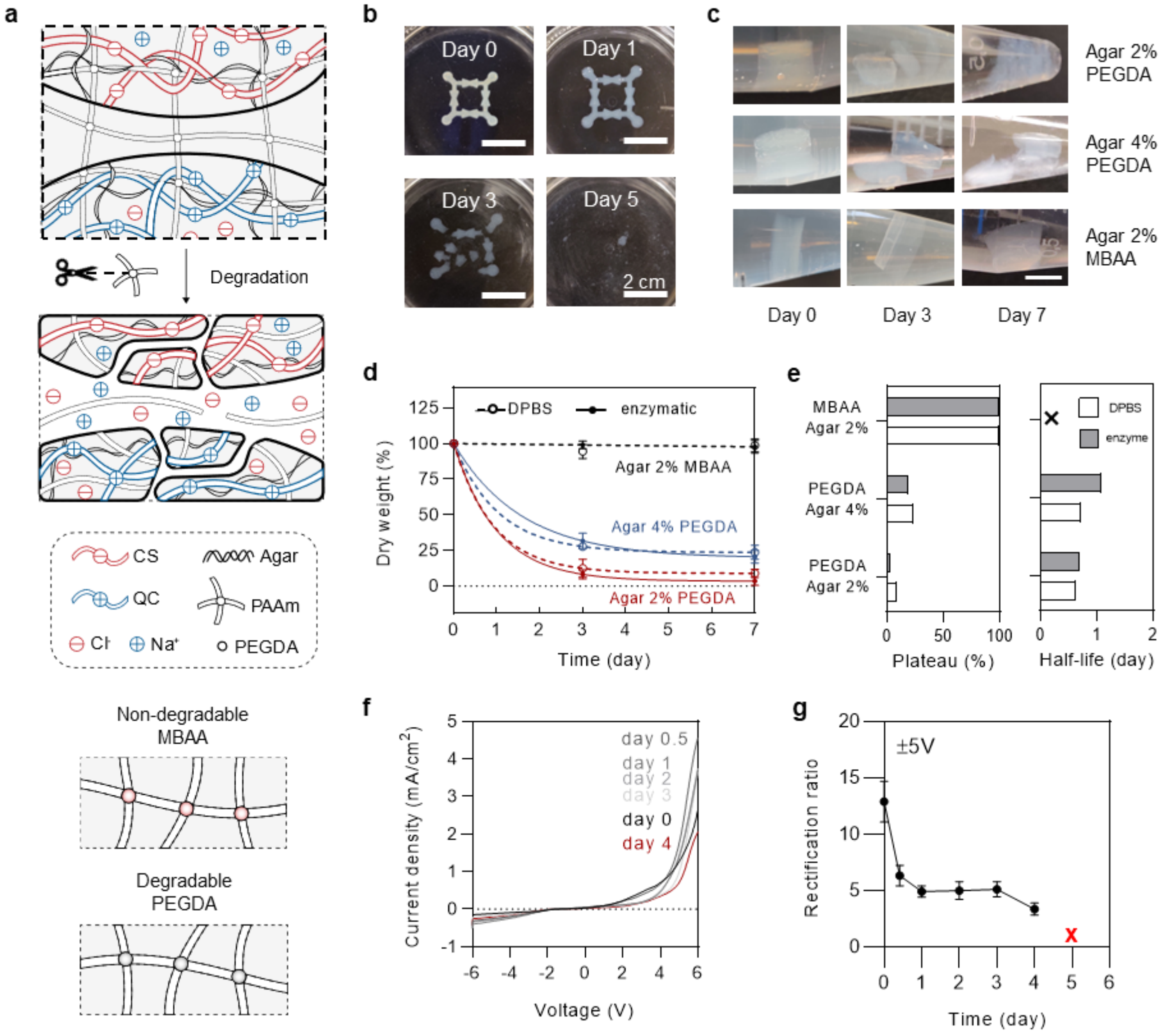

Figure 4.20. Degradation characterizations of the ionic junctions. (a) Schematics of the material design for degradation. (b) Digital image of a printed degradable circuit. (c) Digital image, (d) dry weight change, and (e) corresponding plateau dry weight and half-life time obtained from fitting for in vitro degradation of printed ionic junction in DPBS solutions with or without enzymes. DN hydrogel with MBAA as crosslinker for PAAm network and different concentrations of agarose were included for comparison. Scale bar, 0.3 cm. (f) Electrical performance of the printed ionic junctions during in vitro degradation. Current density as a function of biasing voltage and (g) corresponding current rectification ratio at ±5 V for printed ionic junctions at different degradation time stamps. Scatter plots are presented from representative data. Data are expressed as the mean ± SD from n = 4 samples.

The rational design of the polyelectrolyte and the polymer network is key to degradability and programmed device stability. The biopolymers used – agarose, CS, and QC – are naturally derived and readily degradable enzymatically[212–214]. For the PAAm network, as illustrated in Figure 4.20a, we employ poly(ethylene glycol) (PEGDA) as a degradable crosslinker, which undergoes hydrolysis due to the presence of ester bond[215]. As a result, the devices could disassemble and degrade over time. This property of transient stability was demonstrated in Figure 4.20b, where a 3D ionic microgel printed circuit degraded progressively into small pieces over time. To characterize the degradation behavior of the ionic junctions, we quantify their degradation profile in terms of both physical integrity and electrical performance through an in-vitro degradation test. As comparison, the effect of different degradation media, DPBS with or without enzymes, was studied. To investigate the design of the material system, MBAA as a non-degradable crosslinker for the PAAm network was employed for comparison. Additionally, the effect of agarose concentrations was also studied.

Physically, the ionic junctions composed of 2% and 4% agarose with PEGDA crosslinker disintegrated into small pieces and ultimately led to a 91% and 76% reduction in dry weight after one week without enzymes, respectively (Figure 4.20c-d). When enzymes were introduced to the degradation media, the dry weight loss after 7 days of incubation turned out to be marginally increased, showing 96% and 79% for 2% and 4% agarose, respectively. In stark contrast, when PEGDA was replaced with a non-degradable crosslinker MBAA, neither fragmentation nor dry weight loss after seven days were observed with or without enzymes. To parameterize the degradation profile, a simple one phase decay model was fitted to the data and displayed in Figure 4.20d as solid (enzymatic) or dashed lines (DPBS only). The equation of the model is as follows:

$$m = \left(m_0 - m_{plateau}\right)e^{\left(-\frac{t}{\tau}\right)} + m_{plateau}$$

where m_0 is the initial dry weight at day 0, $m_{plateau}$ is the plateau dry weight, and τ is the time constant. The half-life time ($t_{1/2}$) can be calculated as:

$$t_{1/2} = \ln(2)\,\tau$$

The resulting plateau dry weight and half-life time was compared and plotted in Figure 4.20e. The addition of enzymes imposed slight effect to the degradation profile. It barely affected the final dry weight nor the degradation speed. It is hypothesized that the PAAm network dominated the overall structural integrity and thus the hydrolytic degradation of the PAAm network controlled the general degradation characteristics. The enzymes should also slowly degrade the agarose and biopolymers but demonstrated limited effect in this study.

The electrical performance of the ionic junctions was characterized by linear sweep voltammetry, and rectification ratio at ±5 V was used as the evaluation criterion. The current densities as well as rectification ratio deteriorated substantially within the first day, and then maintained a period of stable operation, until catastrophic fragmentation on day 5 (Figure 4.20g-h). The diminished electrical performance within day 1 was hypothesized to stem from the loss of mobile ions, while complete breakdown of the device on day 5 could be associated with structural failure. The results highlighted our material design in achieving controlled degradation of ionotronic devices.

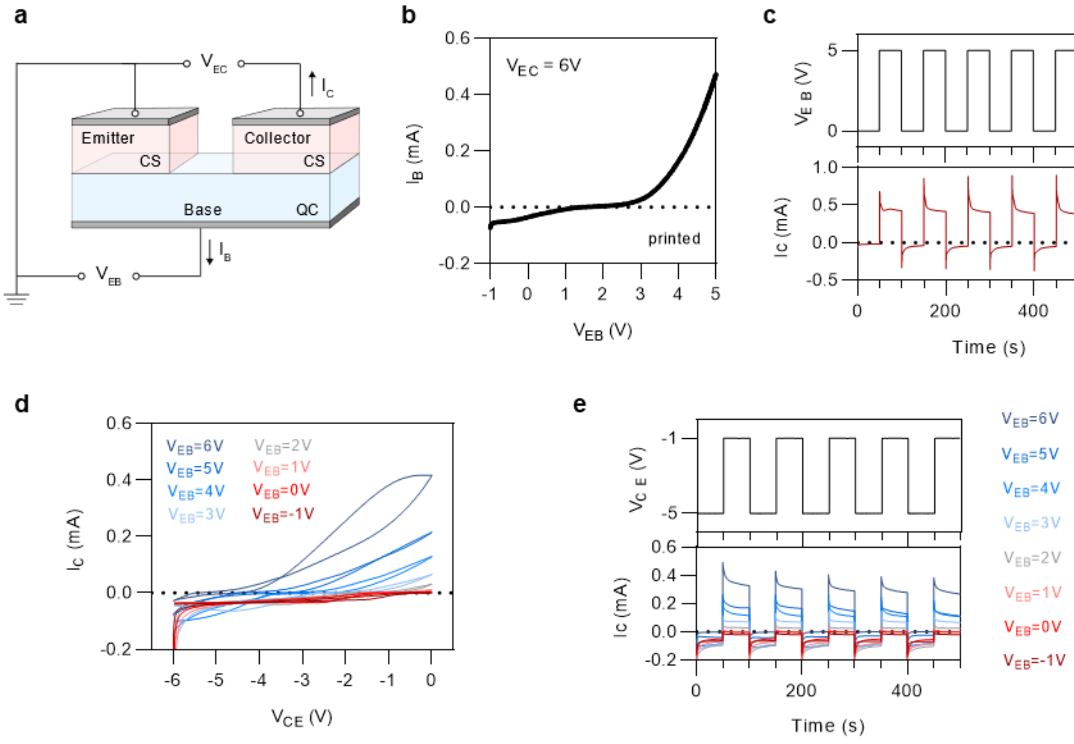

Figure 4.21. Characterizations of the ionic BJT fabricated by 3D IMP. (a) Schematic and circuit diagram of 3D-printed ionic BJT connected in a common-emitter configuration. (b) Base current (I_B) as a function of emitter-base voltage (V_{EB}) at emitter-collector voltage (V_{EC}) of 6 V. Threshold voltage (V_T) is identified as 2 V. (c) Output current (I_C) response as input voltage (V_{EB}) switching between on (5 V) and off (0 V) state at V_{CE} = -1V. (d) Output characteristic (I_C-V_{CE}) curves as a function of input voltage (V_{EB}). (e) Modulation of I_C by V_{EB} as response to switching V_{CE}. Scatter plots are presented from representative data from n = 3 samples.

4.5 Ionotronic devices

The printing capacity of the 3D IMP and the performance of the printed ionic diodes allow us to prototype ionic junctions of various configurations and electrical functions. To prove so, we fabricated and characterized three kinds of ionotronic devices: ionic bipolar junction transistors (BJT), ionic full-wave rectifiers, and ionic touchpads. The electrical counterpart of ionic transistor is extensively used to amplify and modulate signals, and that of ionic rectifier converts ac to dc signals. The ionic touchpad is promising for wearable devices due to its stretchability and conformity to skin. These devices can reveal the capacity of the 3D IMP method in fabricating ionotronic devices with more than two ionic units.

4.5.1 Ionic bipolar junction transistor

The ionic BJT takes a common emitter configuration with three ionic units: one n-type gel as base and two p-type gels as emitter and collector (Figure 4.21a). Two ionic junctions were formed in this way, namely, the emitter-base (EB) junction and the collector-base (CB) junction. The ionic BJT regulates the current from the collector (I_C) via the emitter-base voltage (V_{EB}). A current is expected between the emitter and the collector only when V_{EB} exceeds a threshold voltage (V_T). To test this characteristic, we swept V_{EB} from -1 V to 5 V, while setting the emitter-collector voltage $V_{EC} = 6$ V. As expected, the measured current from the base I_B remains small (<0.05 mA) until V_{EB} reaches $V_T = 2$ V , and the device switches from cut-off to active mode and achieves 0.5 mA at 5 V (Figure 4.21b). The distinct current contrast at the two operating modes was also confirmed by on-off switching of V_{EB}. In this test, the V_{EB} was alternated between on (5 V) and off (0 V) voltages, while fixing V_{CE} and monitoring I_C. Figure 4.21c showed that large currents (~0.5 mA) are reached repeatably at the active mode and decrease quickly to a low level (< 0.04 mA) at the cut-off mode. Upon switching, the current spikes and gradually drops to an equilibrium level, consistent with the behaviors of bipolar membrane ionic transistors[216].

To further test the current modulation performance of the ionic BJT, we measured the I_C-V_{CE} responses to varying constant V_{EB}. Cyclic voltammetry was performed at V_{CE} between -6 V and 0 V (Figure 4.21d). When $V_{EB} < V_T$, both the EB and CB junctions were under reverse bias state, and the ionic BJT was in cut-off mode. The mobile ions were depleted from the junction interfaces, leading to low I_C level no matter how V_{CE} was swept. When $V_{EB} > V_T$, the EB junction becomes forward biased, enriching mobile ions at the EB and CB interfaces. As a result, the ionic BJT switches to active mode, and I_C increases with the rise of V_{CE}. A similar modulation effect was also observed for square wave V_{CE} signals (Figure 4.21e). Briefly, under cut-off mode ($V_{EB} < V_T$), I_C was constantly low, while under active mode ($V_{EB} > V_T$), I_C followed the on-off switching of V_{CE}. To quantify the on/off performance, RMS current (I_C) of six successive on-off cycles were calculated. The current on/off ratio between the on state (V_{EB} = 6 V) and off state (V_{EB} = -1 V) was determined to be 17. Finally, the fidelity of our 3D IMP method was confirmed by comparing it with the ionic BJT fabricated by traditional precursor casting method. As shown in Figure 4.22, the cast ionic BJT was measured to possess the same threshold voltage V_T = 2 V and exhibited similar I_C-V_{CE} modulation performances.

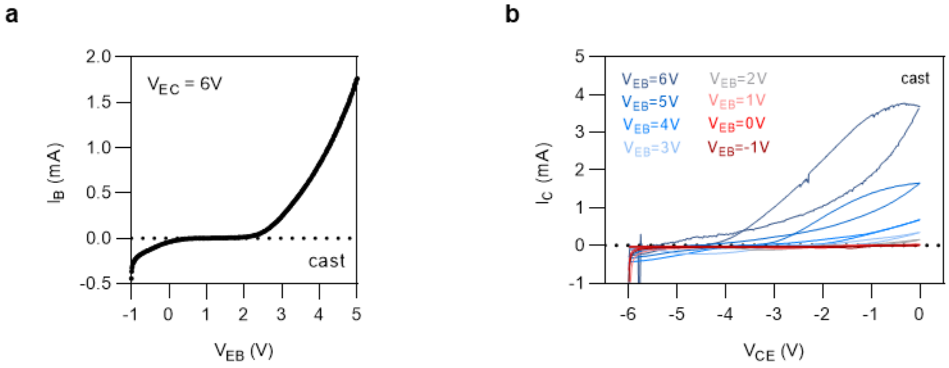

Figure 4.22. Characteristics of the cast ionic BJT show similar performances as printed ones. (a) Base current (I_B) as a function of emitter-base voltage (V_{EB}) at emitter-collector voltage (V_{EC}) of 6 V. Threshold voltage (V_T) is identified as 2 V. (b) Modulation of I_C by V_{EB} as response to sweeping V_{CE}. Scatter plots are presented from representative data from n = 3 samples.

4.5.2 Ionic full-wave rectifier

The full-wave rectifier comprising four connected ionic junctions is shown in Figure 4.23a. The ionic junctions were 3D-printed on a glass substrate with predefined electrode arrays (Figure 4.23b,c); Methods to print flexible substrates and electrodes could also be adopted for a fully flexible and stretchable device[98,171,182]. In response to alternating inputs of positive and negative voltages, the four ionic junctions transition between forward and reverse bias states in synchronized pairs depending on the threshold voltage (Figure 4.24). Specifically, when the input voltage is positive, D1 and D4 are forward-biased, while D2 and D3 are reverse-biased. Current flows through D1 and reaches the positive output terminal; after reaching the negative output terminal, it flows through D4 to the negative input terminal, resulting in a positive output signal. During negative voltage inputs, D2 and D3 are forward-biased, whilst D1 and D4 are reverse-biased. Current first passes through D2, reaching the positive output terminal, and then goes through D3 before reaching the negative output terminal, leading to a positive output signal as well. Hence, in theory, the ionic rectifier should output all positive signals.

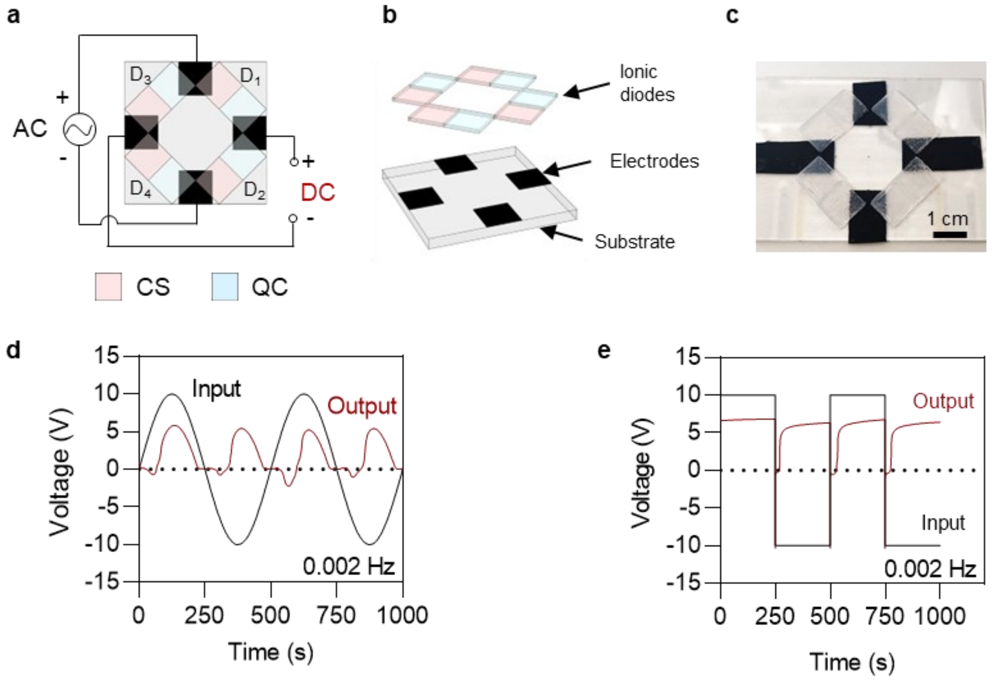

Figure 4.23. Characterizations of the ionic full-wave rectifier fabricated by 3D IMP. (a) Schematic circuit of the ionic full-wave rectifier. (b) exploded view and (c) digital image of the ionic rectifier showing the device structure. (d) Output voltages as response to 0.002 Hz sinusoidal, and (e) 0.002 Hz square wave input voltages. Scatter plots are presented from representative data from n = 3 samples.

Indeed, our printed ionic rectifier successfully demonstrated such rectification effects given both sinusoidal and square wave signals. Figure 4.23d showed the rectification of sinusoidal inputs. Time lag between the output and input were observed, which is due to the time required for the input volage to pass the threshold voltage. In comparison, the square wave inputs lead to much shorter time lags, because of the instantaneous shifting of junction states, where the input voltages immediately exceed the threshold upon switching (Figure 4.23e). These features reflected the characteristics of the ionic junctions. Moreover, the rectifier demonstrated high bandwidth and rectified signals over a wide range of frequencies (0.002 Hz to 1 Hz) (Figure 4.25). As the switching frequencies are limited by the drifting speed of ions, the only charge carriers in the ionic junctions[36,203,207], higher frequencies will result in impaired and unrectified signal outputs.

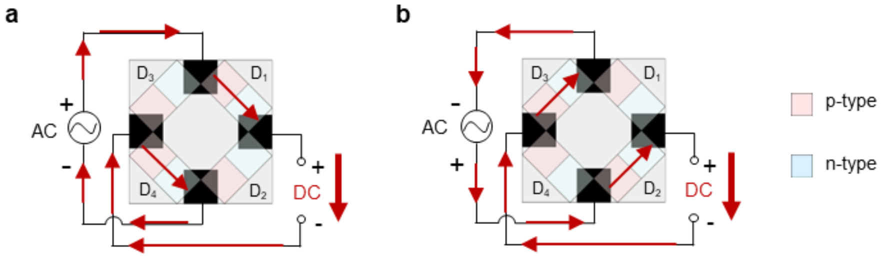

Figure 4.24. Schematic illustrations of the current flow in the printed ionic full-wave rectifiers. Current flow under (a) positive voltage input and (b) negative voltage input.

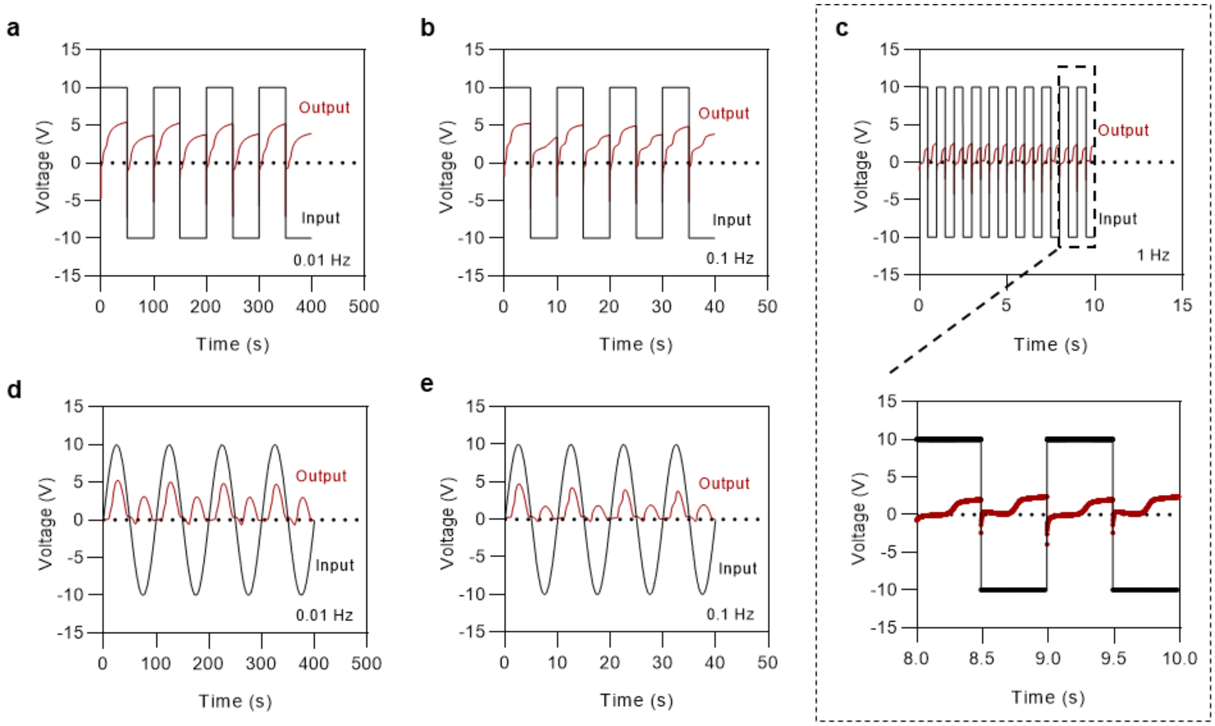

Figure 4.25. Performance of printed ionic full-wave rectifier at various input frequencies. Output voltage as response to (a) 0.01 Hz, (b) 0.1 Hz, and (c) 1 Hz square wave; as well as (d) 0.01 Hz, and (e) 0.1 Hz sinusoidal wave input voltages. Scatter plots are presented from representative data from n = 3 samples.

4.5.3 Ionic touchpad

The last demonstrated ionotronic device is an ionic touchpad, made by 3D IMP of ionic conductive microgels. We printed an array of ionic hydrogels connected with thin copper tapes and sandwiched between silicone layers. Our 3D IMP method offers high precision and resolution. It allowed us to print 16 individual sensing points of 5 mm diameter, 0.8 mm height, and 10 mm pitch (Figure 4.26a), which ultimately yielded a thin and small touchpad (50 mm × 50 mm × 1.6 mm) that was soft and conformable to a hand (Figure 4.26b).

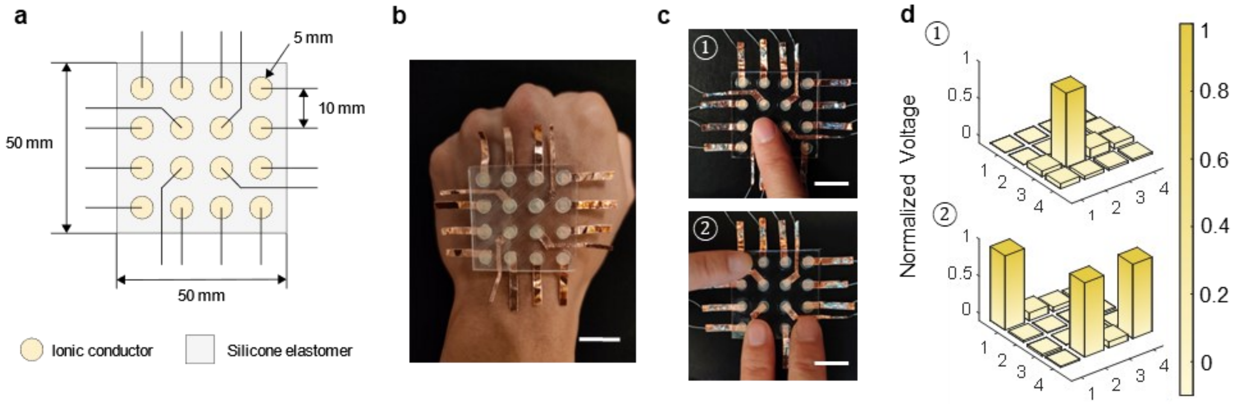

Figure 4.26. Characterizations of the ionic touchpad. (a) Schematic illustration of the TENG touchpad with printed ionic conductor as the current collector. (b) Digital image of the touchpad on the back of a hand. (c) Digital image and (d) corresponding normalized voltage signals of the touchpad detecting ① single-point touch and ② multi-point touches. Scale bar 2 cm.

The sensing mechanism of the touch sensors is based on triboelectric nanogenerators (TENG) under single-electrode mode. They offer simple structures and robust output signals. Briefly, the hydrogels act as current collectors and form EDLs with the electrodes to enhance energy harvesting[127,217], while the silicone elastomer serves as the electrification layer, due to its large electronegativity difference compared to skin[157,158,218]. Upon finger contact and separation, mechanical energy is converted into electricity due to the convoluted effect of contact electrification and electric induction[219,220]. The release of finger contact induces ion flux in the conductive hydrogel layer and polarizes the EDL at the gel-electrode interface, driving electrons to flow in the metal wire. The self-generated voltages power the touchpad and meanwhile serve as sensor outputs. These signals were captured by pairing each sensor with a 100 MΩ resistor and measuring the potential drop across it . To choose the external resistor, an impedance matching test between the internal and external impedances was performed (Figure 4.27a). Voltages across the external loads increased as their resistance increase. 100 MΩ was selected as the external load resistance due to the relatively large voltage level that is within the limit of our data acquisition system.

With this setup, a touch on a pixel yields reliably a positive voltage peak of around 5V, and a release generates a negative voltage peak (Figure 4.27b). The performance of the touchpad was tested for both single- and multi-point touches (Figure 4.26c-d). Touches can be clearly mapped with distinguishable peaks and low noise levels (Figure 4.28, Figure 4.29).

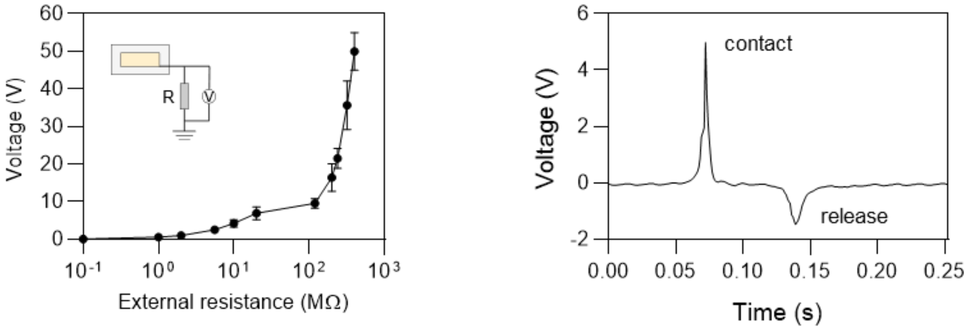

Figure 4.27. Optimization and characteristics of a single touch sensor in the ionic touchpad. (a) Output voltage magnitudes as a function of the resistances of the external loads for a single pixel of the ionic touchpad. (b) Representative output signal of a contact-release action on a single pixel in the ionic touchpad. Scatter plots are presented from representative data. Data are expressed as the mean ± SD from n = 30 samples.

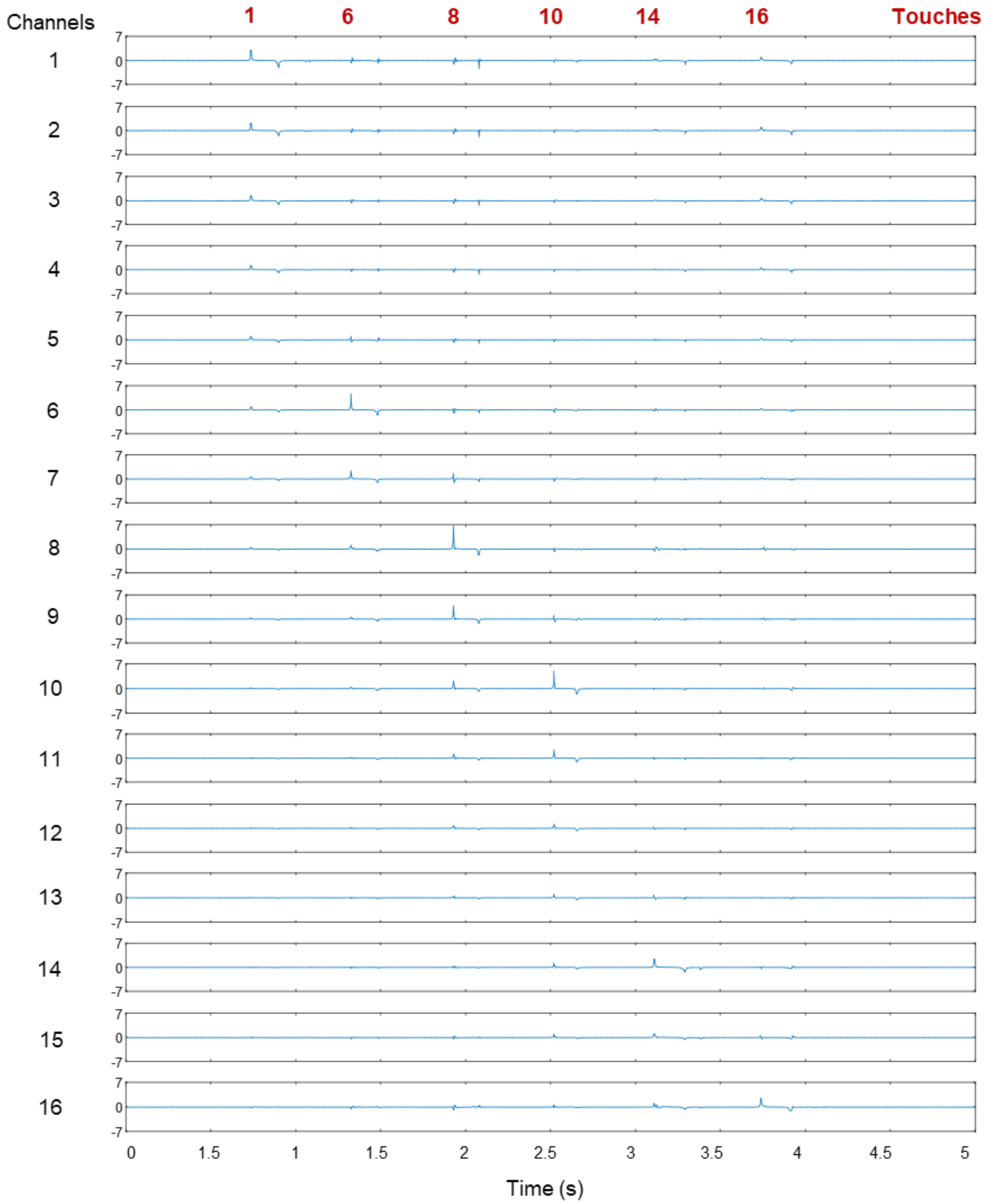

Figure 4.28. Raw output signals of all 16 channels during single-point touches on the ionic touchpad. The touched pixels in sequence were 1, 6, 8, 10, 14, and 16.

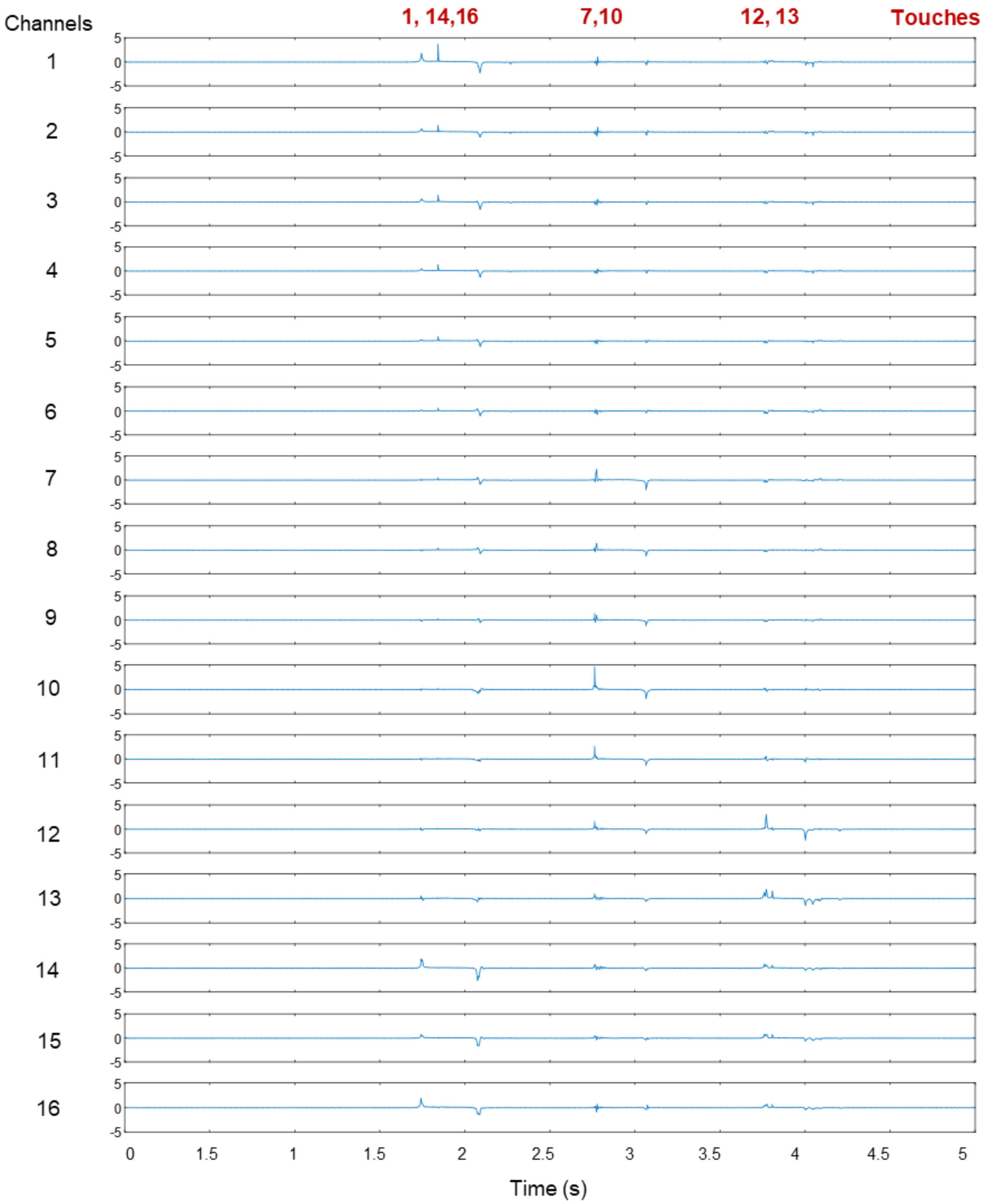

Figure 4.29. Raw output signals of all 16 channels during multi-point touches on the ionic touchpad. The touched pixels in sequence were 1, 14, 16; 7,10; and 12, 13.

CHAPTER 5

Discussions

This chapter discusses the performance and limitations of the PAAc/Chit polyelectrolyte complex hydrogels, the Agar/PAAm DN microgel-reinforced hydrogels, and the 3D IMP method. The findings and implications of these results are discussed comprehensively, in comparison with other works in relevant fields. To mitigate the limitations in the material systems and 3D printing techniques presented in this thesis, potential improvements and future work are suggested. This chapter is structured in four sections: 3D printing, mechanical integrity and disintegration, electrical characteristics, and future work. In terms of 3D printing, topics pertaining to intrinsic printability, high printing fidelity, and limited 3D printing performances are elaborated. In the next section, topics related to mechanical enhancement, adhesion and integration, degradation, and related limitations are discussed. Then, matters related to diverse ionic functions, ionic conductivity, and limited electrical reliability are detailed in the electrical characteristics section. The last section presents future perspectives and outlooks envisioned for the development of 3D-printed hydrogel ionotronics.

5.1 3D Printing

One of the main focuses of this thesis is applying 3D printing technology – specifically DIW – to fabricate ionotronic devices. Such ionotronic devices can greatly benefit from the excellent patterning capability, structural complexity, customizability, rapid embodiment, and upscale potential. The successful DIW of ionotronic devices necessitates careful material design for high printing qualities, which can be evaluated in terms of printability, shape fidelity, and printing resolution.

5.1.1 Intrinsic printability

Conventionally, the flow characteristics of hydrogel inks for DIW are governed by their viscosities and thus determined by the concentration of non-crosslinked polymer solutions[221]. However, since the ink viscosity is also tethered with the strength of post-printed structures, the balancing process is often tedious. Efforts to mitigate such dilemmas have been made to improve the flow of high viscosity inks by integrating extra fillers to facilitate the shear-thinning performances[40,222–225]. Other strategies to circumvent such problems include innovations in in-situ curing[226], embedding printing[41,227,228], and microfluidic printheads for low viscosity inks[229,230].

The material systems and 3D printing strategy proposed in this thesis demonstrated excellent printability, signified by the smooth extrusion, rapid liquid-to-solid transition, and suitable yielding point to support stable printed structures. One of the highlights for the PAAc/Chit hydrogels is their intrinsic printability. The use of high molecular weight polymers formed highly viscous mixtures that were rich in polymer interactions and macroscopically possess relatively high yield strength compared to other liquid precursors. The high yield strength assured the stability of the printed structures at steady state. In the meantime, the PAAc/Chit hydrogels exhibited shear thinning behavior. This salient feature stems from the temporary dissociation of weak bonds or disentanglement of polymer chains under shear stress[231]. Upon application of extrusion force, agitations of high enough rate disentangle the PAAc and Chit long chains and tend to align them along the shear force. This alignment effect leads to less molecular interactions and created larger void spaces inside the polymer solution, causing the macroscopic decreased viscosity[232,233], which ultimately leads to their smooth extrusions.

Whereas the printability of PAAc/Chit hydrogel follows the conventional design principles, the 3D IMP method offered a new design pathway, by leveraging the flow behavior of microgels as packed granular materials. The microgels are able to dynamically transition between a jammed state as a solid and an unjammed state as a liquid; the terminology jamming indicates a rather high particle-to-volume fraction (> 0.58, depending on the shape, heterogeneity, charge, and stiffness)[234]. Due to the softness of the microgels, the interactions between adjacent microgels are convoluted, but are predominately governed by friction force between the microgels, the elastic deformation of individual gels, and other interactions such as electrostatic, hydrogen bonds, and van der Waals forces[235]. Transition of the states under shear forces can be explained by the changes in the thermodynamic states under the input of energy. Rapid granular flow occurs when strong external force (shear force during extrusion printing) exceeds the frictional interactions in the granular materials, therefore displacing them[236,237]. Under either case in this thesis, recovery of the extruded ink to solid state arises from the reversible nature of the collective weak associations that favor assembly[238].

5.1.2 High printing fidelity

The developed printability aides in high shape fidelity. The PAAc/Chit hydrogel showed its capabilities in closely replicating the shapes of diverse load-bearing connective tissues including aorta, IVD, meniscus, and tendon. The resemblance was not limited to simple emulation of the outer shape of the tissues. Exploiting the features of extrusion 3D printing, the printed filaments also closely followed the designed ink-write pathway to imitate the fiber direction of native tissues for mechanical reinforcement on a larger scale. On the other hand, the 3D IMP strategy has been demonstrated to construct various objects and ionotronic devices with precise 3D architectures. The printing accuracy was exemplified by the small sizes of the structures (< 3 cm) and simultaneously accurate reproduction of the subtle shape features according to the CAD models, such as the 400 μm-gap between the left and right side of the miniaturized brain, the 800 μm-gaps between paths of the spiral circuit, and the 400 μm-wide connection between the trapezoidal-shaped ionic junction (Figure 4.7). The shape fidelities are among the best in the field of 3D-printed hydrogels[40,43].

5.1.3 Limitations in 3D printing performances

Despite the promising results, drawbacks to the presented materials and printing strategies in this thesis still exist and require attention in future developments.

Tethered printability and excessive adhesion. First, the PAAc/Chit hydrogel with high ionic strength behaved as a viscous liquid, where the viscosity was predominately influenced by the total polymer content. Although the shape transitioning mechanism offered exceptional mechanical enhancement for the printed constructs, most of the mechanical properties including tensile strength, elastic modulus, and toughness were still related to the total polymer concentration. The pursuit of further extreme mechanics for specific ionotronic devices would inevitably require an increase of polymer concentration, which would deteriorate the printability. As such, the printability is still somewhat coupled with the mechanical properties. This drawback was mitigated in this thesis by the design of the 3D IMP strategy, which completely decouples the ink rheology and the mechanics of printed architecture.

Another drawback for the PAAc/Chit hydrogel in 3D printing is related to the adhesiveness of the pristine polymer solution. Whilst the hydrogen bond-rich polymers contributed to the adhesion on diverse substrates, the excessive adhesion poses risks to the printing operation. During ink extrusion, the hydrogel filaments were either prone to sticking to the tip of the nozzle or struggling to cutoff after finishing printing. This occasionally caused dragging of the filament and destruction of the printed structures. This problem could potentially be solved by adding a retraction step when finishing printing a filament, and prior to movement, by applying a negative pressure and sucking the filament back to the nozzle. Though this function is established in fused deposition modeling (FDM) printers and some customized bioprinters, it is not common for commercially available syringe-pump and pneumatically controlled bioprinters[239,240].

Limited printing resolution. A general limitation to both the material systems during 3D printing is the modest printing resolution, in the range of few hundred micrometers. 3D printing of the PAAc/Chit hydrogels were performed with 20G metal needle nozzles with internal diameters of 603 µm. On the other hand, for the 3D IMP, 22G and 27G plastic conical nozzle were used with 410 µm inner diameter. While the resolution of the 3D-printed PAAc/Chit hydrogels was not specifically examined, that of the 3D IMP was carefully evaluated against varying extrusion pressure and ink-write speed. The optimized resolution reached ~200 µm with 27G nozzle under the settings of 25 kPa extrusion pressure and 7 mm s^{-1} ink-write speed.

Generally, for extrusion-based 3D printing of hydrogels from conventional liquid precursor inks, resolution is determined by the nozzle inner diameter, the flow characteristics of the ink, and the ink-substrate interactions (i.e., wettability, adhesive and cohesive properties, and ink-write speed)[241]. The flow behavior of the ink is further affected by intrinsic ink properties (i.e., viscosity and shear thinning behavior), the nozzle shape, and external extrusion parameters (i.e., extrusion pressure). Characterization of the printing resolutions is not standardized in the field of 3D printing of hydrogels. Since nozzle size is the governing factor that determines the scale of the printing resolution, the resolution of printing was commonly estimated to be the nozzle inner diameter. Typically, extrusion-based 3D printing of hydrogels exhibit resolution in the range of 100-1000 µm[68,242–245], while the current state-of-the-art resolution can reach as high as 30 µm for the printing of conductive polymer hydrogels[182]. One may be inclined to simply switch to a smaller nozzle to improve the printing resolution. However, as nozzle size decreases, high viscosity inks have a higher tendency to create high shear stress. The high resistance to flow is prone to clog the nozzle, leading to discontinued ink deposition. As such, further improvement in the printing resolution is non-trivial. The PAAc/Chit hydrogels manifest such issues. The highly viscous polyelectrolyte complex hydrogels suffered from complications such as discontinued filaments, bursting flow, and nozzle clogging during our attempt to implement a smaller nozzle.

Conversely, the 3D IMP method featured outstanding flow characteristics during extrusion with small nozzles. However, the microgel size constrained the further improvement of printing resolution. As the inner diameter of the nozzles are in the tens to hundreds of micrometers range, this range overlaps with the heterogeneous size distribution of the microgels that were synthesized in this study. Further reducing the size of the nozzle would inevitably jeopardize the printings. The clogging behavior of wet granular materials through a conical channel has been investigated. The determining factors include the ratio of the channel diameter (D) and the particle diameter (d)[246]. Permanent nozzle clogging occurs when $D/d < 2.43$, and continuous smooth extrusion of uniform spherical particles is promised when $D/d > 5.26$, while discontinuous burst flow resides in between. These results provided valuable design guidelines for improving the printing resolution using the ionic microgels despite some discrepancies such as heterogeneity size distribution, stiffness and strength of individual microgels, as well as electrostatic interactions due to the charges. To this end, strategies to be implemented for future evolutions could focus on synthesis of smaller microgels and even nanogels with controlled size distributions. Higher agitation factors during batch emulsion along with stepwise filtering could be carried out, while microfluidic emulsification channels could be applied to produce uniform-sized microgels[188,191,192,201,234,247,248].

5.2 Mechanical Integrity and Degradation

Throughout this thesis, two material systems have been developed with an overarching goal to enhance the mechanical robustness of the post-printed structures. This is because practical application of such ionotronics often require mechanical properties that can be relied upon. Specifically, it is of importance to ensure the mechanical integrity in aspects including the elastic modulus, stretchability, tensile strength, and fracture toughness of individual ionic units, as well as the adhesion between heterogeneous ionic units. These attributes are of particular interest due to three reasons. First, the interface of hydrogel ionotronic devices with human tissues require matching of their mechanical properties. The human tissues are soft and dynamically deformable. Physiological strain level measured on human tissue range from 10% on the brain[249], to 10%-20%

on muscle and heart, to 50% on skin[250]. In the meantime, the soft human tissues are also tough and fracture resistant, with the fracture toughness of skin and cartilage higher than 1000 J m^{-2} [21]. These values serve as the criteria when designing the hydrogel ionotronic materials. Second, device reliability and durability are crucial during practical daily usage. Third, ionotronic devices necessitate multiple ionic units for diverse functionalities. Breakdown of one single component or the disintegration between components could lead to malfunction or catastrophic failure of the whole device.

5.2.1 Mechanical enhancement

Strengthening and toughening of hydrogels have been achieved by two main strategies: manipulating the network structures to avoid defects, and incorporation of energy dissipative mechanisms such as sacrificial bonds and healable non-covalent bonds[241,251–254]. Under the scope of this thesis, the mechanical enhancement strategies should also be compatible with the extrusion-based 3D printing. A good example of this is the addition of nanoclay that serves as both a rheological modifier and a strengthening moiety[187,255]. In this thesis, two mechanical enhancement methods were adopted, phase-transition-induced condensation of polymer networks for the PAAc/Chit hydrogels and microgel-reinforced energy dissipation for the 3D IMP of DN hydrogels.

Through careful material design and mechanism investigations, the PAAc/Chit hydrogels were demonstrated to significantly enhance their mechanical properties post-printing by phase transition. With a two-order-of-magnitude increase in elastic modulus, tensile strength, and fracture toughness, the hydrogel transformed from a soft and injectable glue to a stretchable and tough solid. The enhancement is especially highlighted by the fracture toughness, reaching a marked 2500 J m^{-2}, which is comparable to reported values for 3D-printed hydrogels[105,111–114,116]. The exceptional mechanics was ascribed to the utilization of macromolecule crosslinkers PAAc and Chit, which eliminated the need for cytotoxic monomers and crosslinkers typically required for creating stretchable hydrogels. During phase transition, physical interactions such as hydrogen bonds, electrostatic interactions, and topological entanglements were enriched by ion exchange process, and the polymers chains were condensed. The abundance of physical interactions served as means of energy dissipation under deformation, thus leading to effective mechanical augmentation.

The 3D IMP strategy took another route for mechanical enhancement by using DN crosslinking and microgel-reinforced toughening mechanisms. The resulting material featured a two-phase composite structure, with DN PAAm/Agar microgels embedded in PAAm hydrogels. The inclusion of the covalently crosslinked polymer PAAm infiltrated into the microgels and in between them, forming a homogeneous stretchy network that significantly improved the cohesiveness of the material. As a result, the 3D ionic microgel printed ionic junction demonstrated maximum stretch values of greater than 20, one order of magnitude higher than that of the SN agarose hydrogels. The other part of the hydrogel composite, DN microgels, contributed to the substantial strengthening and toughening of the material. During deformation, the microgels exhibited mesoscale fractures and breakage of sacrificial physical bonds to absorb energy[211]. In consequence, the microgel-reinforced DN hydrogels demonstrated two orders of magnitude augmentation in fracture toughness compared to the SN hydrogels. The achieved fracture toughness 1200 J m^{-2} was on the lower side of what have been achieved for 3D-printed tough hydrogels in the literature (1000-9000 J m^{-2}), potentially due to the impaired crosslinking of the PAAm network caused by the infiltration of oxygen during the printing process. Such problems could be solved by printing in nitrogen environments, purging the printed structures with inert gas for sufficient amount of time, or the inclusion of oxygen scavengers such as glucose and glucose oxidase in the printable inks[187,256]. In addition, introducing dynamic covalent crosslinking to the microgels has the potential to further enhance the mechanical properties of the 3D IMP hydrogel ionotronics[248,257].

5.2.2 Adhesion and integration

The crucial role of adhesion and integration in ionotronic devices was exemplified in two general aspects. First, robust integration between different device components inside an ionotronic device prevents delamination during deformation and ensures a stable and reliable operation. Second, ionotronics excel when interfacing with the human body. While conformable contacts promote mechanical integration, which benefits long-term wearing comfortability and implantation biocompatibility[258], strong adhesion to biological tissues further assures effective communication between human and machine.

In this thesis, the PAAc/Chit hydrogels demonstrated strong adhesion to diverse non-biological and biological substrates. When interfacing with synthetic materials such as PAAm/Alg hydrogels, a high interfacial toughness of 300 J m^{-2} was achieved. The robust bonding was further evinced when stretching the hydrogel substrate with printed PAAc/Chit mesh, where the mesh was firmly attached to the substrate and correspondingly deformed throughout the loading-unloading cycles. The results indicated the strong inter-component integration offered by the PAAc/Chit hydrogels when implemented in ionotronic devices. The robust interfacial adhesion was ascribed to both the tough hydrogel matrix, enabled by the condensed polymer network and the abundance of physical and covalent bonds at the interface[50,259,260]. On the other hand, the PAAc/Chit hydrogels also presented strong adhesion to biological tissues in wet and physiological environments. Given their high toughness, which matches the extreme mechanical properties in the connective tissues, the PAAc/Chit hydrogels are prominent to combine the functions of tissue repairs and implantable sensory devices towards the future of digitalized healthcare.

Whereas most efforts have been devoted to advancing the adhesion of hydrogel ionotronic components to biological tissues and other passive ionic components[46,99–101,261–266], little attention has been paid to the adhesion between ionic-active components[38,267,268]. The 3D IMP strategy excelled in uniting heterogeneous ionic modules and creating ionotronic devices with outstanding integrity. The rough inter-component interfaces created by the microgels resulted in a 3-fold increase in the adhesion energy compared to the smooth solution-casting counterparts. Further, the topological effect together with the homogeneous interpenetrating PAAm network throughout the whole device led to a two orders of magnitude enhancement in interfacial toughness compared to pure SN devices. The adhesion energy between p- and n-type materials achieved 579 J m^{-2}, higher than those attained in ionoelastomers (339.3 J m^{-2})[268]. This attribute is highly desirable for the reliability of soft devices with multiple ionic-active constituents that would expect large deformations during use. Advances in binding dissimilar ionic units is one of the most important directions in the future development of ionotronics in achieving fully ionic integrated circuits.

5.2.3 Degradation

Another highlight in the ionotronic materials presented in this thesis is their degradability. Designing a fully degradable hydrogel ionotronic device entails specific demands for both the material system and fabrication method. Each component must be degradable, but without prematurely compromising mechanical or electrical performance. Although reported hydrogels can degrade hydrolytically or enzymatically[215,269], existing ionotronics are primarily based on synthetic polymer networks containing non-degradable backbone polymers and charged polymers.

In this thesis, degradability was enabled by the combination of biopolymers and degradable crosslinkers for the synthetic polymer network of the 3D IMP ionic junctions. The hydrolytic degradation of the easter bonds in the PEGDA crosslinker for the PAAm network dominated the degradation process, demonstrating a 91% weight loss in DPBS after 7 days. In the meantime, the ionic junctions maintained stable operation for 4 days before complete breakdown. While rapid degradation was presented in this work, a few biopolymer and synthetic matrix with different degradation rates in diverse environments were demonstrated for hydrogel ionotronics, including gelatin[270], PAA/gelatin[271], PVA/cellulose[272], Agar/cellulose[28], silk[273], carboxylate chitosan/sulfobetaine methacrylate[274], glutinous[275], and PAAm[276]. In our case, to allow for controlled degradation profiles for different application scenarios, the inclusion of both degradable (PEGDA) and non-degradable (MBAA) crosslinkers is hypothesized to be a promising strategy.

Nevertheless, the enzymes in our study had insignificant effects on the degradation profile. Theoretically, agarose could be degraded by other enzymes and bacteria[212,277,278]; the enzymes used in this study (collagenase and lysozyme) were not effective to degrade agarose. The results imply that matching enzymatic cues is essential to in vitro degradation of hydrogels. Considerations in the degradation conditions and practical application scenarios are also supposed to play a key role in the design of hydrogel matrix in ionotronics.

From a broader perspective, the degradation of electronic and ionotronics holds significant importance for two key reasons. First, degradable devices ensure sustainability. The extensive use of electronics and the booming development of wearable devices foresee 74 million tons of electronic waste in 2030[279–281]. To alleviate such environmental crisis, substantial research efforts have been made to develop electronics that could degrade after their lifespan and be reclaimed by nature[282–286]. Nevertheless, few studies have demonstrated degradable hydrogel ionotronics. Secondly, the consideration of degradation is crucial for implantable devices. Endowing degradability to these devices could eliminate the need for secondary surgeries and thereby reduce potential clinical complications.

5.2.4 Limitations in mechanical performances

Apart from the highlights in mechanical performances, there are several drawbacks underlying the mechanical characteristics of the material systems developed in this thesis, which require attentions in future studies.

Volume shrinkage. Whereas the PAAc/Chit hydrogels undergo mechanical enhancement via phase transition, the condensed polymer network induced substantial shrinkage in the printed structures. Though the contraction was observed to be homogeneous and isotropic, where the designed and as-printed architectures were greatly preserved after phase transition, this behavior is still undesirable in hydrogel ionotronics. When deployed alone in a single-unit ionotronic device, such as the presented strain sensor, the volume decrease poses minimal effects to the device function, albeit it is expected to significantly affect the structures and functions of multi-unit ionotronic devices.

Encoded defects. The uniformity of the 3D IMP ionic junctions was not as ideal as the ones fabricated by precursor casting. The heterogeneous size distribution of the microgels together with the layer-by-layer and filament-by-filament deposition encoded some defects in the printed structures. Mechanically, the defects posed risks in causing stress concentration under loading and resulting in more unpredictable rupture events. Indeed, this is evinced by the large error bar in the measured maximum stretch of the printed ionic junctions during pure shear tests (Figure 4.18). Electrically, the defects might locally deteriorate electrical functions and lead to nonuniform electrical properties. To mitigate this issue, microgels of more uniform size distributions could be synthesized as mentioned previously and carefully calibrated infill densities could be implemented to minimize the nonuniformity. In addition, implementing smaller microgels and improving the microgel ink jamming could avoid large air gaps, improve the packing density, and effectively decrease the defect size.

5.3 Electrical Characteristics

Electrical performances are the core attribute that determines the functions of hydrogel ionotronics. In ionotronics, ions are the main charge carriers. In most cases, the movement of ions inside matrix materials generate ionic currents, while the manipulation of ionic current endows different ionic functions. By design, various ionic species were included in the ionotronic materials presented in this thesis and achieved generally three different ionic functions: basic ionic conduction with decent ionic conductivity, linear electromechanical coupling behavior, and outstanding current modulation performances.

5.3.1 Ionic conductivity

In an ionic conductor, electricity is conducted by mobile ion transportation. The PAAc/Chit hydrogel was shown to possess an ionic conductivity of 0.55 S m^{-1}, consistent with the values obtained for polyelectrolyte hydrogels in the literature[287,288]. Nevertheless, the PT hydrogels showed a significantly decreased conductivity of 0.053 S m^{-1}. This overall drop in conductivity is due to the combined effect of decreased number of charge carriers and decreased ion mobility. Since the conductivity of polyelectrolyte hydrogels stems from the mobile counterions that are associated with the charged polymer chains, the interactions between the mobile counterions and the polymers play a crucial role in affecting the ionic conductivity. In the polyelectrolyte complex hydrogels, the mobile sodium ions, chloride ions and protons carry charges. After phase transition, the electrostatic interaction between the PAAc chains and Chit chains intensified, leading to substantially decreased net ionic strength. As a result, the polyelectrolyte complex system lost a considerably large number of mobile ions to the surrounding environment, thus showing attenuated ability to carry charges. Additionally, the contracted polymer network reduces the void spaces and further hinders the transportation of ions, deteriorating their mobility[196,207,289].

The conductivity of the 3D IMP Agar/PAAm hydrogels follow the same principle of ionic conduction principles, but with more complexity – considering the physical barriers between the microgels. The p-type (0.406 S m^{-1}) and n-type (0.147 S m^{-1}) conductors resemble that of the pristine PAAc/Chit hydrogels. Polycations and polyanions bring corresponding mobile ions to the materials as charge carriers, and the ionic conductivities are related to the polyelectrolyte concentrations. On the other hand, the pure ionic conductors contain both positive sodium ions and negative chloride ions as charge carriers. With the added high mobile ion concentrations, a high ionic conductivity of 2 S m^{-1}. Comparing to the widely used PAAm hydrogel ionic conductors (~30 S m^{-1})[51], the microgel-reinforced hydrogel showed inferior conductivity. Unlike the charged polymer backbones in the PAAc/Chit hydrogels, the matrix polymers PAAm and agar are generally neutrally charged and do not pose electrostatic effect on the mobile ions. Instead, the compromised conductivity is due to the rather dense polymer matrix and the less efficient transportation of ions across microgels. The inferior conductivities are not necessarily a drawback, as the overall essence is about matching the ionic conductivities to the application scenarios. While a high conductivity is preferred for signal and power transmissions, a low conductivity matching that of the tissues is desired when interacting with tissues for self-resolved bio-signal measurements and accurate stimulation[124,163]. However, to enhance ionic conductivities, ionic microgels serve as a great vessel, providing versatility in both materials and fabrication design. Instead of electrolytes and polyelectrolytes, other conductive moieties could be incorporated in the microgels to enable electrical conductivity. Some options include conductive polymers, poly ionic liquids, and inorganic conductors.

5.3.2 Diverse ionic functions

Most hydrogel ionotronics employ ionic species to function as pure ionic conductors. The approaches in manipulating the ions inside a hydrogel matrix are monotonous, and the variety of ionic functions are scarce. Due to these reasons, few works have been presented to construct integrated devices with pure ionic units[205].

The 3D IMP method presented in this thesis exemplified a versatile approach to incorporate diverse ionic species in achieving diverse ionic functions. The inclusion of polyanion and polycation in the microgels create p-type and n-type ionic units that could form an ionic junction when contacting. When operating alone, the ionic junction rectifies ionic currents by allowing unidirectional current flow like a diode, whereas combining multiple ionic junctions created functional transistors and rectifiers. The key to this design flexibility roots from the solid nature of the microgels, where the ionic unit as inks do not mix during printing to avoid premature deterioration of the ionic functions. Aside from expanding functionalities, owing to the universalness of the microgels as vessels, the 3D IMP also offered flexibility for enhanced performances.

One limitation in our material design is that the ionic species are not securely fixed to the polymer matrix of the microgels, especially the inclusion of NaCl in the ionic conductors. Though the implemented long chains polyelectrolytes are expected to entangle on the polymer backbone, diffusion of mobile ions and drifting of polyelectrolytes under external electrical field is still possible. To mitigate this, chemical modifications could be applied to the polyelectrolytes to anchor them onto the matrix polymer network, such as creating copolyelectrolytes using methacrylated polysaccharides as polymer backbones[27]. Further, macromolecules such as conducting polymers and zwitterionic polymers could be employed as active ionic species in the pure ionic conductors.

5.3.3 Limited electrical reliability

Mechanical loading memory. A common limitation for both materials developed in this thesis is the mechanical memories, pertaining to hysteresis and plastic deformation. Whereas the hysteresis during stretching of the PAAc/Chit hydrogels served as a means of energy dissipation for tougher mechanics, the irreversible microscopic changes in the polymer structures alter the bulk mechanical properties of the material over cycles of loading-unloading. Likewise, in the 3D IMP ionic junctions, the microgels served as load dissipator during large deformations. The dissipation effect could be evinced by the phase separation between the originally uniform microgels and the infiltrated PAAm polymer network. In both cases, plastic deformations after stretching were observed and the mechanical properties were irreversibly changed. As the materials exhibited electromechanical coupling effect, the electrical performances were expected to deviate from its pristine state. Indeed, when the PAAc/Chit hydrogels were used as a strain sensor, permanent elongation after cycles of finger bending caused buckling of the hydrogel when returning to 0 degrees and an increasing trend in the baseline of resistance measurements (Figure 3.16). Though the effect of hysteresis to electrical performances was not illustrated for the 3D IMP ionic junctions, similar effects were expected. The separation of phases between the discrete microgels and the continuous PAAm network during large deformation could also anticipate early device breakdown in electrical functions before the mechanical rupture of the whole structure.

This problem is prevalent in hydrogel ionotronics, where energy dissipators were preferentially selected in the pursuit of softness and high toughness. Though the deformations of human tissue do not exceed strain of 75%[290], precautions should still be taken. From materials design perspective, self-healing hydrogels, or purely elastic hydrogels with optimized polymer networks could be used to face this challenge.

Electrochemical stability. In this thesis, hydrogels are the materials used for ionotronics. They contain more than 80% water. Typically, hydrogel ionotronics effectively transmit alternating currents or produce electric fields. However, under direct current with overpotential at the EDL exceeding 0.828 V, electrolysis of water at the electrode occurs. The faradaic current is a double-edged sword. On one hand, hydrolysis produces protons and hydroxyl ions at the hydrogel–

electrode interfaces. The increased number of mobile ions adds to the existing ones and enhances the charge-carrying abilities of the ionotronic material, which in turn contributes to higher ionic current. For ionic conductors, the apparent effect is elevated ionic conductivity, while for ionic junctions, the situation is more complicated. Under forward bias, protons are generated at the anode that interfaces with the p-type hydrogels, while hydroxyl ions are generated at the cathode that interfaces with the n-type hydrogels. Upon creation, the mobile ions drift immediately to the opposite side of the junction under external electric field and substantially increase the ionic current. Under reverse bias, protons are generated near the n-type hydrogels, whereas hydroxyl ions are produced near the p-type hydrogels. Though the external electric field tends to drive the ions to the opposite side of the junction, the existing mobile ions that are accumulated at the electrodes capture the generated ions, suppressing the ionic current. Depending on the overpotential and the reaction kinetics, balancing of these two counter effects yields either increased or decreased ionic current under reverse bias. On the other hand, though the electrochemical process is modeled, water in hydrogel is consumed gradually, deteriorating the device structure and function overtime. Further, the oxygen and hydrogen gas formed at the electrodes are not ideal for stable practical operations.

To avoid faradaic process under direct current, there are two solutions. First, the overpotential at the hydrogel–electrodes interface could be limited within the electrochemical window, whose absolute value is 0.828 V at the cathode and 1.23 V at the anode[197,198]. This could be achieved by limiting the operation condition to low voltage scenarios and by proper device design to divide the voltage among different circuit sections, so that the voltage drop across the EDL is within the electrochemical window. This had been achieved in ionic actuators involving dielectrics even when operating under 10 kV, since the drastically smaller capacitance value of the dielectric when in series with the EDL occupied most of the voltage drop[51]. However, this is intrinsically difficult for devices like the ionic junction, since the IDL is paralyzed under forward bias and the EDLs hold most of the voltage drop from external voltage sources. The second remedy is to avoid the inclusion of water by using alternative solvent materials (e.g. ionogels) or liquid-free materials (e.g., polyelectrolyte elastomers[199,268,291]) to form ionotronics. Although ion mobility will be suppressed due to stronger interaction between mobile ions and adjacent polymer chains, the enhanced electrochemical stability will allow application in broader scenarios.

5.4 Future Work

Despite the amazing progress and rapid development, 3D printing of hydrogel ionotronics is still in its infancy. Here are some future perspectives and outlooks that are envisioned for hydrogel ionotronics as the next generation wearable and implantable devices.

Current 3D printing methods for hydrogel ionotronics are far from translation or commercialization. Although extrusion-based 3D printing offers effective, rapid, facile, and low-cost solutions for constructing hydrogel ionotronics in 3D space, the rather low printing resolution (> 30 μm) stands to be one of the largest hurdles in future developments. This drawback is especially notable when compared to current electronic components at nanometer scale. However, instead of employing DIW as the mainstream mass production methods for ionotronic devices, they can serve as a strong tool during this exploration stage. Considering the popularity and rather facile operation, DIW can bridge the gap between the manual assembly era and the future commercialization stage. On one hand, with the booming development in various ionotronic materials, DIW is a fast and accurate fabrication method to verify the functionalities of new materials and rapidly prototype ionotronic devices. The capability of DIW to accurately deposit hydrogels in 3D spaces largely reduces the adverse effects of manufacture discrepancies on device performances and allows one to focus on the effect of materials. On the other hand, the much higher resolution, smaller features, and structural complexity offered by DIW, compared to current fabrication methods, will reveal the significant role of device structural design to device functions. Specifically, compared to mold casting and manual assembly method, DIW can produce smaller ionic units in ionotronic devices and allow positioning of these components with higher precision. Reducing component sizes can lead to enhanced electrical performances (e.g., faster response, higher rectification ratio) in most ionotronic elements due to the decreased ion travel distances and intensified electric field distribution[36,207]. Smaller ionic components also allow for miniaturization of the overall ionic devices to accommodate for the often-limited spaces during applications. In addition, a larger number of ionic elements could be integrated within confined build volume to support better performances (e.g., more transistors for stronger computational power) or expand the variety of functions. The capability of DIW to build intricate structures renders it a powerful tool to fabricate and combine the same set of materials in various configurations. This design freedom enables the creation of new device functionalities through different device architectures, as exemplified by a recent work on DLP printing of ionotronic capacitive sensors that can perceive different types of mechanical stimuli by using different architectures[268]. To this end, DIW holds great possibility for improving electrical performance[29,193] or inventing new ionic functions, and will pave the road for the future development of high-resolution 3D-printed devices. In the meantime, other 3D printing technologies, especially light-based methods such as SLA, DLP[292], and selective laser sintering (SLS), are promising alternatives to facilitate the development of ionotronics to the industry. They offer much higher resolutions (~ 1 μm), can readily inherit the experience and equipment from the lithography process used in current semiconductor industries, but still require further optimization to accommodate for the production of soft ionotronics.

Inspired by skin, multifunctionality with distinct decoupling of different signal types is desirable. The inclusion of multi-functions in one single device broadens the application range and enables a more efficient device platform. Examples of such devices are often developed as sensors that possess multimodal sensing[19]. The ability to measure multiple stimuli orthogonally requires further exploration in material design, device structures, and sensing mechanisms. Some pioneering works in this topic include an artificial multimodal receptor for heat and mechanical stimuli based on ion relaxation dynamics[293], a multimodal temperature and strain sensor based on capacitive and resistive dual response, and multiaxial pressure sensors based on capacitive sensor arrays[294,295]. It is important to note that multifunctionality without clear decoupling mechanisms is problematic in practice. As the functionalities are tethered without deciphering strategies, they would only act as disturbances to each other. For sensors that respond to multiple external stimuli, changes in other affecting factors would act as noises for the measurement of the targeting input stimulus and deteriorate its function. For other ionotronic components, mechanical deformations often alter the electrical performances. Beyond strain sensors, these electromechanical coupling effects cause unstable device performances and are hazards in practical applications. As such, strain-insensitive hydrogel ionotronics are in high demand[16].

The performances of ionotronics are far inferior to commercial electronics. For example, the conductivity of ionic conductors are in the range of 0.01-1000 S m^{-1}, while metal conductors have conductivity of ~10^7 S m^{-1} [296,297]; ionic diodes possess rectification ratio of 5-300 [298], whereas commercial silicon diodes have typical values of 10^5 [299]. Further improvements on the electrical performances of ionotronics rely on better understandings of the current conduction mechanisms. Unlike electronic conduction, ionic conductivity relies on the transport of ions in various media, which can be treated as a mass transport problem. Further development in hydrogel ionotronics requires more profound understanding in the physical nature of ions and their behavior in hydrogel matrix. A deeper understanding would be beneficial to exploit the advantages while circumventing the limitations of ions in designing ionotronics. Modeling of the ionic transportation in ionotronic materials can predict device performances, offer guidelines in materials and device optimizations, and provide valuable insights into their applications[200]. Potential directions include studying the transportation of ions in dense polymer networks, or within matrices of different charge environments, or under mechanical stimuli, or during electrochemical reactions.

CHAPTER 6

Concluding Remarks

This thesis is centered on addressing two engineering challenges associated with 3D printing of hydrogel ionotronics: (1) simultaneously achieving high ink printability, mechanical robustness, and uncompromised ionic performance; (2) printing multiple active ionic units in one ionotronic device for expanded functionalities.

First, a family of polyelectrolyte complex hydrogels featuring positively charged Chit and negatively charged PAAc were developed to achieve printability and toughness. While at specific polymer ratios, the hydrogels could condense their polymer network and transform from a printable polymer solution to a strong and tough hydrogel solid, other ratio resulted in brittle and swollen hydrogels. Investigations in the kinetics and environment pH revealed the ion exchange process during the phase transition under benign physiological conditions. Both increased polymer content and the inclusion of covalent coupling reagent EDC/NHS were proven to augment the mechanical performances. The mobile counterions associated to the polyelectrolyte backbones enabled intrinsic ionic conductivity. Though the PT hydrogels exhibited compromised conductivity, the decent linearity in electromechanical coupling within a wide range of stretch level supported their application as strain sensors. The high-molecular-weight polymers facilitate the printability of the PAAc/Chit hydrogels. While the appropriate printing time window facilitated smooth printing operations, the shear yielding, shear thinning, and self-recovery characteristics guarantee printability. The high shape fidelity of the printed tissue mimetics further evinced the excellent printing quality. Combining 3D-printability, strong adhesion, and controlled volumetric changes, applications of the PAAc/Chit hydrogels, including patterned adhesion, air/liquid pocket and channels, as well as morphing hybrid structures, were demonstrated. To conclude, the presented material concurrently achieved printability, high toughness, and ionic conduction, and thus stands as a promising solution for 3D printing of hydrogel ionotronics. It has further potential to open avenues in implantable devices, surgical phantoms, and tissue repair.

To enable 3D printing of multiple ionic materials and expand ionic device functions, the 3D IMP strategy was proposed. The intrinsic high printability of the microgels was confirmed with rheological measurements, and various intricate 3D structures with high fidelity were 3D-printed. The microgels served as vessels to incorporate three different ionic species that could be freely combined in 3D space during printing without mixing or compromising ionic functions. In addition to the remarkable printing qualities, the ionic microgels also toughened the hydrogel matrix and promoted the adhesion between different ionic units when implemented with the DN crosslinking strategy, which substantially improved the overall mechanical performance of the 3D-printed ionic junctions. With the microgel-reinforced strategy, the printed ionic junctions achieved high stretchability, high fracture toughness, and high interfacial toughness. The combination of agarose microgels, hydrolysable crosslinkers, and degradable polyelectrolyte allowed the device to degrade within 1 week for transient stability. Due to the high-charge-density biopolymers (CS and QC), extremely high rectification ratios were demonstrated by tuning the polymer concentration, desalination state, and size. The formation of an IDL and the faradaic rectification process of the ionic junctions were confirmed and analyzed quantitatively with equivalent circuit models that are fitted to EIS data. With the established 3D IMP method, a variety of ionotronic devices with multiple heterogeneous ionic units, including ionic diodes, ionic bipolar junction transistors, ionic full-wave rectifiers, and ionic touchpads were fabricated, and their functionalities were validated. To sum up, the 3D IMP offered a versatile approach to 3D-print high-performance hydrogel ionotronics with heterogeneous ionic components and robust mechanics. This study provides new possibilities for the design and fabrication of multi-component hydrogel ionotronics and enlightens new applications in stretchable and wearable devices.

Overall, this thesis presents the design of novel material systems and innovative fabrication strategies for hydrogel ionotronics by taking advantages of the physical properties of multi-form hydrogels, various mechanical toughening mechanisms, and ionic functionalities of diverse ionic species. From wearable and implantable devices to synthetic biology and cyborgs, the integration of humans to machines has started to sprout and will become an indispensable technology in the future. Hydrogels ionotronics, thanks to their tissue-like mechanical, chemical, and electrical characteristics, will play a crucial role in realizing intimate interfaces between humans and machines.

Bibliography

1. Bernards, D. A., Flores-Torres, S., Abruña, H. D. & Malliaras, G. G. Observation of electroluminescence and photovoltaic response in ionic junctions. *Science* **313**, 1416–1419 (2006).
2. Rogers, J. A., Someya, T. & Huang, Y. Materials and mechanics for stretchable electronics. *Science* **327**, 1603–1607 (2010).
3. Wang, C., Wang, C., Huang, Z. & Xu, S. Materials and structures toward soft electronics. *Adv. Mater.* **30**, 1801368 (2018).
4. Kim, D., Xiao, J., Song, J., Huang, Y. & Rogers, J. A. Stretchable, curvilinear electronics based on inorganic materials. *Adv. Mater.* **22**, 2108–2124 (2010).
5. Kim, D.-H. *et al.* Materials and noncoplanar mesh designs for integrated circuits with linear elastic responses to extreme mechanical deformations. *Proc. Natl. Acad. Sci.* **105**, 18675–18680 (2008).
6. Khang, D. Y., Jiang, H., Huang, Y. & Rogers, J. A. A stretchable form of single-crystal silicon for high-performance electronics on rubber subtrates. *Science* **311**, 208–212 (2006).
7. Xu, S. *et al.* Soft microfluidic assemblies of sensors, circuits, and radios for the skin. *Science* **344**, 70–74 (2014).
8. Choi, S., Han, S. I., Kim, D., Hyeon, T. & Kim, D. H. High-performance stretchable conductive nanocomposites: Materials, processes, and device applications. *Chem. Soc. Rev.* **48**, 1566–1595 (2019).
9. Chen, X., Rogers, J. A., Lacour, S. P., Hu, W. & Kim, D.-H. Materials chemistry in flexible electronics. *Chem. Soc. Rev.* **48**, 1431–1433 (2019).
10. Sekitani, T. *et al.* A rubberlike stretchable active matrix using elastic conductors. *Science* **321**, 1468–1472 (2008).
11. Sekitani, T. *et al.* Stretchable active-matrix organic light-emitting diode display using printable elastic conductors. *Nat. Mater.* **8**, 494–499 (2009).
12. Huang, S., Liu, Y., Zhao, Y., Ren, Z. & Guo, C. F. Flexible electronics: stretchable electrodes and their future. *Adv. Funct. Mater.* **29**, 1–15 (2019).
13. Kim, D. C., Shim, H. J., Lee, W., Koo, J. H. & Kim, D. Material-based approaches for the fabrication of stretchable electronics. *Adv. Mater.* **32**, 1902743 (2020).

14. Yang, C. & Suo, Z. Hydrogel ionotronics. *Nat. Rev. Mater.* **3**, 125–142 (2018).
15. Cao, Y. *et al.* A transparent, self-healing, highly stretchable ionic conductor. *Adv. Mater.* **29**, 1605099 (2017).
16. Lei, Z. & Wu, P. A highly transparent and ultra-stretchable conductor with stable conductivity during large deformation. *Nat. Commun.* **10**, 1–9 (2019).
17. Yao, B. *et al.* Hydrogel ionotronics with ultra-Low impedance and high signal fidelity across broad frequency and temperature ranges. *Adv. Funct. Mater.* **32**, 2109506 (2022).
18. Lee, H. R., Kim, C. C. & Sun, J. Y. Stretchable ionics – a promising candidate for upcoming wearable devices. *Adv. Mater.* **30**, 1704403 (2018).
19. Ying, B. & Liu, X. Skin-like hydrogel devices for wearable sensing, soft robotics and beyond. *iScience* **24**, 103174 (2021).
20. Sun, J. Y. *et al.* Highly stretchable and tough hydrogels. *Nature* **489**, 133–136 (2012).
21. Li, J., Illeperuma, W. R. K., Suo, Z. & Vlassak, J. J. Hybrid hydrogels with extremely high stiffness and toughness. *ACS Macro Lett.* **3**, 520–523 (2014).
22. Liang, X. *et al.* Anisotropically fatigue-resistant hydrogels. *Adv. Mater.* **33**, 2102011 (2021).
23. Ge, G. *et al.* Muscle-inspired self-healing hydrogels for strain and temperature sensor. *ACS Nano* **14**, 218–228 (2020).
24. Wei, D. *et al.* Highly stretchable, fast self-healing, responsive conductive hydrogels for supercapacitor electrode and motion sensor. *Macromol. Mater. Eng.* **305**, (2020).
25. Ying, B., Wu, Q., Li, J. & Liu, X. An ambient-stable and stretchable ionic skin with multimodal sensation. *Mater. Horizons* **7**, 477–488 (2020).
26. Ying, B., Chen, R. Z., Zuo, R., Li, J. & Liu, X. An anti-freezing, ambient-stable and highly stretchable ionic skin with strong surface adhesion for wearable sensing and soft robotics. *Adv. Funct. Mater.* **31**, 2104665 (2021).
27. Lee, H. *et al.* A stretchable ionic diode from copolyelectrolyte hydrogels with methacrylated polysaccharides. *Adv. Funct. Mater.* **29**, 1–8 (2019).
28. Nyamayaro, K. *et al.* Toward biodegradable electronics: ionic diodes based on a cellulose nanocrystal–agarose hydrogel. *ACS Appl. Mater. Interfaces* **12**, 52182–52191 (2020).
29. Wang, Y., Wang, Z., Su, Z. & Cai, S. Stretchable and transparent ionic diode and logic gates. *Extrem. Mech. Lett.* **28**, 81–86 (2019).
30. Tybrandt, K., Forchheimer, R. & Berggren, M. Logic gates based on ion transistors. *Nat.*

Commun. **3**, (2012).

31. Duan, J. *et al.* Tough hydrogel diodes with tunable interfacial adhesion for safe and durable wearable batteries. *Nano Energy* **48**, 569–574 (2018).
32. Zhou, Y. *et al.* Biocompatible and flexible hydrogel diode-based mechanical energy harvesting. *Adv. Mater. Technol.* **2**, 1700118 (2017).
33. Zhang, Y. *et al.* Hydrogel ionic diodes toward harvesting ultralow-frequency mechanical energy. *Adv. Mater.* **33**, 2103056 (2021).
34. Han, S. H., Kwon, S. R., Baek, S. & Chung, T. D. Ionic circuits powered by reverse electrodialysis for an ultimate iontronic system. *Sci. Rep.* **7**, 1–7 (2017).
35. Hou, Y. *et al.* Flexible ionic diodes for low-frequency mechanical energy harvesting. *Adv. Energy Mater.* **7**, 1601983 (2017).
36. Lim, S. M. *et al.* Ion-to-ion amplification through an open-junction ionic diode. *Proc. Natl. Acad. Sci. U. S. A.* **116**, 13807–13815 (2019).
37. Sjöström, T. A. *et al.* Miniaturized ionic polarization diodes for neurotransmitter release at synaptic speeds. *Adv. Mater. Technol.* **5**, 1–7 (2020).
38. Kim, H. J. *et al.* Low-voltage reversible electroadhesion of ionoelastomer junctions. *Adv. Mater.* **32**, 1–7 (2020).
39. Ge, G., Wang, Q., Zhang, Y.-Z., Alshareef, H. N. & Dong, X. 3D printing of hydrogels for stretchable ionotronic devices. *Adv. Funct. Mater.* **31**, 2107437 (2021).
40. Chen, Z. *et al.* 3D printing of multifunctional hydrogels. *Adv. Funct. Mater.* **29**, 1–8 (2019).
41. Bao, G. *et al.* Triggered micropore-forming bioprinting of porous viscoelastic hydrogels. *Mater. Horizons* **7**, 2336–2347 (2020).
42. Cheng, J. *et al.* Centrifugal multimaterial 3D printing of multifunctional heterogeneous objects. *Nat. Commun.* **13**, 7931 (2022).
43. Li, J., Wu, C., Chu, P. K. & Gelinsky, M. 3D printing of hydrogels: Rational design strategies and emerging biomedical applications. *Mater. Sci. Eng. R Reports* **140**, 100543 (2020).
44. Ravanbakhsh, H., Bao, G., Luo, Z., Mongeau, L. G. & Zhang, Y. S. Composite inks for extrusion printing of biological and biomedical constructs. *ACS Biomater. Sci. Eng.* **7**, 4009–4026 (2021).
45. Ravanbakhsh, H. *et al.* Emerging technologies in multi-material bioprinting. *Adv. Mater.*

33, 2104730 (2021).

46. Yang, H. *et al.* Printing hydrogels and elastomers in arbitrary sequence with strong adhesion. *Adv. Funct. Mater.* **29**, 1–8 (2019).
47. Liu, X., Liu, J., Lin, S. & Zhao, X. Hydrogel machines. *Mater. Today* **36**, 102–124 (2020).
48. Zhang, Y. S. & Khademhosseini, A. Advances in engineering hydrogels. *Science* **356**, (2017).
49. Zheng, Z. *et al.* Ionic shape-morphing microrobotic end-effectors for environmentally adaptive targeting, releasing, and sampling. *Nat. Commun.* **12**, 1–12 (2021).
50. Li, J. *et al.* Tough adhesives for diverse wet surfaces. *Science* **357**, 378–381 (2017).
51. Keplinger, C. *et al.* Stretchable, transparent, ionic conductors. *Science* **341**, 984–987 (2013).
52. Yuk, H., Lu, B. & Zhao, X. Hydrogel bioelectronics. *Chem. Soc. Rev.* **48**, 1642–1667 (2019).
53. Lee, Y., Song, W. J. & Sun, J.-Y. Hydrogel soft robotics. *Mater. Today Phys.* **15**, 100258 (2020).
54. Yang, C. Perspectives on the fundamental principles and manufacturing of stretchable ionotronics. *Appl. Phys. Lett.* **122**, 70501 (2023).
55. Liang, X. *et al.* Preparation of cellulose-based conductive hydrogels with ionic liquid. *React. Funct. Polym.* **86**, 1–6 (2015).
56. Dispenza, C., Presti, C. Lo, Belfiore, C., Spadaro, G. & Piazza, S. Electrically conductive hydrogel composites made of polyaniline nanoparticles and poly(N-vinyl-2-pyrrolidone). *Polymer (Guildf).* **47**, 961–971 (2006).
57. Ohm, Y. *et al.* An electrically conductive silver–polyacrylamide–alginate hydrogel composite for soft electronics. *Nat. Electron.* **4**, 185–192 (2021).
58. Gniadek, M. *et al.* Construction of multifunctional materials by intrachannel modification of NIPA hydrogel with PANI-metal composites. *J. Electroanal. Chem.* **812**, 273–281 (2018).
59. Cai, G. *et al.* Extremely stretchable strain sensors based on conductive self-healing dynamic cross-links hydrogels for human-motion detection. *Adv. Sci.* **4**, 1600190 (2017).
60. Mottet, L. *et al.* A conductive hydrogel based on alginate and carbon nanotubes for probing microbial electroactivity. *Soft Matter* **14**, 1434–1441 (2018).
61. Liu, X. W. *et al.* Conductive carbon nanotube hydrogel as a bioanode for enhanced microbial electrocatalysis. *ACS Appl. Mater. Interfaces* **6**, 8158–8164 (2014).

62. Chuang, W. J., Chiu, W. Y. & Tai, H. J. Temperature-dependent conductive composites: Poly(N-isopropylacrylamide-co- N-methylol acrylamide) and carbon black composite films. *J. Mater. Chem.* **22**, 20311–20318 (2012).

63. Peng, R., Yu, Y., Chen, S., Yang, Y. & Tang, Y. Conductive nanocomposite hydrogels with self-healing property. *RSC Adv.* **4**, 35149–35155 (2014).

64. Liu, X. *et al.* Functionalized carbon nanotube and graphene oxide embedded electrically conductive hydrogel synergistically stimulates nerve cell differentiation. *ACS Appl. Mater. Interfaces* **9**, 14677–14690 (2017).

65. Han, L. *et al.* A mussel-inspired conductive, self-adhesive, and self-healable tough hydrogel as cell stimulators and implantable bioelectronics. *Small* **13**, 1601916 (2017).

66. Qu, B., Li, J. rong, Xiao, H. ning, He, B. hai & Qian, L. ying. Facile preparation and characterization of sodium alginate/graphite conductive composite hydrogel. *Polym. Compos.* **37**, 3050–3056 (2016).

67. Paulsen, B. D., Tybrandt, K., Stavrinidou, E. & Rivnay, J. Organic mixed ionic–electronic conductors. *Nat. Mater.* **19**, 13–26 (2020).

68. Lu, B. *et al.* Pure PEDOT:PSS hydrogels. *Nat. Commun.* **10**, (2019).

69. Zhou, T. *et al.* 3D printable high-performance conducting polymer hydrogel for all-hydrogel bioelectronic interfaces. *Nat. Mater.* **22**, 895–902 (2023).

70. Taylor, D. L. & in het Panhuis, M. Self-healing hydrogels. *Adv. Mater.* **28**, 9060–9093 (2016).

71. Deng, Z., Wang, H., Ma, P. X. & Guo, B. Self-healing conductive hydrogels: Preparation, properties and applications. *Nanoscale* **12**, 1224–1246 (2020).

72. Hur, J. *et al.* Polypyrrole/agarose-based electronically conductive and reversibly restorable hydrogel. *ACS Nano* **8**, 10066–10076 (2014).

73. Zhu, D. Y., Rong, M. Z. & Zhang, M. Q. Self-healing polymeric materials based on microencapsulated healing agents: From design to preparation. *Prog. Polym. Sci.* **49–50**, 175–220 (2015).

74. Ge, G. *et al.* Highly stretchable and autonomously healable epidermal sensor based on multi-functional hydrogel frameworks. *J. Mater. Chem. A* **7**, 5949–5956 (2019).

75. van der Kooij, H. M., Susa, A., García, S. J., van der Zwaag, S. & Sprakel, J. Imaging the molecular motions of autonomous repair in a self-healing polymer. *Adv. Mater.* **29**, 1701017

(2017).

76. Gačanin, J. *et al.* Autonomous ultrafast self-healing hydrogels by ph-responsive functional nanofiber gelators as cell matrices. *Adv. Mater.* **31**, 1805044 (2019).

77. Yu, H., Wang, Y., Yang, H., Peng, K. & Zhang, X. Injectable self-healing hydrogels formed via thiol/disulfide exchange of thiol functionalized F127 and dithiolane modified PEG. *J. Mater. Chem. B* **5**, 4121–4127 (2017).

78. Yang, W. J. *et al.* Antifouling and antibacterial hydrogel coatings with self-healing properties based on a dynamic disulfide exchange reaction. *Polym. Chem.* **6**, 7027–7035 (2015).

79. Apostolides, D. E., Sakai, T. & Patrickios, C. S. Dynamic covalent star poly(ethylene glycol) model hydrogels: a new platform for mechanically robust, multifunctional materials. *Macromolecules* **50**, 2155–2164 (2017).

80. Shan, M., Gong, C., Li, B. & Wu, G. A pH, glucose, and dopamine triple-responsive, self-healable adhesive hydrogel formed by phenylborate-catechol complexation. *Polym. Chem.* **8**, 2997–3005 (2017).

81. Liao, M. *et al.* Wearable, healable, and adhesive epidermal sensors assembled from mussel-inspired conductive hybrid hydrogel framework. *Adv. Funct. Mater.* **27**, 1703852 (2017).

82. Yu, F., Cao, X., Du, J., Wang, G. & Chen, X. Multifunctional hydrogel with good structure integrity, self-healing, and tissue-adhesive property formed by combining diels-alder click reaction and acylhydrazone bond. *ACS Appl. Mater. Interfaces* **7**, 24023–24031 (2015).

83. Karimi, A. R. & Khodadadi, A. Mechanically robust 3d nanostructure chitosan-based hydrogels with autonomic self-healing properties. *ACS Appl. Mater. Interfaces* **8**, 27254–27263 (2016).

84. Wei, Z. *et al.* Novel biocompatible polysaccharide-based self-healing hydrogel. *Adv. Funct. Mater.* **25**, 1352–1359 (2015).

85. Zhang, J. *et al.* Highly stretchable and self-healable mxene/polyvinyl alcohol hydrogel electrode for wearable capacitive electronic skin. *Adv. Electron. Mater.* **5**, 1900285 (2019).

86. Bao, G. *et al.* Ionotronic tough adhesives with intrinsic multifunctionality. *ACS Appl. Mater. Interfaces* **13**, 37849–37861 (2021).

87. Ye, X. *et al.* Self-healing pH-sensitive cytosine- and guanosine-modified hyaluronic acid hydrogels via hydrogen bonding. *Polymer (Guildf).* **108**, 348–360 (2017).

88. Rao, V. K. *et al.* Polydiacetylene hydrogel self-healing capacitive strain sensor. *J. Mater. Chem. C* **8**, 6034–6041 (2020).

89. Li, Y. *et al.* Triterpenoid-based self-healing supramolecular polymer hydrogels formed by host–guest interactions. *Chem. – A Eur. J.* **22**, 18435–18441 (2016).

90. Deng, Z., Guo, Y., Zhao, X., Ma, P. X. & Guo, B. Multifunctional stimuli-responsive hydrogels with self-healing, high conductivity, and rapid recovery through host-guest interactions. *Chem. Mater.* **30**, 1729–1742 (2018).

91. Cui, W., Ji, J., Cai, Y. F., Li, H. & Ran, R. Robust, anti-fatigue, and self-healing graphene oxide/hydrophobically associated composite hydrogels and their use as recyclable adsorbents for dye wastewater treatment. *J. Mater. Chem. A* **3**, 17445–17458 (2015).

92. Gregorova, A., Saha, N., Kitano, T. & Saha, P. Hydrothermal effect and mechanical stress properties of carboxymethylcellulose based hydrogel food packaging. *Carbohydr. Polym.* **117**, 559–568 (2015).

93. Kabiri, K., Zohuriaan-Mehr, M. J., Mirzadeh, H. & Kheirabadi, M. Solvent-, ion- and pH-specific swelling of poly(2-acrylamido-2- methylpropane sulfonic acid) superabsorbing gels. *J. Polym. Res.* **17**, 203–212 (2010).

94. Morelle, X. P. *et al.* Highly stretchable and tough hydrogels below water freezing temperature. *Adv. Mater.* **30**, 1801541 (2018).

95. Bai, Y. *et al.* Transparent hydrogel with enhanced water retention capacity by introducing highly hydratable salt. *Appl. Phys. Lett.* **105**, 151903 (2014).

96. Yang, Y. *et al.* Conductive organohydrogels with ultrastretchability, antifreezing, self-healing, and adhesive properties for motion detection and signal transmission. *ACS Appl. Mater. Interfaces* **11**, 3428–3437 (2019).

97. Chen, F. *et al.* Rational fabrication of anti-freezing, non-drying tough organohydrogels by one-pot solvent displacement. *Angew. Chemie* **130**, 6678–6681 (2018).

98. Tian, K. *et al.* 3D printing of transparent and conductive heterogeneous hydrogel–elastomer systems. *Adv. Mater.* **29**, (2017).

99. Cheng, S., Narang, Y. S., Yang, C., Suo, Z. & Howe, R. D. Stick-on large-strain sensors for soft robots. *Adv. Mater. Interfaces* **6**, 1–11 (2019).

100. Yuk, H., Zhang, T., Parada, G. A., Liu, X. & Zhao, X. Skin-inspired hydrogel–elastomer hybrids with robust interfaces and functional microstructures. *Nat. Commun.* **7**, 12028

(2016).

101. Yu, Y. *et al.* Multifunctional “hydrogel skins” on diverse polymers with arbitrary shapes. *Adv. Mater.* **31**, 1807101 (2019).

102. Rogers, J. A. Integrated nanoelectronic-photonic devices and bioresorbable materials. *Nano Res.* **14**, 2885–2887 (2021).

103. Hwang, H. H., Zhu, W., Victorine, G., Lawrence, N. & Chen, S. 3D-printing of functional biomedical microdevices via light- and extrusion-based approaches. *Small Methods* **2**, 1700277 (2018).

104. Bakarich, S. E., Panhuis, M. In Het, Beirne, S., Wallace, G. G. & Spinks, G. M. Extrusion printing of ionic–covalent entanglement hydrogels with high toughness. *J. Mater. Chem. B* **1**, 4939 (2013).

105. Wei, J. *et al.* 3D printing of an extremely tough hydrogel. *RSC Adv.* **5**, 81324–81329 (2015).

106. Du, C. *et al.* 3D printing of a tough double-network hydrogel and its use as a scaffold to construct a tissue-like hydrogel composite. *J. Mater. Chem. B* **10**, 468–476 (2022).

107. Dong, M. *et al.* Digital light processing 3D printing of tough supramolecular hydrogels with sophisticated architectures as impact-absorption elements. *Adv. Mater.* **34**, 2204333 (2022).

108. Zheng, S. Y. *et al.* Programmed deformations of 3d-printed tough physical hydrogels with high response speed and large output force. *Adv. Funct. Mater.* **28**, 1803366 (2018).

109. Yang, F., Tadepalli, V. & Wiley, B. J. 3D printing of a double network hydrogel with a compression strength and elastic modulus greater than those of cartilage. *ACS Biomater. Sci. Eng.* **3**, 863–869 (2017).

110. Hirsch, M., Charlet, A. & Amstad, E. 3D Printing of strong and tough double network granular hydrogels. *Adv. Funct. Mater.* **31**, (2021).

111. Tang, J. *et al.* 3D printable, tough, magnetic hydrogels with programmed magnetization for fast actuation. *J. Mater. Chem. B* **9**, 9183–9190 (2021).

112. Zhao, D. *et al.* 3D printing method for tough multifunctional particle-based double-network hydrogels. *ACS Appl. Mater. Interfaces* **13**, 13714–13723 (2021).

113. Hong, S. *et al.* 3D printing of highly stretchable and tough hydrogels into complex, cellularized structures. *Adv. Mater.* **27**, 4035–4040 (2015).

114. Jiang, P. *et al.* 3D printing of dual-physical cross-linking hydrogel with ultrahigh strength and toughness. *Chem. Mater.* **32**, 9983–9995 (2020).

115. Zhu, F. *et al.* 3D printing of ultratough polyion complex hydrogels. *ACS Appl. Mater. Interfaces* **8**, 31304–31310 (2016).

116. Zhu, F. *et al.* Processing tough supramolecular hydrogels with tunable strength of polyion complex. *Polymer (Guildf).* **95**, 9–17 (2016).

117. Cui, H. *et al.* Direct 3D printing of a tough hydrogel incorporated with carbon nanotubes for bone regeneration. *J. Mater. Chem. B* **7**, 7207–7217 (2019).

118. Sun, J. Y., Keplinger, C., Whitesides, G. M. & Suo, Z. Ionic skin. *Adv. Mater.* **26**, 7608–7614 (2014).

119. Yang, C. H. *et al.* Ionic cable. *Extrem. Mech. Lett.* **3**, 59–65 (2015).

120. Schroeder, T. B. H. *et al.* An electric-eel-inspired soft power source from stacked hydrogels. *Nature* **552**, 214–218 (2017).

121. Yang, C. *et al.* Ionotronic luminescent fibers, fabrics, and other configurations. *Adv. Mater.* **32**, 2005545 (2020).

122. Wang, Y. *et al.* Temperature sensing using junctions between mobile ions and mobile electrons. *Proc. Natl. Acad. Sci. U. S. A.* **119**, e2117962119 (2022).

123. Sheng, H. *et al.* Neural interfaces by hydrogels. *Extrem. Mech. Lett.* **30**, 100510 (2019).

124. Yang, Q. *et al.* Photocurable bioresorbable adhesives as functional interfaces between flexible bioelectronic devices and soft biological tissues. *Nat. Mater.* **20**, 1559–1570 (2021).

125. Chen, B. & Suo, Z. Optoionic sensing. *Small* **18**, 2103882 (2022).

126. Chen, B. *et al.* All-solid ionic eye. *J. Appl. Mech. Trans. ASME* **88**, (2021).

127. Jin, Z., Zhao, F., Lei, Y. & Wang, Y. C. Hydrogel-based triboelectric devices for energy-harvesting and wearable sensing applications. *Nano Energy* **95**, 106988 (2022).

128. Ying, B., Zuo, R., Wan, Y. & Liu, X. An ionic hydrogel-based antifreezing triboelectric nanogenerator. *ACS Appl. Electron. Mater.* **4**, 1930–1938 (2022).

129. Lu, N., Lu, C., Yang, S. & Rogers, J. Highly sensitive skin-mountable strain gauges based entirely on elastomers. *Adv. Funct. Mater.* **22**, 4044–4050 (2012).

130. Sadasivuni, K. K. *et al.* Reduced graphene oxide filled cellulose films for flexible temperature sensor application. *Synth. Met.* **206**, 154–161 (2015).

131. Yang, J. *et al.* Wearable temperature sensor based on graphene nanowalls. *RSC Adv.* **5**, 25609–25615 (2015).

132. Oh, Y. S. *et al.* Battery-free, wireless soft sensors for continuous multi-site measurements

of pressure and temperature from patients at risk for pressure injuries. *Nat. Commun.* **12**, 1–16 (2021).

133. Bai, W. *et al.* Bioresorbable multilayer photonic cavities as temporary implants for tether-free measurements of regional tissue temperatures. *BME Front.* **2021**, 1–14 (2021).
134. Li, Q., Zhang, L., Tao, X. & Ding, X. Review of flexible temperature sensing networks for wearable physiological monitoring. *Adv. Healthc. Mater.* **6**, 1601371 (2017).
135. Shi, Y., Ma, C., Peng, L. & Yu, G. Conductive “smart” hybrid hydrogels with PNIPAM and nanostructured conductive polymers. *Adv. Funct. Mater.* **25**, 1219–1225 (2015).
136. Wang, Y. Hydrogel interface. (Harvard University, 2019).
137. Niu, S. & Wang, Z. L. Theoretical systems of triboelectric nanogenerators. *Nano Energy* **14**, 161–192 (2014).
138. Tat, T., Libanori, A., Au, C., Yau, A. & Chen, J. Advances in triboelectric nanogenerators for biomedical sensing. *Biosens. Bioelectron.* **171**, 112714 (2021).
139. Zheng, Q. *et al.* In vivo powering of pacemaker by breathing-driven implanted triboelectric nanogenerator. *Adv. Mater.* **26**, 5851–5856 (2014).
140. Ouyang, H. *et al.* Symbiotic cardiac pacemaker. *Nat. Commun.* **10**, 1–10 (2019).
141. Jeong, S. H. *et al.* Accelerated wound healing with an ionic patch assisted by a triboelectric nanogenerator. *Nano Energy* **79**, 105463 (2021).
142. Tang, W. *et al.* Implantable self-powered low-level laser cure system for mouse embryonic osteoblasts’ proliferation and differentiation. *ACS Nano* **9**, 7867–7873 (2015).
143. Tian, J. *et al.* Self-powered implantable electrical stimulator for osteoblasts’ proliferation and differentiation. *Nano Energy* **59**, 705–714 (2019).
144. Lee, S. *et al.* Development of battery-free neural interface and modulated control of tibialis anterior muscle via common peroneal nerve based on triboelectric nanogenerators (TENGs). *Nano Energy* **33**, 1–11 (2017).
145. Yao, G. *et al.* Effective weight control via an implanted self-powered vagus nerve stimulation device. *Nat. Commun.* **9**, 1–10 (2018).
146. Zheng, Q. *et al.* Biodegradable triboelectric nanogenerator as a life-time designed implantable power source. *Sci. Adv.* **2**, (2016).
147. Guan, H. *et al.* Self-powered, wireless-control, neural-stimulating electronic skin for in vivo characterization of synaptic plasticity. *Nano Energy* **67**, 104182 (2020).

148. Bai, P. *et al.* Membrane-based self-powered triboelectric sensors for pressure change detection and its uses in security surveillance and healthcare monitoring. *Adv. Funct. Mater.* **24**, 5807–5813 (2014).
149. Zheng, Q. *et al.* In vivo self-powered wireless cardiac monitoring via implantable triboelectric nanogenerator. *ACS Nano* **10**, 6510–6518 (2016).
150. Ma, Y. *et al.* Self-powered, one-stop, and multifunctional implantable triboelectric active sensor for real-time biomedical monitoring. *Nano Lett.* **16**, 6042–6051 (2016).
151. Ouyang, H. *et al.* Self-powered pulse sensor for antidiastole of cardiovascular disease. *Adv. Mater.* **29**, 1703456 (2017).
152. Zhao, Z. *et al.* Machine-washable textile triboelectric nanogenerators for effective human respiratory monitoring through loom weaving of metallic yarns. *Adv. Mater.* **28**, 10267–10274 (2016).
153. Jang, J., Lee, J., Jang, J. H. & Choi, H. A triboelectric-based artificial basilar membrane to mimic cochlear tonotopy. *Adv. Healthc. Mater.* **5**, 2481–2487 (2016).
154. Guo, H. *et al.* A highly sensitive, self-powered triboelectric auditory sensor for social robotics and hearing AIDS. *Sci. Robot.* **3**, (2018).
155. Wang, S. *et al.* Stretchable and wearable triboelectric nanogenerator based on kinesio tape for self-powered human motion sensing. *Nanomaterials* **8**, (2018).
156. Pu, X. *et al.* Rotation sensing and gesture control of a robot joint via triboelectric quantization sensor. *Nano Energy* **54**, 453–460 (2018).
157. Pu, X. *et al.* Ultrastretchable, transparent triboelectric nanogenerator as electronic skin for biomechanical energy harvesting and tactile sensing. *Sci. Adv.* **3**, (2017).
158. Liu, T. *et al.* Triboelectric-nanogenerator-based soft energy-harvesting skin enabled by toughly bonded elastomer/hydrogel hybrids. *ACS Nano* **12**, 2818–2826 (2018).
159. Someya, T., Bao, Z. & Malliaras, G. G. The rise of plastic bioelectronics. *Nature* vol. 540 379–385 (2016).
160. Feiner, R. & Dvir, T. Tissue–electronics interfaces: from implantable devices to engineered tissues. *Nat. Rev. Mater.* **3**, 17076 (2017).
161. Deng, J. *et al.* Electrical bioadhesive interface for bioelectronics. *Nat. Mater.* **20**, 229–236 (2021).
162. Wang, C. *et al.* Bioadhesive ultrasound for long-term continuous imaging of diverse organs.

Science **377**, 517–523 (2022).

163. Yang, Q., Hu, Z. & Rogers, J. A. Functional hydrogel interface materials for advanced bioelectronic devices. *Accounts Mater. Res.* **2**, 1010–1023 (2021).
164. Kim, H. J. *et al.* Biological assessments of multifunctional hydrogel-decorated implantable neural cuff electrode for clinical neurology application. *Sci. Rep.* **7**, 1–14 (2017).
165. Liu, J. *et al.* Intrinsically stretchable electrode array enabled in vivo electrophysiological mapping of atrial fibrillation at cellular resolution. *Proc. Natl. Acad. Sci. U. S. A.* **117**, 14769–14778 (2020).
166. Oribe, S. *et al.* Hydrogel-based organic subdural electrode with high conformability to brain surface. *Sci. Rep.* **9**, 13379 (2019).
167. Kaur, S., Weerasekare, G. M. & Stewart, R. J. Multiphase adhesive coacervates inspired by the sandcastle worm. *ACS Appl. Mater. Interfaces* **3**, 941–944 (2011).
168. Stewart, R. J., Wang, C. S., Song, I. T. & Jones, J. P. The role of coacervation and phase transitions in the sandcastle worm adhesive system. *Adv. Colloid Interface Sci.* **239**, 88–96 (2017).
169. Jones, J. P., Sima, M., O'Hara, R. G. & Stewart, R. J. Water-borne endovascular embolics inspired by the undersea adhesive of marine sandcastle worms. *Adv. Healthc. Mater.* **5**, 795–801 (2016).
170. Shao, H. & Stewart, R. J. Biomimetic underwater adhesives with environmentally triggered setting mechanisms. *Adv. Mater.* **22**, 729–733 (2010).
171. Yin, X.-Y. *et al.* 3D printing of ionic conductors for high-sensitivity wearable sensors. *Mater. Horizons* **6**, 767–780 (2019).
172. Chen, J., Huang, J. & Hu, Y. 3D printing of biocompatible shape-memory double network hydrogels. *ACS Appl. Mater. Interfaces* **13**, 12726–12734 (2021).
173. Wang, C., Yan, Q., Liu, H. B., Zhou, X. H. & Xiao, S. J. Different EDC/NHS activation mechanisms between PAA and PMAA brushes and the following amidation reactions. *Langmuir* **27**, 12058–12068 (2011).
174. Lake & Thomas. The strength of highly elastic materials. *Proc. R. Soc. London. Ser. A. Math. Phys. Sci.* **300**, 108–119 (1967).
175. Wu, J. *et al.* An off-the-shelf bioadhesive patch for sutureless repair of gastrointestinal defects. *Sci. Transl. Med.* **14**, 1–37 (2022).

176. Wu, S. J., Yuk, H., Wu, J., Nabzdyk, C. S. & Zhao, X. A multifunctional origami patch for minimally invasive tissue sealing. *Adv. Mater.* **33**, 1–10 (2021).

177. Blacklow, S. O. *et al.* Bioinspired mechanically active adhesive dressings to accelerate wound closure. *Sci. Adv.* **5**, 1–10 (2019).

178. Fan, H., Wang, J. & Gong, J. P. Barnacle Cement Proteins-Inspired Tough Hydrogels with Robust, Long-Lasting, and Repeatable Underwater Adhesion. *Adv. Funct. Mater.* **31**, 1–8 (2021).

179. Zhao, Q. *et al.* Underwater contact adhesion and microarchitecture in polyelectrolyte complexes actuated by solvent exchange. *Nat. Mater.* **15**, 407–412 (2016).

180. Dompé, M. *et al.* Thermoresponsive Complex Coacervate-Based Underwater Adhesive. *Adv. Mater.* **31**, 1808179 (2019).

181. Dompé, M. *et al.* Underwater Adhesion of Multiresponsive Complex Coacervates. *Adv. Mater. Interfaces* **7**, 1901785 (2020).

182. Yuk, H. *et al.* 3D printing of conducting polymers. *Nat. Commun.* **11**, 4–11 (2020).

183. Yang, Z. *et al.* Programming hydrogel adhesion with engineered polymer network topology. *Proc. Natl. Acad. Sci.* **120**, e2307816120 (2023).

184. Li, J. & Mooney, D. J. Designing hydrogels for controlled drug delivery. *Nat. Rev. Mater.* **1**, 16071 (2016).

185. Dong, Y. *et al.* 4D printed hydrogels: fabrication, materials, and applications. *Adv. Mater. Technol.* **5**, 2000034 (2020).

186. Champeau, M. *et al.* 4D printing of hydrogels: a review. *Adv. Funct. Mater.* **30**, 1910606 (2020).

187. Sydney Gladman, A., Matsumoto, E. A., Nuzzo, R. G., Mahadevan, L. & Lewis, J. A. Biomimetic 4D printing. *Nat. Mater.* **15**, 413–418 (2016).

188. Highley, C. B., Song, K. H., Daly, A. C. & Burdick, J. A. Jammed microgel inks for 3D printing applications. *Adv. Sci.* **6**, (2019).

189. Arnott, S. *et al.* The agarose double helix and its function in agarose gel structure. *J. Mol. Biol.* **90**, 269–284 (1974).

190. Chen, Q., Zhu, L., Zhao, C., Wang, Q. & Zheng, J. A robust, one-pot synthesis of highly mechanical and recoverable double network hydrogels using thermoreversible sol-gel polysaccharide. *Adv. Mater.* **25**, 4171–4176 (2013).

191. Daly, A. C., Riley, L., Segura, T. & Burdick, J. A. Hydrogel microparticles for biomedical applications. *Nat. Rev. Mater.* **5**, 20–43 (2019).

192. Muir, V. G., Qazi, T. H., Shan, J., Groll, J. & Burdick, J. A. Influence of microgel fabrication technique on granular hydrogel properties. *ACS Biomater. Sci. Eng.* **7**, 4269–4281 (2021).

193. Han, J., Kim, K. B., Kim, H. C. & Chung, T. D. Ionic circuits based on polyelectrolyte diodes on a microchip. *Angew. Chemie* **121**, 3888–3891 (2009).

194. Ding, Y. & Zheng, Z. Stretchable ionics: How to measure the electrical resistance/impedance. *Matter* **5**, 2570–2573 (2022).

195. Peng, Q. *et al.* Recent advances in designing conductive hydrogels for flexible electronics. *InfoMat* **2**, 843–865 (2020).

196. Lee, C.-J. *et al.* Ionic conductivity of polyelectrolyte hydrogels. *ACS Appl. Mater. Interfaces* **10**, 5845–5852 (2018).

197. Yamamoto, T. & Doi, M. Electrochemical mechanism of ion current rectification of polyelectrolyte gel diodes. *Nat. Commun.* **5**, 4162 (2014).

198. Nyamayaro, K. *et al.* The rectification mechanism in polyelectrolyte gel diodes. *Phys. Fluids* **33**, (2021).

199. Kim, H. J., Chen, B., Suo, Z. & Hayward, R. C. Ionoelastomer junctions between polymer networ of fixed anions and cations. *Science* **367**, 773–776 (2020).

200. Triandafilidi, V., Hatzikiriakos, S. G. & Rottler, J. Poisson-Boltzmann modeling and molecular dynamics simulations of polyelectrolyte gel diodes in the static regime. *Soft Matter* **16**, 1091–1101 (2020).

201. Qazi, T. H., Muir, V. G. & Burdick, J. A. Methods to characterize granular hydrogel rheological properties, porosity, and cell invasion. *ACS Biomater. Sci. Eng.* **8**, 1427–1442 (2022).

202. Cayre, O. J., Suk, T. C. & Velev, O. D. Polyelectrolyte diode: Nonlinear current response of a junction between aqueous ionic gels. *J. Am. Chem. Soc.* **129**, 10801–10806 (2007).

203. Gabrielsson, E. O., Janson, P., Tybrandt, K., Simon, D. T. & Berggren, M. A four-diode full-wave ionic current rectifier based on bipolar membranes: Overcoming the limit of electrode capacity. *Adv. Mater.* **26**, 5143–5147 (2014).

204. Bao, B. *et al.* 3D porous hydrogel/conducting polymer heterogeneous membranes with

electro-/ph-modulated ionic rectification. *Adv. Mater.* **29**, 1–7 (2017).

205. Han, S. H. *et al.* Hydrogel-based iontronics on a polydimethylsiloxane microchip. *ACS Appl. Mater. Interfaces* **13**, 6606–6614 (2021).

206. Ding, Y., Cai, P. & Wen, Z. Electrochemical neutralization energy: from concept to devices. *Chem. Soc. Rev.* **50**, 1495–1511 (2021).

207. Dobashi, Y. *et al.* Piezoionic mechanoreceptors: Force-induced current generation in hydrogels. *Science* **376**, 502–507 (2022).

208. Brug, G. J., van den Eeden, A. L. G., Sluyters-Rehbach, M. & Sluyters, J. H. The analysis of electrode impedances complicated by the presence of a constant phase element. *J. Electroanal. Chem.* **176**, 275–295 (1984).

209. Muthukumar, M. *Polymer translocation*. *CRC press* (CRC Press, 2016). doi:10.1201/b10901.

210. Hutchinson, J. W. & Suo, Z. Mixed mode cracking in layered materials. in *Advances in Applied Mechanics* vol. 29 63–191 (Elsevier, 1991).

211. Hu, J. *et al.* Microgel-reinforced hydrogel films with high mechanical strength and their visible mesoscale fracture structure. *Macromolecules* **44**, 7775–7781 (2011).

212. Jiang, C., Liu, Z., Cheng, D. & Mao, X. Agarose degradation for utilization: Enzymes, pathways, metabolic engineering methods and products. *Biotechnol. Adv.* **45**, 107641 (2020).

213. Li, X. *et al.* Immunostimulatory effect of chitosan and quaternary chitosan: A review of potential vaccine adjuvants. *Carbohydr. Polym.* **264**, 118050 (2021).

214. Wang, K. *et al.* Degradation of chondroitin sulfate: Mechanism of degradation, influence factors, structure-bioactivity relationship and application. *Carbohydr. Polym.* **301**, 120361 (2023).

215. Freedman, B. R. *et al.* Degradable and removable tough adhesive hydrogels. *Adv. Mater.* **33**, 2008553 (2021).

216. Tybrandt, K., Larsson, K. C., Richter-Dahlfors, A. & Berggren, M. Ion bipolar junction transistors. *Proc. Natl. Acad. Sci. U. S. A.* **107**, 9929–9932 (2010).

217. Wu, Y. *et al.* Hydrogels as soft ionic conductors in flexible and wearable triboelectric nanogenerators. *Adv. Sci.* **9**, 2106008 (2022).

218. Parida, K. *et al.* Highly transparent, stretchable, and self-healing ionic-skin triboelectric

nanogenerators for energy harvesting and touch applications. *Adv. Mater.* **29**, 1702181 (2017).

219. Wu, C., Wang, A. C., Ding, W., Guo, H. & Wang, Z. L. Triboelectric nanogenerator: a foundation of the energy for the new era. *Adv. Energy Mater.* **9**, 1802906 (2019).
220. Zhou, L., Liu, D., Wang, J. & Wang, Z. L. Triboelectric nanogenerators: Fundamental physics and potential applications. *Frict. 2020 83* **8**, 481–506 (2020).
221. Paxton, N. *et al.* Proposal to assess printability of bioinks for extrusion-based bioprinting and evaluation of rheological properties governing bioprintability. *Biofabrication* **9**, 044107 (2017).
222. Compton, B. G. & Lewis, J. A. 3D-printing of lightweight cellular composites. *Adv. Mater.* **26**, 5930–5935 (2014).
223. Farahani, R. D., Dubé, M. & Therriault, D. Three-dimensional printing of multifunctional nanocomposites: manufacturing techniques and applications. *Adv. Mater.* **28**, 5794–5821 (2016).
224. Chin, S. M. *et al.* Covalent-supramolecular hybrid polymers as muscle-inspired anisotropic actuators. *Nat. Commun.* **9**, 1–11 (2018).
225. Hausmann, M. K. *et al.* Dynamics of cellulose nanocrystal alignment during 3D printing. *ACS Nano* **12**, 6926–6937 (2018).
226. Ouyang, L., Highley, C. B., Sun, W. & Burdick, J. A. A generalizable strategy for the 3D bioprinting of hydrogels from nonviscous photo-crosslinkable inks. *Adv. Mater.* **29**, 1604983 (2017).
227. Wu, W., Deconinck, A. & Lewis, J. A. Omnidirectional printing of 3D microvascular networks. *Adv. Mater.* **23**, (2011).
228. Zhao, J. & He, N. A mini-review of embedded 3D printing: supporting media and strategies. *J. Mater. Chem. B* **8**, 10474–10486 (2020).
229. Colosi, C. *et al.* Microfluidic bioprinting of heterogeneous 3D tissue constructs using low-viscosity bioink. *Adv. Mater.* **28**, 677–684 (2016).
230. Mirani, B., Stefanek, E., Godau, B., Hossein Dabiri, S. M. & Akbari, M. Microfluidic 3D printing of a photo-cross-linkable bioink using insights from computational modeling. *ACS Biomater. Sci. Eng.* **7**, 3269–3280 (2021).
231. Uman, S., Dhand, A. & Burdick, J. A. Recent advances in shear-thinning and self-healing

hydrogels for biomedical applications. *J. Appl. Polym. Sci.* **137**, 48668 (2020).

232. Chhabra, R. P. Non-Newtonian Fluids: An Introduction. in *Rheology of Complex Fluids* 3–34 (Springer New York, 2010). doi:10.1007/978-1-4419-6494-6_1.

233. Shaw, M. T. *Introduction to Polymer Rheology*. *Introduction to Polymer Rheology* (Wiley, 2011). doi:10.1002/9781118170229.

234. Riley, L., Schirmer, L. & Segura, T. Granular hydrogels: emergent properties of jammed hydrogel microparticles and their applications in tissue repair and regeneration. *Curr. Opin. Biotechnol.* **60**, 1–8 (2019).

235. Cheng, W., Zhang, J., Liu, J. & Yu, Z. Granular hydrogels for 3D bioprinting applications. *VIEW* **1**, 20200060 (2020).

236. Goldhirsch, I. Mesoscopic nature of granular flows. in *Handbook of Powder Technology* vol. 10 245–253 (Elsevier Science B.V., 2001).

237. Liu, A. J. & Nagel, S. R. Granular and jammed materials. *Soft Matter* **6**, 2869–2870 (2010).

238. Guvendiren, M., Lu, H. D. & Burdick, J. A. Shear-thinning hydrogels for biomedical applications. *Soft Matter* **8**, 260–272 (2012).

239. Pusch, K., Hinton, T. J. & Feinberg, A. W. Large volume syringe pump extruder for desktop 3D printers. *HardwareX* **3**, 49–61 (2018).

240. Tashman, J. W., Shiwarski, D. J. & Feinberg, A. W. A high performance open-source syringe extruder optimized for extrusion and retraction during FRESH 3D bioprinting. *HardwareX* **9**, e00170 (2021).

241. Zhang, X. N., Zheng, Q. & Wu, Z. L. Recent advances in 3D printing of tough hydrogels: A review. *Compos. Part B Eng.* **238**, 109895 (2022).

242. Highley, C. B., Rodell, C. B. & Burdick, J. A. Direct 3D printing of shear-thinning hydrogels into self-healing hydrogels. *Adv. Mater.* **27**, 5075–5079 (2015).

243. Murphy, R. D., Kimmins, S., Hibbitts, A. J. & Heise, A. 3D-extrusion printing of stable constructs composed of photoresponsive polypeptide hydrogels. *Polym. Chem.* **10**, 4675–4682 (2019).

244. Hsieh, C.-T. & Hsu, S. Double-network polyurethane-gelatin hydrogel with tunable modulus for high-resolution 3D bioprinting. *ACS Appl. Mater. Interfaces* **11**, 32746–32757 (2019).

245. Costantini, M. *et al.* 3D bioprinting of BM-MSCs-loaded ECM biomimetic hydrogels for

in vitro neocartilage formation. *Biofabrication* **8**, 035002 (2016).

246. Souzy, M., Zuriguel, I. & Marin, A. Transition from clogging to continuous flow in constricted particle suspensions. *Phys. Rev. E* **101**, 060901 (2020).
247. Hu, Y., Azadi, G. & Ardekani, A. M. Microfluidic fabrication of shape-tunable alginate microgels: Effect of size and impact velocity. *Carbohydr. Polym.* **120**, 38–45 (2015).
248. Ataie, Z. *et al.* Nanoengineered granular hydrogel bioinks with preserved interconnected microporosity for extrusion bioprinting. *Small* **18**, 2202390 (2022).
249. Budday, S., Holzapfel, G. A., Steinmann, P. & Kuhl, E. Challenges and perspectives in brain tissue testing and modeling. *PAMM* **19**, e201900269 (2019).
250. Shim, H. J., Sunwoo, S. H., Kim, Y., Koo, J. H. & Kim, D. H. Functionalized Elastomers for Intrinsically Soft and Biointegrated Electronics. *Advanced Healthcare Materials* vol. 10 2002105 (2021).
251. Xu, C., Dai, G. & Hong, Y. Recent advances in high-strength and elastic hydrogels for 3D printing in biomedical applications. *Acta Biomater.* **95**, 50–59 (2019).
252. Nonoyama, T. & Gong, J. P. Tough double network hydrogel and its biomedical applications. *Annu. Rev. Chem. Biomol. Eng.* **12**, 393–410 (2021).
253. Xin, H. Double-network tough hydrogels: a brief review on achievements and challenges. *Gels* **8**, 247 (2022).
254. Long, R. & Hui, C.-Y. Fracture toughness of hydrogels: measurement and interpretation. *Soft Matter* **12**, 8069–8086 (2016).
255. Jin, Y., Shen, Y., Yin, J., Qian, J. & Huang, Y. Nanoclay-based self-supporting responsive nanocomposite hydrogels for printing applications. *ACS Appl. Mater. Interfaces* **10**, 10461–10470 (2018).
256. Oytun, F., Kahveci, M. U. & Yagci, Y. Sugar overcomes oxygen inhibition in photoinitiated free radical polymerization. *J. Polym. Sci. Part A Polym. Chem.* **51**, 1685–1689 (2013).
257. Muir, V. G. *et al.* Sticking together: Injectable granular hydrogels with increased functionality via dynamic covalent inter-particle crosslinking. *Small* **18**, 2201115 (2022).
258. Yuk, H., Wu, J. & Zhao, X. Hydrogel interfaces for merging humans and machines. *Nat. Rev. Mater.* **7**, 935–952 (2022).
259. Yuk, H., Zhang, T., Lin, S., Parada, G. A. & Zhao, X. Tough bonding of hydrogels to diverse non-porous surfaces. *Nat. Mater.* **15**, 190–196 (2016).

260. Ma, Z., Bao, G. & Li, J. Multifaceted design and emerging applications of tissue adhesives. *Adv. Mater.* **33**, 2007663 (2021).

261. Lin, S. *et al.* Stretchable hydrogel electronics and devices. *Adv. Mater.* **28**, 4497–4505 (2016).

262. Wirthl, D. *et al.* Instant tough bonding of hydrogels for soft machines and electronics. *Sci. Adv.* **3**, 1–10 (2017).

263. Inoue, A., Yuk, H., Lu, B. & Zhao, X. Strong adhesion of wet conducting polymers on diverse substrates. *Sci. Adv.* **6**, 1–10 (2020).

264. Tian, K., Bae, J., Suo, Z. & Vlassak, J. J. Adhesion between hydrophobic elastomer and hydrogel through hydrophilic modification and interfacial segregation. *ACS Appl. Mater. Interfaces* **10**, 43252–43261 (2018).

265. Liu, Q., Nian, G., Yang, C., Qu, S. & Suo, Z. Bonding dissimilar polymer networks in various manufacturing processes. *Nat. Commun.* **9**, 1–11 (2018).

266. Li, K. *et al.* Tough, instant, and repeatable adhesion of self-healable elastomers to diverse soft and hard surfaces. *Adv. Sci.* **9**, 2105742 (2022).

267. Liu, Y. *et al.* Electrically programmable interfacial adhesion for ultrastrong hydrogel bonding. *Adv. Mater.* **34**, 2108820 (2022).

268. Li, C. *et al.* Polyelectrolyte elastomer-based ionotronic sensors with multi-mode sensing capabilities via multi-material 3D printing. *Nat. Commun.* **14**, 1–14 (2023).

269. Nam, S. & Mooney, D. Polymeric tissue adhesives. *Chem. Rev.* **121**, 11336–11384 (2021).

270. Ghosh, S. K., Park, J., Na, S., Kim, M. P. & Ko, H. A fully biodegradable ferroelectric skin sensor from edible porcine skin gelatine. *Adv. Sci.* **8**, 2005010 (2021).

271. Fang, L. *et al.* Stretchable, healable, and degradable soft ionic microdevices based on multifunctional soaking-toughened dual-dynamic-network organohydrogel electrolytes. *ACS Appl. Mater. Interfaces* **12**, 56393–56402 (2020).

272. Li, X. *et al.* Highly stretchable, self-healing, and degradable ionic conductive cellulose hydrogel for human motion monitoring. *Int. J. Biol. Macromol.* **223**, 1530–1538 (2022).

273. Zhang, S. *et al.* Body-integrated, enzyme-triggered degradable, silk-based mechanical sensors for customized health/fitness monitoring and in situ treatment. *Adv. Sci.* **7**, 1903802 (2020).

274. Ye, G., Song, D., Song, J., Zhao, Y. & Liu, N. A fully biodegradable and biocompatible

ionotronic skin for transient electronics. *Adv. Funct. Mater.* **33**, 2303990 (2023).

275. Tian, S. *et al.* A degradable-renewable ionic skin based on edible glutinous rice gel. *ACS Appl. Mater. Interfaces* **14**, 5122–5133 (2022).
276. Zhang, Y. *et al.* Ultra-fast programmable human-machine interface enabled by 3D printed degradable conductive hydrogel. *Mater. Today Phys.* **27**, 100794 (2022).
277. Chi, W. J., Chang, Y. K. & Hong, S. K. Agar degradation by microorganisms and agar-degrading enzymes. *Appl. Microbiol. Biotechnol.* **94**, 917–930 (2012).
278. Yun, E. J. *et al.* Metabolic and enzymatic elucidation of cooperative degradation of red seaweed agarose by two human gut bacteria. *Sci. Rep.* **11**, 1–14 (2021).
279. Nithya, R., Sivasankari, C. & Thirunavukkarasu, A. Electronic waste generation, regulation and metal recovery: a review. *Environ. Chem. Lett.* **19**, 1347–1368 (2021).
280. Rene, E. R. *et al.* Electronic waste generation, recycling and resource recovery: Technological perspectives and trends. *J. Hazard. Mater.* **416**, 125664 (2021).
281. Kiddee, P., Naidu, R. & Wong, M. H. Electronic waste management approaches: An overview. *Waste Manag.* **33**, 1237–1250 (2013).
282. Han, W. B., Lee, J. H., Shin, J. & Hwang, S. Advanced materials and systems for biodegradable, transient electronics. *Adv. Mater.* **32**, 2002211 (2020).
283. Jamshidi, R., Taghavimehr, M., Chen, Y., Hashemi, N. & Montazami, R. Transient electronics as sustainable systems: from fundamentals to applications. *Adv. Sustain. Syst.* **6**, 2100057 (2022).
284. Guo, Y. *et al.* Degradable and fully recyclable dynamic thermoset elastomer for 3d-printed wearable electronics. *Adv. Funct. Mater.* **31**, 2009799 (2021).
285. Xiang, L. *et al.* Wafer-scale high-yield manufacturing of degradable electronics for environmental monitoring. *Adv. Funct. Mater.* **29**, 1905518 (2019).
286. Tan, M. J. *et al.* Biodegradable electronics: Cornerstone for sustainable electronics and transient applications. *J. Mater. Chem. C* **4**, 5531–5558 (2016).
287. Diao, W. *et al.* Reversibly highly stretchable and self-healable zwitterion-containing polyelectrolyte hydrogel with high ionic conductivity for high-performance flexible and cold-resistant supercapacitor. *J. Appl. Polym. Sci.* **137**, 48995 (2020).
288. Jia, M., Luo, L. & Rolandi, M. Correlating ionic conductivity and microstructure in polyelectrolyte hydrogels for bioelectronic devices. *Macromol. Rapid Commun.* **43**,

2100687 (2022).

289. Bordi, F., Colby, R. H., Cametti, C., de Lorenzo, L. & Gili, T. Electrical conductivity of polyelectrolyte solutions in the semidilute and concentrated regime: The role of counterion condensation. *J. Phys. Chem. B* **106**, 6887–6893 (2002).

290. Zhao, Y. *et al.* Soft strain-insensitive bioelectronics featuring brittle materials. *Science* **378**, 1222–1227 (2022).

291. Zhang, C. *et al.* 3D printed, solid-state conductive ionoelastomer as a generic building block for tactile applications. *Adv. Mater.* **34**, 2105996 (2022).

292. Ge, Q. *et al.* 3D printing of highly stretchable hydrogel with diverse UV curable polymers. *Sci. Adv.* **7**, 1–11 (2021).

293. You, I. *et al.* Artificial multimodal receptors based on ion relaxation dynamics. *Science* **370**, 961–965 (2020).

294. Boutry, C. M. *et al.* A hierarchically patterned, bioinspired e-skin able to detect the direction of applied pressure for robotics. *Sci. Robot.* **3**, (2018).

295. Ham, J. *et al.* Porous dielectric elastomer based flexible multiaxial tactile sensor for dexterous robotic or prosthetic hands. *Adv. Mater. Technol.* **8**, 2200903 (2023).

296. Matsuhisa, N., Chen, X., Bao, Z. & Someya, T. Materials and structural designs of stretchable conductors. *Chem. Soc. Rev.* **48**, 2946–2966 (2019).

297. Jo, Y. J., Ok, J., Kim, S. Y. & Kim, T. il. Stretchable and Soft Organic–Ionic Devices for Body-Integrated Electronic Systems. *Advanced Materials Technologies* 2001273 (2021) doi:10.1002/admt.202001273.

298. Huo, R. *et al.* Tough Transient Ionic Junctions Printed with Ionic Microgels. *Adv. Funct. Mater.* **33**, 2213677 (2023).

299. Beck, P. A., Nickel, J. H. & Hartwell, P. G. High current density in μc-Si PECVD diodes for low temperature applications. in *Materials Research Society Symposium Proceedings* vol. 808 483–488 (Materials Research Society, 2004).